SURFACE CHARACTERIZATION OF NB CAVITY SECTIONS - UNDERSTANDING THE HIGH FIELD Q-SLOPE

A Dissertation

Presented to the Faculty of the Graduate School

of Cornell University

in Partial Fulfillment of the Requirements for the Degree of

Doctor of Philosophy

by

Olexander S. Romanenko

January 2009

SURFACE CHARACTERIZATION OF NB CAVITY SECTIONS -
UNDERSTANDING THE HIGH FIELD Q-SLOPE

Olexander S. Romanenko, Ph.D.
Cornell University 2009

The high field Q-slope in niobium cavities was studied by analyzing the samples cut out from regions of strong and weak heating in the high magnetic field region of the cavity walls. A variety of surface tools were used: SEM/EDX, XPS, AES, EBSD, optical profilometry.

Based on the surface analysis several possible primary sources of the high field Q-slope have been eliminated, such as roughness, niobium oxide, and foreign contaminants. The microcrystalline structure of the cavity samples was studied for the first time and the effect of the mild baking on the dislocation content was discovered. An alternative model to explain the HFQS and a mild baking effect is proposed, as suggested by results from this work.

Defects that produced additional losses before the HFQS onset were also identified by thermometry and analyzed using the SEM. It was found that defects were pits.

BIOGRAPHICAL SKETCH

Olexander Romanenko was born on January 24, 1982, in Zaporozhye, Ukraine. In 1998 he entered the Moscow Institute of Physics and Technology, from which he successfully graduated in May, 2002, with the Bachelor of Sciences in Applied Physics and Mathematics. In August, 2002 he entered a graduate program in physics at Cornell University. Alexander graduated from Cornell University in January, 2009 with the Ph.D. in Physics.

To my parents, Sergey and Valentina Romanenko

ACKNOWLEDGEMENTS

First I would like to thank many people who directly helped me to complete this thesis work.

My former fellow student and a life-long friend Grigory Eremeev who helped me with cavity tests, and provided a lot of feedback on the results. A research associate in SRF group Dave Meidlinger with whom we prepared and tested two of the three cavities involved in the thesis work.

Jonathan Shu from Cornell Center for Materials Research (CCMR) taught me how to use XPS and performed several studies on the samples. Another CCMR expert John Hunt trained me to use EBSD, which brought in many valuable results for this thesis, and optical profilometry.

Prof. Peter Simpson from University of Western Ontario performed positron annihilation studies on the samples. Dr. Joseph Woicick from BNL analyzed several samples with XPS using the synchrotron X-ray source at NSLS.

John Kaufman from SRF group taught me how to use an in-house Auger/SIMS system and a sample baking setup.

Samples were cut out from the cavities by the Machine Shop experts: John Kaminski and Phil Hutchings. Chemical treatment of samples, if needed, was always done in time by Holly Conklin, Aaron Windsor, Terri Gruber and Neal Sherwood.

I'm greatly indebted to my chief advisor Hasan Padamsee, whose patience, help, encouragement, and support allowed me to perform this thesis work. His willingness to let me explore novel ideas was of great value for the final completion of this thesis project.

I thank Prof. J. Sethna for valuable discussions on some theoretical aspects of this work.

I would like to thank current and former members of the SRF group, from whom I learned, and who were always helpful and available for discussion of any problems with experiments: Matthias Liepe, Zach Conway, Rongli Geng, Valery Shemelin, Sergey Belomestnykh, Ivan Bazarov, Phil Barnes, Greg Werner, Eric Chojnacki, James Sears, Rick Roy, Don Heath, Peter Quigley, Curtis Crawford, Bill Ashmanskas, Georg Hoffstaetter, Charlie Sinclair and Maury Tigner.

I would like to acknowledge the help of administrative and drafting staff at Newman Lab for providing me the necessary support: Peggy Steenrod, Monica Wesley, B. J. Bortz, Jeanne Butler and Pam Morehouse.

I would also like to thank current and former students in the SRF group for fruitful discussions of many science and non-science topics: Yi Xie, Justin Vines and Linh Nguyen.

I want to thank the members of my special committee: Prof. G. Dugan and Prof. C. Csaki for reading this document. And I want to thank again my advisor Hasan Padamsee for providing a timely feedback on my writing.

Lastly, I thank all my friends and family for their constant support throughout the years spent on the thesis research.

TABLE OF CONTENTS

LIST OF TABLES

LIST OF FIGURES

CHAPTER 1

INTRODUCTION

Superconducting radio frequency (RF) cavities have become the prime technology choice for current and future particle accelerators such as CESR, CEBAF, XFEL, ERL, ILC etc. The main advantage of the superconducting niobium cavities over the previously standard normal conducting copper cavities is the extremely low dissipated power due to the small RF losses in the superconducting state. This results in an efficient transfer of RF power to the particle beam power. Still, the advantage in losses comes with the cost of the power for cavity refrigeration, which is needed to keep superconducting cavities at typical operating temperatures of 1.5-4.2 K depending on the RF frequency for the particular application. Nevertheless the total AC power needed to provide a given accelerating gradient is less in the case of the superconducting cavities than in the case of normal conducting ones for CW and high duty factor operation.

Accelerating gradients up to the record value of 59 MV/m have been demonstrated in niobium single cell cavities. In the case of multicell cavities intended for use in future accelerators such as ILC, the achieved gradients are lower. The specification for ILC is currently to have an average qualifying gradient of 35 MV/m in 1.3 GHz 9-cell cavities, which is not yet achieved with a high enough consistency.

Even though record-high gradients are achieved in single cell cavities, there are gaps in the understanding of the physics behind the various effects that depend on surface condition and variations in cavity performance. Most of the recently adopted preparation steps are not well understood and were empirically found to improve the high field surface resistance, or the quench field. For

example, electropolishing, which has become a standard step in cavity preparation (instead of a formerly routine buffered chemical polishing), followed by a 100-120°C in situ annealing of the cavity for 1-2 days allows small grain cavities to consistently achieve a high quality factor up to the highest accelerating gradient. Whereas small grain cavities, which undergo a buffered chemical polishing and baking, are often limited by the unexplained high field degradation of the quality factor, one of the main topics of this thesis. The benefits of mild baking are not yet understood.

Historically, as soon as the physics was understood behind each of the limitations encountered in the quest for higher accelerating gradients, a new treatment recipe(s) was invented that significantly improved consistently achieved gradients and optimized the time and cost for the cavity preparation. Currently, the high field behavior of RF cavities (high field Q-slope) and its dependence on the surface conditions is a major puzzle to be solved.

The main topic of this thesis work is to try to understand how the detail nature of the RF surface translates into the high field surface resistance.

This thesis is organized as follows.

In Chapter 2 an overview of the RF cavities is given, and properties of niobium in the superconducting state are discussed.

In Chapter 3, known sources of dissipation in cavities are presented and the little understood Q-slopes at low, medium and high fields are introduced.

In Chapter 4, several recently proposed models for the high field Q-slope are reviewed, and the problems with each of them are discussed.

In Chapter 5, a brief overview is given of cavity preparation steps, which will be involved in the discussion of the thesis results.

In Chapter 6, results of the RF tests on the cavities used in this thesis work are reported.

Chapter 7 presents the results of the optical profilometry analysis of the roughness on the samples dissected from the cavities.

Chapter 8 reports on XPS investigations of the niobium oxide structure of the cavity samples.

Chapter 9 presents the results of the EBSD analysis of the crystalline microstructure of the samples. A method of analysis based on the local misorientation is applied to analyze the difference in the dislocation content between the samples and the effect of the mild baking.

Based on the experimental results a model is presented in Chapter 10 for the HFQS and the mechanism behind the mild baking effect.

Summary of the thesis work is given in Chapter 11.

In Appendix A, preliminary results of the positron annihilation studies of the vacancy concentration in niobium samples are presented.

CHAPTER 2

SUPERCONDUCTING RF CAVITIES

2.1 Cavity Fundamentals

Niobium superconducting cavities are radio frequency (RF) resonators, which provide the electric field to accelerate a particle beam. The *accelerating gradient* is defined as an energy gain per unit length:

$$E_{acc} = \frac{V_{acc}}{d} \tag{2.1}$$

where d is the length of the cavity, and V_{acc} is the accelerating voltage defined as

$$V_{acc} = \left| \frac{1}{e} \times maximum\ energy\ gain\ possible\ during\ transit \right| \tag{2.2}$$

If we consider axis z to be aligned with the cavity symmetry axis, and the cavity resonates at the mode of angular frequency ω, then we have for V_{acc}:

$$V_{acc} = \left| \int_0^d E_z(z) e^{\frac{i\omega z}{c}} dz \right| \tag{2.3}$$

The RF field in the cavity leads to the dissipation in the cavity walls due to the non-zero microwave resistance of superconducting niobium, which will be discussed in the following chapter. The non-zero dissipation is characterized by the surface resistance R_s, and the magnitude of the magnetic field at the cavity surface. The power dissipated per unit area of the wall is:

$$\frac{dP_{diss}}{ds} = \frac{1}{2} R_s \left| \mathbf{H} \right|^2 \tag{2.4}$$

where **H** is the local magnetic field amplitude. Hence, the total dissipated power P_{diss} is given by an integral over the interior cavity wall:

$$P_{diss} = \frac{1}{2} R_s \int_S \left| \mathbf{H} \right|^2 ds \tag{2.5}$$

In practice, it is more convenient to characterize cavity losses using a cavity *quality factor* Q_0, which is defined as:

$$Q_0 = \frac{\omega U}{P_{diss}} \tag{2.6}$$

where ω is the angular frequency of the operating field mode, and U is the stored energy of the electromagnetic field in the cavity, which can be calculated from the magnetic field amplitude:

$$U = \frac{1}{2}\mu_0 \int_V |\mathbf{H}|^2 \, dV \tag{2.7}$$

For the cavity quality factor Q_0 we then obtain:

$$Q_0 = \frac{\omega_0 \mu_0 \int_V |\mathbf{H}|^2 \, dV}{R_s \int_S |\mathbf{H}|^2 \, ds} = \frac{G}{R_s} \tag{2.8}$$

where

$$G = \frac{\omega_0 \mu_0 \int_V |\mathbf{H}|^2 \, dV}{\int_S |\mathbf{H}|^2 \, ds} \tag{2.9}$$

is the *geometry factor*, which only depends on the cavity shape and the distribution of the electromagnetic field in the accelerating mode.

The distribution of the electromagnetic field in the cavity is governed by Maxwell's equations, which reduce to the wave equations for the case of the fields in the cavity:

$$\left(\nabla^2 - \frac{1}{c^2}\frac{\partial^2}{\partial t^2}\right)\begin{pmatrix}\mathbf{E}\\ \mathbf{H}\end{pmatrix} = 0 \tag{2.10}$$

If we assume that niobium surface behaves as a perfect conductor, then the boundary conditions, which have to be satisfied at the cavity wall are:

$$\hat{n} \times \mathbf{E} = 0, \; \hat{n} \cdot \mathbf{H} = 0 \tag{2.11}$$

Two families of solutions exist to the Eq. (2.10), which are denoted as *transverse magnetic* (TM) modes and *transverse electric* (TE) modes. For TM modes the

magnetic field is everywhere transverse to the z-axis, whereas the electric field is transverse to the z-axis for TE modes. For the purpose of particle acceleration only TM modes are useful, since TE modes do not have a longitudinal electric field on the beam axis. Typically, SRF cavities are operated in the TM_{010} mode, which has the lowest eigenfrequency among the TM modes.

The analytical solution for the cavity with the input coupler port and other symmetry-breaking parts does not exist, so usually computer-based field solvers (i.e. SLANS, Microwave Studio) are used to find the distribution of the fields inside the cavity. For Mark III shape elliptical cavities used in this thesis work, the distribution of the electric and magnetic fields on the walls of the cavity is shown in Fig. 2.1.

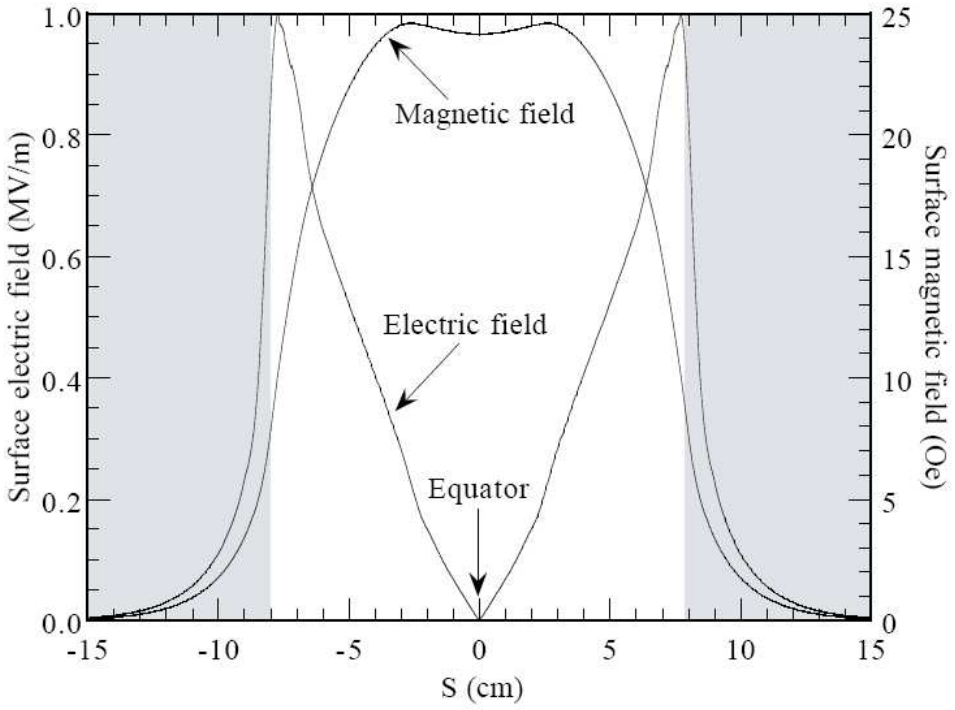

Figure 2.1: Electric and magnetic fields distribution on the cavity walls for the elliptical MARK III shape (reproduced from [28].

The geometry factor, which is provided by the field solvers as well, is $G = 273\ \Omega$ and the ratios of the highest surface electric and magnetic fields to the accelerating gradient E_{acc} are:

$$\begin{aligned} \frac{E_{peak}}{E_{acc}} &\cong 1.83 \\ \frac{H_{peak}}{E_{acc}} &\cong 44.98 \frac{Oe}{MV/m} \end{aligned} \tag{2.12}$$

2.2 Superconductivity

Superconductivity was discovered in 1911 by H. Kamerlingh-Onnes in mercury, lead and tin, when he observed a complete disappearance of the electrical resistance below the material-specific critical temperature T_c. A complete theoretical understanding of classic superconductors was not achieved until the BCS theory was formulated in 1950s. Up to now many elements and compounds have been found to possess superconducting properties. Among the superconducting elements niobium has the highest critical temperature and relatively high critical fields, which motivates its choice as a material for superconducting RF cavities.

2.2.1 Properties of superconductors

Superconductors have two main characteristic properties. The first one is an absence of any measurable resistance to DC electric currents below the critical temperature T_c. The second one is perfect diamagnetism, which is the expulsion of any external magnetic field from the interior of the superconductor up to the critical field B_c – called a Meissner-Ochshenfeld effect. For type I

superconductors there exists only one critical field, above which superconductivity is destroyed, and the material becomes normal conducting. For type II superconductors, as soon as the applied magnetic field reaches the first critical field B_{c1}, it becomes energetically favorable for the magnetic field to penetrate partially since the interface energy between the superconducting and normal phases becomes negative. At $B > B_{c1}$ the magnetic flux enters type II superconductors in the form of fluxoids each carrying a quantum of the magnetic flux $\phi_0 = h/2e = 2.07 \times 10^{-15}\ Wb$, and the number of fluxoids increases with the increase in the applied magnetic field. When the applied field reaches the second critical field B_{c2} the whole material becomes normal conducting.

Typical magnetization curves for type I and type II superconductors is shown in Fig. 2.2.

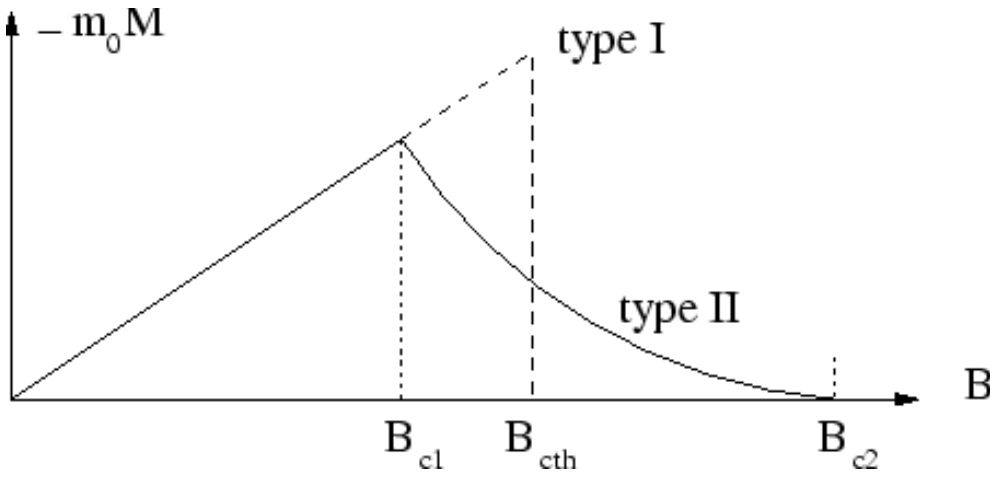

Figure 2.2: Typical magnetization curves for type I and II superconductors.

In order to explain the Meissner effect, H. London and F. London proposed two empirical equations, which described the expulsion of the magnetic field

from the bulk of a superconductor:

$$\frac{\partial \mathbf{J}}{\partial t} = \frac{n_s e^2}{m}\mathbf{E} \tag{2.13}$$

$$\frac{m}{n_s e^2}\nabla \times \mathbf{J} = -\mathbf{B} \tag{2.14}$$

Using London equations 2.13-2.14 and Maxwell's equations we obtain for the static field distribution at the half-space filled with superconductor:

$$B(z) = B_0 e^{-\frac{z}{\lambda_L}},\ J(z) = J_0 e^{-\frac{z}{\lambda_L}} \tag{2.15}$$

so that the magnetic field and the shielding current density have a finite penetration depth, which is characterized by a constant

$$\lambda_L = \sqrt{\frac{m}{\mu_0 n_s e^2}} \tag{2.16}$$

named a London penetration depth. For a very high purity niobium (RRR = 2000), the London penetration depth was measured to be $\lambda_L \approx 40\ nm$ [23]. The temperature dependence of the penetration depth is given by:

$$\lambda_L(T) = \frac{\lambda_L(0)}{\sqrt{1 - \left(\frac{T}{T_c}\right)^4}} \tag{2.17}$$

An extremely successful theory of superconductivity was developed by Bardeen, Cooper and Schrieffer in 1957 [2]. The fundamental effect underlying the superconductivity is the "condensation" of electrons within $k_B T_c \approx \hbar\omega_D$ of the Fermi surface into pairs due to the effective attractive interaction caused by lattice vibrations (phonons). The resulting Cooper pairs can be considered as single particles carrying a charge of $2e$ and a mass of $2m$ with the pairing energy of 2Δ. A new density of states near the Fermi surface exhibits an energy gap Δ, which is the absence of any energy levels within 2Δ from the Fermi surface ϵ_F.

The BCS theory predicts the following relation between the superconducting gap at $T = 0\ K$ and the critical temperature:

$$2\Delta(0) = 2 \times (1.76 k_B T_c) = 3.12\ meV \tag{2.18}$$

The actual size of the gap depends on the strength of electron-phonon interaction, and for niobium it was found to be $\Delta(0)/k_B T_c = 1.9$. A characteristic length scale for the Cooper pair, also known as a *coherence length*, can be found from Heisenberg's uncertainty principle, and in terms of the Fermi velocity v_F is given by:

$$\xi_0 = \frac{\hbar v_F}{k_B T_c} = \frac{\hbar v_F}{\Delta} \tag{2.19}$$

For niobium $\xi_0 \approx 39\ nm$.

A Ginzburg-Landau parameter is defined as a ratio of London penetration depth and a coherence length:

$$\kappa = \frac{\lambda_L}{\xi_0} \tag{2.20}$$

and the value of κ determines if the superconductor is type I or type II. For type I: $\kappa < \frac{1}{\sqrt{2}}$, and for type II: $\kappa > \frac{1}{\sqrt{2}}$. For niobium we have $\kappa \approx 1$, and it is a weak type II superconductor.

A zero DC resistance in the superconducting state can be understood based on the two-fluid model. One fluid is a superfluid of electrons condensed into Cooper pairs, and the other fluid is a normal fluid of free electrons. At $T = 0\ K$ all of the electrons are paired, but at a finite temperature $T < T_c$ a fraction of unpaired electrons is given by the Boltzmann factor $exp(-\Delta/k_b T)$.

Cooper pairs move through the lattice without dissipation if the thermal energy of phonons is less than the superconducting gap 2Δ, i.e. $T < T_c$. Thus the supercurrent flows with zero DC electric resistance. Normal and superconduct-

ing current components are effectively in parallel, but since the supercurrent experiences no resistance, the total current is carried exclusively by Cooper pairs, whereas normal electrons are shielded from the electric field, and hence there is no normal current, which would produce dissipation.

In the case of RF currents though, the resistance of superconductors is not zero. A finite resistance arises due to the inertial mass of Cooper pairs. When the superconductor is exposed to the time-varying electric field, the Cooper pairs (superfluid) are unable to completely shield the normal fluid. Time-varying magnetic field in the penetration depth induces a time-varying electric field, which acts on the normal electrons and causes dissipation. From Faraday's law an induced electric field is proportional to the magnetic field rate of change:

$$E_{ind} \propto \frac{dH}{dt} \propto \omega H \tag{2.21}$$

and the resulting normal current density is

$$j_n \propto n_n E \propto n_n \omega H \tag{2.22}$$

where n_n is the number of normal electrons, $n_n \propto exp\left(-\frac{\Delta}{k_B T}\right)$. The dissipated power produced by RF currents is then:

$$P_{diss} \propto j_n E_{ind} \propto n_n \omega^2 H^2 \tag{2.23}$$

Using Eq. (2.4) we finally obtain:

$$R_s \propto n_n \omega^2 \propto \omega^2 exp\left(-\frac{\Delta}{k_b T}\right) \tag{2.24}$$

The exact expression for the surface resistance involves several material parameters, but a good practical approximation for $T < T_c/2$ and for frequencies much smaller than $2\Delta/h \approx 10^{12}\ Hz$ is

$$R_{BCS} = 2 \times 10^{-4} \frac{1}{T} \left(\frac{f}{1.5}\right)^2 exp\left(-\frac{17.67}{T}\right) \tag{2.25}$$

where f is the RF frequency in GHz.

2.2.2 Critical fields

A thermodynamic critical field H_c is defined by the magnetic energy density needed to overcome the reduction in the free energy $f_n(T) - f_s(T)$ due to the condensation into the superconducting state:

$$\frac{H_c^2(T)}{8\pi} = f_n(T) - f_s(T) \tag{2.26}$$

It is approximated very well by a parabolic law:

$$H_c(T) \approx H_c(0)\left[1 - \left(\frac{T}{T_c}\right)^2\right] \tag{2.27}$$

The thermodynamic critical field is a measurable property of type I superconductors, but for type II superconductors there is no physical phenomenon, which takes place at that field. For type II superconductors the surface energy of the normal-superconducting interface becomes negative as soon as the applied magnetic field reaches the lower critical field H_{c1}. A negative surface energy makes it energetically favorable to have a mixed state with the partial penetration of the magnetic flux in the form of fluxoids each carrying a quantum of the magnetic flux ϕ_0. With further increase in the applied field, the number of fluxoids penetrating the material increases, until their normal conducting cores start to overlap, which happens at the higher critical field H_{c2}, and the superconductivity is destroyed in the bulk of the superconductor. For measurements with very high purity niobium (RRR = 2000), critical fields were reported in [23]: $H_{c1} = 1800\ Gauss, H_{c2} = 3900\ Gauss$.

The Ginzburg-Landau (G-L) theory [24], although applicable for temperatures T not much below T_c, allows an estimate of both H_{c1} and H_{c2} in some limits. For the higher critical field H_{c2} it gives:

$$H_{c2} = \sqrt{2}\kappa H_c \tag{2.28}$$

and for the lower critical field in the limit $\kappa \gg 1$ (which is not a good approximation for niobium):

$$H_{c1} = \frac{log\kappa + 0.081}{\kappa\sqrt{2}} \tag{2.29}$$

The calculations of the bulk critical fields within the G-L theory neglect finite dimensions, and for real superconductors, surface effects should be considered as well. Saint-James and de Gennes [42] showed that superconductivity can be sustained at a metal-insulator interface in a parallel field H_{c3}, higher by a factor of 1.695 than H_{c2}. The detailed analysis of the boundary conditions in the G-L theory shows that:

$$H_{c3} = 1.695 H_{c2} = 1.695(\sqrt{2}\kappa H_c) \tag{2.30}$$

Furthermore, in the absence of nucleation centers at the surface of superconductors, "superheated" superconducting state may persist metastably for $H > H_c$ up to the *superheating critical field* H_{sh}. A superheating field can be calculated in various limits using the G-L theory:

$$\begin{aligned} H_{sh} &= 0.75 H_c \; for \; \kappa >> 1 \\ H_{sh} &= 1.2 H_c \; for \; \kappa \approx 1 \\ H_{sh} &= \frac{H_c}{\sqrt{\kappa}} \; for \; \kappa << 1 \end{aligned} \tag{2.31}$$

Practically, for niobium cavities there is much discussion at this point, about which of the critical fields is the ultimate limit. RF surface magnetic fields in

Table 2.1: Critical fields and temperature for high purity niobium (RRR = 2000) from [23].

Property	Measured value
T_c	9.29 K
H_c	2061 Gauss
H_{c1}	1800 Gauss
H_{c2}	3900 Gauss

excess of H_{c1} and H_c have been successfully demonstrated recently in single cell niobium cavities [18, 17]. There is also some evidence that H_{c1} might be the practical limiting field due to a strong dissipation caused by the penetrating fluxoids as will be discussed in Ch. 10.

CHAPTER 3

LOSSES IN SUPERCONDUCTING NIOBIUM CAVITIES

3.1 Residual resistance

The surface resistance of niobium as calculated from the cavity quality factor is in practice higher than the corresponding BCS surface resistance and the total surface resistance can typically be written in the form:

$$R_s = R_{BCS}(T) + R_{res} \tag{3.1}$$

where $R_{BCS}(T)$ is the temperature-dependent BCS surface resistance, and R_{res} is the temperature-independent *residual resistance*. There are several possible sources of the residual resistance, which are understood, such as trapped magnetic flux and niobium hydrides, but in the absence of these sources niobium cavities still have a few nΩ of the residual resistance, the origin of which is not clear, but possible sources could be absorbed gases etc. One should distinguish between the fundamental losses, which are inherent to the cavity material, and parasitic losses caused by different extrinsic phenomena discussed below.

3.2 Multipacting

The *multipacting* phenomenon in niobium cavities is a resonant process of the incident power absorption by the electrons originating from the cavity walls. Roughly speaking, if the electron emitted from the niobium surface by some physical mechanism (i.e. cosmic rays, field emission, photoemission etc.) is accelerated by the cavity electric field and upon colliding with the cavity surface

produces more than one secondary electron, then the the number of electrons involved multiplies (hence the name). Secondary electrons are accelerated in trajectories that return to the surface and upon impact produce more electrons. The resulting avalanche current is limited only by the available RF power and the space-charge effects, and hence it becomes impossible to raise the field in the cavity beyond the multipacting barrier. In order for multipacting to be possible, the secondary emission coefficient should be high enough, and the electron trajectories in the cavity should satisfy certain resonant conditions. By selecting the proper cavity shape it is possible to choose a design such that multipacting is avoided. As soon as the physical mechanism was identified, the spherical and elliptical cavity shapes emerged, which essentially eliminated the multipacting problem, by making the accelerated electrons move towards the cavity equator where the electric field is zero and secondary electrons can not gain enough energy to produce secondaries.

3.3 Field emission

Field emission is a well-known effect of the emission of electrons from the regions at the surface where the applied electric field is high and electrons in niobium can tunnel through the work function barrier. The theory of field emission was developed by Fowler and Nordheim (FN) [22] and gives the following expression for the tunneling current density:

$$j = \frac{e^2}{8\pi h}\frac{E^2}{\phi t^2(y)} exp\left(-\frac{8\pi\sqrt{2m\,(e\phi)^3}v(y)}{3heE}\right) \tag{3.2}$$

where e is the electron charge, m is the electron mass, h is a Planck's constant, ϕ is the work function in eV, and E is the instantaneous electric field in MV/m.

In practice, for niobium cavities the FN current density should be modified by using βE instead of E, where β is the field enhancement factor that originates from the electric field enhancement at sharp tips on the surface.

Areas of the cavity surface that have a higher β value or a reduced work function will become field emission sites at lower electric fields. The nature of field emitters was studied in detail in [28] and the general conclusion is that most of the field emitters are either foreign particles or protrusions on the surface such as scratches.

The natural way to overcome the field emission is to use the high pressure ultrapure water rinsing (HPR) in order to remove the majority of the particle contaminants from the cavity surface. If the field emitter is still present even after the HPR, it is sometimes possible to eliminate it by high power processing when the field emitter particle is heated up by a short pulse of a very high RF power to the temperature of evaporation. In general, the field emission phenomenon is well understood and can be overcome by cleanliness methods.

3.4 Q-slopes

The typical RF test result for EP and BCP niobium cavities is shown in Fig. 3.1.

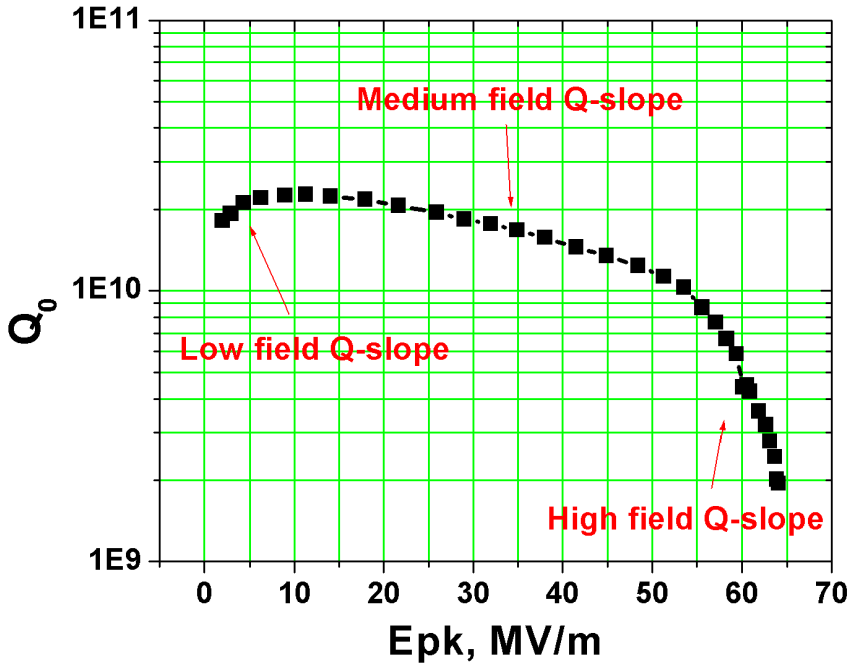

Figure 3.1: Typical Q_0 vs. E_{peak} curve for SRF niobium cavities limited by the high field Q-slope.

It is clearly observed that the dependence has three distinct regions, which are respectively called low, medium and high field Q-slopes.

3.4.1 Low field Q-slope

Low Field Q-slope (LFQS) is a decrease in the cavity surface resistance with field in the range of the E_{acc} below approximately 5 MV/m. The physical mechanism, which underlies the effect, is not clear at this time although several mechanisms are proposed, but since the LFQS does not represent any obstacles to the cavity performance, it obtained relatively low attention as compared to the following Q-slopes.

3.4.2 Medium field Q-slope

Medium Field Q-slope (MFQS) is a mild degradation of the cavity quality factor with field until the quench or a high field Q-slope limitation is reached. Although the full understanding of the effect has not been yet developed, there is a strong theoretical indication that the MFQS is due to the positive feedback between the surface heating and the BCS surface resistance [15].

3.4.3 High field Q-slope

The high field Q-slope is a general phenomenon in superconducting niobium cavities, which arises in the absence of the parasitic losses discussed above (multipacting, field emission, hydrides) as soon as the peak magnetic field at the niobium surface reaches about 100 mT. The manifestation of the HFQS is the sharp increase in the surface resistance of niobium with the increased magnitude of the applied magnetic field. This in turn translates into the degradation of the cavity quality factor Q_0, which limits the achievable accelerating gradient. The HFQS is generic in the sense that BCP and EP cavities of all grain sizes exhibit the same behavior if no further annealing was applied after the chemical treatment. An empirical "cure" for the HFQS was found, which is an in situ baking of the cavity at 100-120°C in UHV for 12-48 hours depending on the grain size. Although baking allows to consistently prepare high performance niobium cavities, which do not have the HFQS, it is a time-consuming process (2 days), and the understanding of the physics behind the HFQS and the mild baking effect would possibly result in techniques leading to a substantial decrease in the cavity preparation time, and possibly better performance.

CHAPTER 4

HIGH FIELD Q-SLOPE MODELS

4.1 Introduction

Several models have been proposed in the recent decade to account for the observed high field Q-slope in niobium cavities including:

- Thermal Feedback [25]
- Interface Tunnel Exchange (ITE) model [27]
- Magnetic Field Enhancement (MFE) [14]
- Weak superconducting layer model [41]
- Modified oxygen pollution layer model [8]
- Magnetic impurities in the oxide [19]

In general, none of the theories agrees fully or satisfactorily with the experimental data, and some of them such as ITE and thermal feedback can already be excluded, since HFQS was shown to be a magnetic field effect, and the thermal feedback does not produce enough dissipation to account for the HFQS. Below we briefly describe the models, which can still explain the high field Q-slope at least partially, and present experimental facts that falsify them as a complete story.

4.2 Magnetic Field Enhancement (MFE)

The MFE model presented in [14] attributes the HFQS to the enhancement of the magnetic field at the sharp edges of the grain boundaries (see Fig. 4.1), which are especially pronounced for the small grain BCP cavities. Similarly to the electric field enhancement at sharp tips, the magnetic field is enhanced at the grain boundaries, and the enhancement factor can be as high as two as follows from the finite element simulations. As soon as the local magnetic field reaches the critical field, the area around the grain boundary edge becomes normal conducting and the dissipation increases sharply.

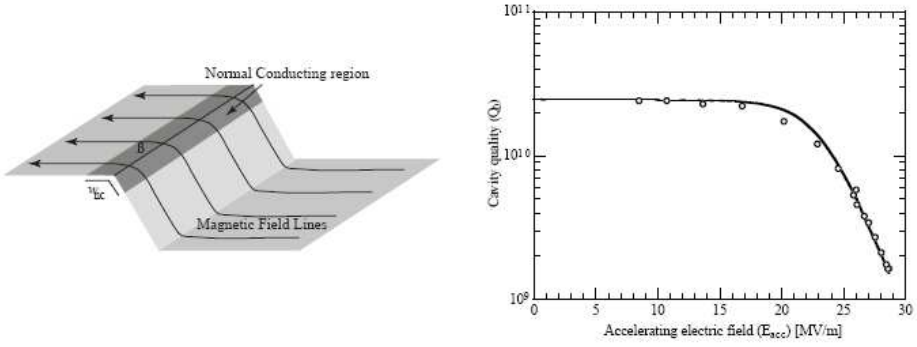

Figure 4.1: Schematic of the grain boundary edge becoming normal conducting (left) and the corresponding fit to the Q_0 vs. E_{acc} for the niobium cavity from [14].

The MFE model gives a reasonable fit to the cavity data, but there are several experimental results, which strongly oppose it. The obvious inconsistency is the presence of the HFQS in single grain cavities with no grain boundaries. In addition, despite the significant difference in roughness between small grain BCP and EP cavities, smoother EP cavities also show the HFQS - BCP and EP cavities that were not baked, behave remarkably similar. Another major difficulty is that

the baking effect is not described by the model since the surface roughness does not change due to baking.

4.3 Weak superconducting layer

The essence of this model is the possible existence of the "weak" superconducting layer with depressed superconducting properties just underneath the oxide layer on niobium. The degraded superconducting properties are attributed to the high concentration of the interstitial oxygen, which is known to strongly depress the niobium superconducting properties if present in concentrations of several atomic percent. Thus the critical field in the "weak" layer is reached at lower applied RF fields and the high field Q-slope emerges. Another basis for this model is the low temperature baking effect. Common interstitial impurities present in the cavity grade niobium are H, O, C and N. Since the low temperature baking at 100°C was found to remove the high field Q-slope in EP cavities of all grain sizes and large grain BCP cavities, it was suggested that the effect might come from the diffusion of interstitials. At the temperatures of 100-120°C both N and C are believed to be not mobile enough due to their low bulk diffusion coefficient, and H is mobile even at room temperature thus making any change of its depth profile reversible. Oxygen, on the other hand, has an appropriate diffusion coefficient that can explain the change in the material within the magnetic field penetration depth. For typical baking durations of 24-48 hours it was calculated that oxygen diffusion length is about 20 nm, which is consistent with the thickness of the baking-modified layer [9]. The schematic of the baking effect on the high-concentration oxygen layer is shown in Fig. 4.2.

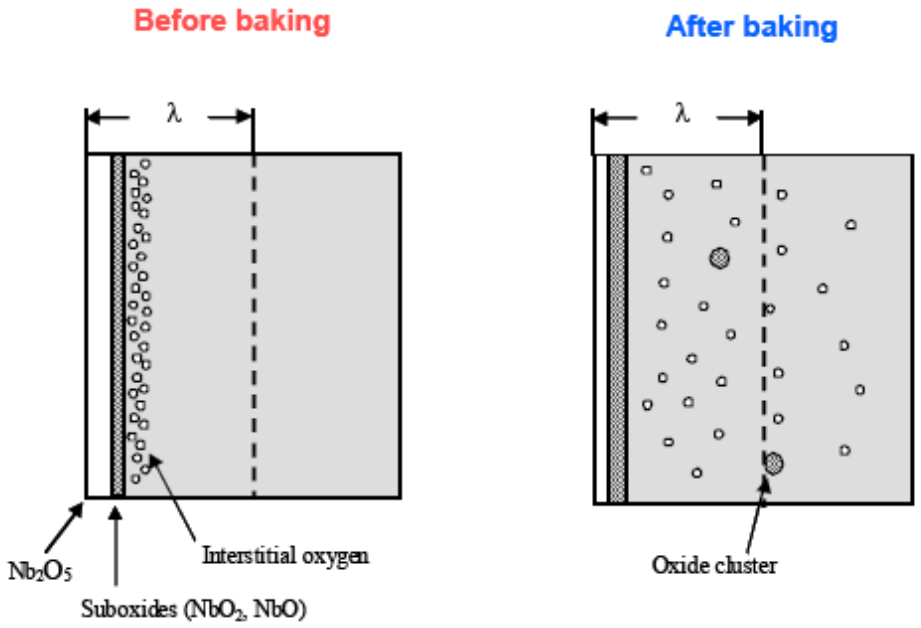

Figure 4.2: Schematic of the interstitial oxygen distribution before and after baking within the weak superconducting layer model from [6].

The major obstacle for this model to succeed is the lack of experimental evidence for the high oxygen-content layer underneath the oxide. Recent XPS [12] and SIMS [40] studies showed that this layer does not exist and the modification of the oxide and the interstitial oxygen content during the mild baking is reversed as soon as the cavity is exposed to the atmospheric air, which is in contradiction to the cavity experiments that show an unchanged baking benefit even after a year of air exposure. Other data not explained by this model is the superiority of small grain EP cavities over small grain BCP cavities after baking, since there is no reason to believe that the difference in roughness might affect the oxygen diffusion during baking.

4.4 Magnetic impurities

The most recent model proposed by T. Proslier and collaborators [19] is based on the possible existence of the magnetic impurities in the niobium oxide layer. Tunneling studies performed on the cavity grade niobium indicated that the electron density of states does not replicate the BCS theory prediction but instead points toward the existence of the increased number of quasiparticle excitations in the superconducting gap. The explanation suggested by authors is that the non-stoichiometric niobium oxide $Nb_2O_{5-\delta}$, which possesses magnetic properties, is present in the oxide layer and these magnetic impurities cause the dissipative scattering at the interface, which leads to the high field Q-slope. The low temperature baking effect is explained by the decrease in the non-stoichiometric oxide concentration and thus the decrease in the dissipation due to scattering. The tunneling conductance curves for baked and unbaked samples, which support the model, are shown in Fig. 4.3.

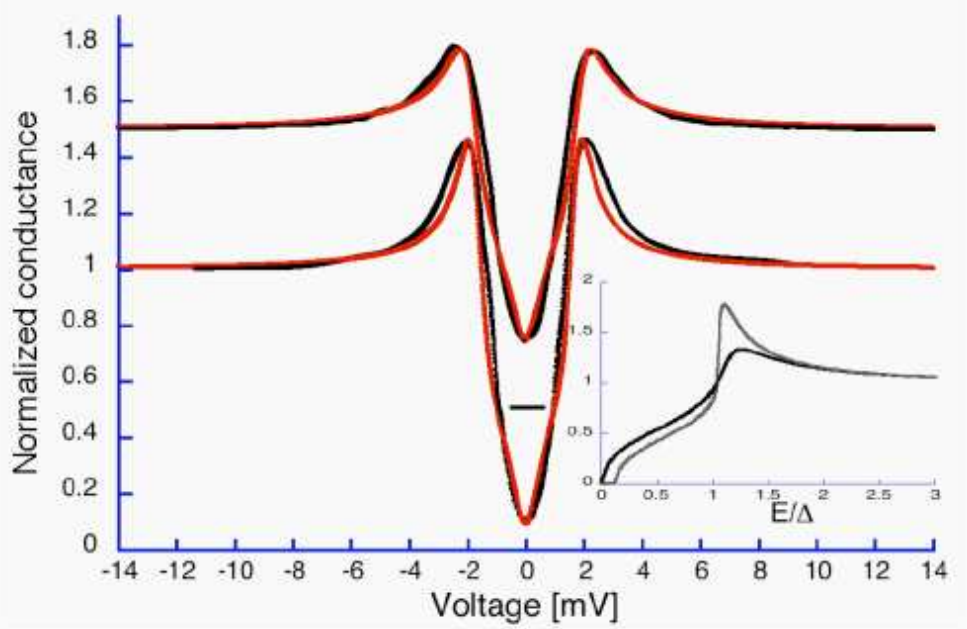

Figure 4.3: Tunneling conductance curves for unbaked (top) and baked (bottom) niobium samples from [19].

We believe that this model contradicts several experimental facts as found by cavity tests and surface studies. First, cavity experiments show that the high field Q-slope is not restored by the hydrofluoric acid rinsing of the baked cavity where the HFQS is healed. The effect of the HF treatment on niobium is the removal of the remaining oxide layer, which is subsequently regrown after water rinsing and air exposure. If the non-stoichiometric oxide inclusions were removed by the baking, there is a good reason to believe that a new oxide should again have similar magnetic impurities.

Furthermore, recent XPS studies [12] of the mild baking effect in UHV on the niobium oxide structure show that the slight changes caused by baking are completely reversible by the subsequent atmospheric air exposure. But cavity experiments indicate that the mild baking benefit (the healed HFQS) survives

air exposure. Thus small changes in the oxide due to baking are completely reversed by the air exposure, and XPS shows that there is no increase in the NbO_2 thickness or modification of the oxide as suggested by the model. Yet another indication of the irrelevance of the oxide layer to the HFQS are the cavity experiments reported in [11]. The nearly oxide-free cavity, which had the Nb_2O_5 layer removed by the in situ 400°C annealing, exhibited the same high field Q-slope as with the natural oxide before baking.

Summarizing, we think that magnetic impurities may exist in the niobium oxide layer, but they do not play a role in the high field Q-slope and the mild baking effect on niobium cavities. Although they might contribute to the low field Q-slope, which is sensitive to the oxide regrowth [47].

4.5 Conclusion

As presented above, none of the currently available models can explain all the experimental data collected on cavities and cavity material samples. A lack of the physical understanding of the processes involved in the high field Q-slope and the baking effect motivates further studies into the niobium structure within the London penetration depth and modifications introduced by the low temperature baking.

CHAPTER 5

CAVITY PREPARATION

A typical procedure of fabricating a single cell niobium cavity includes several steps as discussed in detail in [35]. Major steps undertaken in the process are (as reproduced from [35]):

- Material acquisition and inspection
- Half-cells forming by deep drawing or spinning
- Trimming
- Degreasing
- Light etch ($\approx 5\ \mu m$)
- De-rust
- Inspect for scratches, defects or rust
- Electron-beam weld iris
- Grind iris
- Light etch ($\approx 5\ \mu m$)
- Electron beam-weld equator
- Inspect weld
- Etch complete cavity ($\approx 100\ \mu m$)
- Postpurify in furnace (for highest RRR)
- Etch inside ($\approx 100\ \mu m$) and outside ($\approx 30\ \mu m$)
- Tune to correct frequency and field flatness
- Final chemistry ($\approx 5\ \mu m$)

- High-pressure rinsing
- Dry in clean room
- Assemble end flanges and couplers in clean room
- Evacuate

Recently, *electropolishing* (EP) for a 50-100μm material removal is increasingly used instead of a previously standard *Buffered Chemical Polishing* (BCP) as the chemical etching method before the high-pressure rinsing, since EP produces a much smoother cavity surface. The macro-roughness is reduced from several microns to less than 0.5 μm. We will briefly describe both BCP and EP procedure as the details will be relevant for a later discussion.

After the discovery of the HFQS and of the mild baking effect, an in situ baking of cavities at 100-120°C for 12-48 hours (depending on the grain size) became a part of the preparation for cavities capable of achieving the highest gradients. We will briefly describe BCP, EP and the mild baking process of the cavities, since these are fundamental for understanding of the thesis work.

5.1 Buffered chemical polishing

Chemical etching is required in order to remove a mechanical damage layer and surface contaminants introduced during handling. BCP is chemical etching of niobium by a mixture of hydrofluoric (HF–48% conc.), nitric (HNO_3–68% conc.), and phosphoric (H_3PO_4–85% conc.) acids. The volume ratios for a typical BCP recipe are – HF:HNO_3:H_3PO_4 = 1:1:2.

Hydrofluoric acid serves as an etching agent removing the niobium pentoxide via a chemical reaction. The naked niobium surface is then oxidized by nitric acid. Both processes go in parallel resulting in the etching effect. Phosphoric acid is added as a buffer (hence the name BCP) to slow down the reaction by diluting the mixture and increasing its viscosity, since otherwise the reaction is too violent and poorly controlled.

During BCP the temperature of the solution has to be kept below about 15°C in order to prevent hydrogen contamination of niobium. BCP produces a relatively large macro-roughness.

5.2 Electropolishing

Electropolishing is a chemical etching process facilitated by the application of a positive electric potential to the cavity surface enhancing the surface oxidation process. An electric charge concentration at the sharp tips of the surface result in the higher etching rates for those areas, which translates into a polishing effect. An acid solution typically used for EP is a mixture of hydrofluoric (HF - 48% conc.) and sulfuric (H_2SO_4) acids in the volume ratio of 1:9. EP gives smooth surface.

SEM images of niobium surface after BCP and EP are shown in Fig. 5.1.

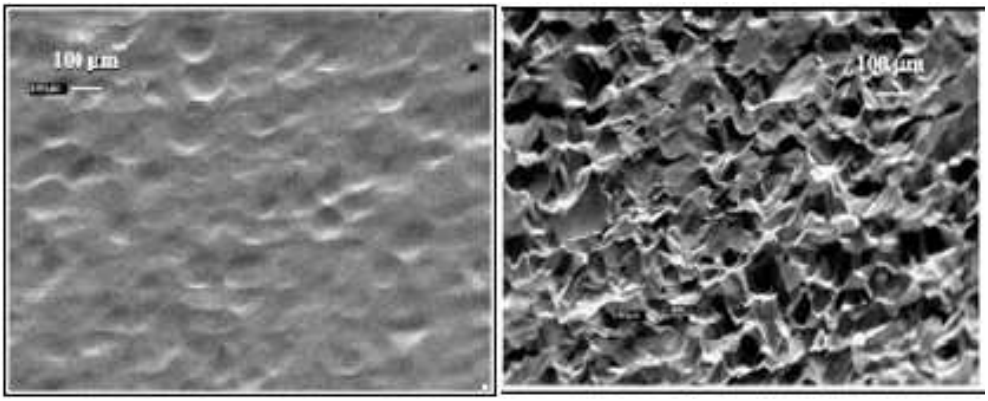

Figure 5.1: SEM images of the EP (left) and BCP (right) finish from [16].

5.3 Low temperature baking

It was found empirically that in order to remove the HFQS in EP-treated cavities of all grain sizes and large grain BCP cavities, an in situ heat treatment of the cavity at about 100-120°C for 1-2 days is required. Baking is not as effective, by contrast, on small grain BCP cavities.

There are several different procedures for baking of the cavities implemented in different labs worldwide.

At Cornell, two setups have been routinely used, as discussed in [9]. One of them utilizes heat tapes wrapped around the cavity walls. Another baking setup is based on the use of hot air in the thermal insulation box around the cavity.

At JLab, baking is performed [7] either in the oven by blowing a hot nitrogen gas on the cavity surface, or in the 2 K testing dewar by heating the helium gas by resistive heaters.

All of the baking setups produce similar results in terms of the cavity performance improvement.

It was shown that by removing about 20 nm of the material by anodizing [10] or BCP or EP the baking benefit is destroyed and the HFQS reappears.

CHAPTER 6

RF CAVITY TESTS AND DISSECTION

6.1 Introduction

RF tests of superconducting niobium cavities performed at Cornell and JLab [9, 7] with the temperature mapping system attached to the outer cavity walls indicate that in the HFQS regime the heating pattern in the high magnetic field region is not uniform but rather patchy with some areas exhibiting a higher temperature increase. The patchiness is more pronounced for large grain cavities. Since the reason for the patchiness is not known, we decided to utilize the following strategy in this thesis work in order to directly correlate niobium surface properties with the HFQS behavior:

- Prepare several 1.5 GHz single cell niobium cavities having different grain size or chemical preparation, i.e. large and small grain BCP and a small grain EP
- Test the cavities with the temperature mapping system attached, and up to the highest magnetic field in the HFQS regime
- Identify regions, which exhibit stronger and weaker heating and cut samples from the corresponding areas of the cavity walls
- Analyze the samples with various surface analytical techniques in order to look for any differences, which might be responsible for the different HFQS behavior

RF testing of the cavities was performed utilizing the RF setup described in detail in [9], a sketch of which is shown in Fig. 6.1.

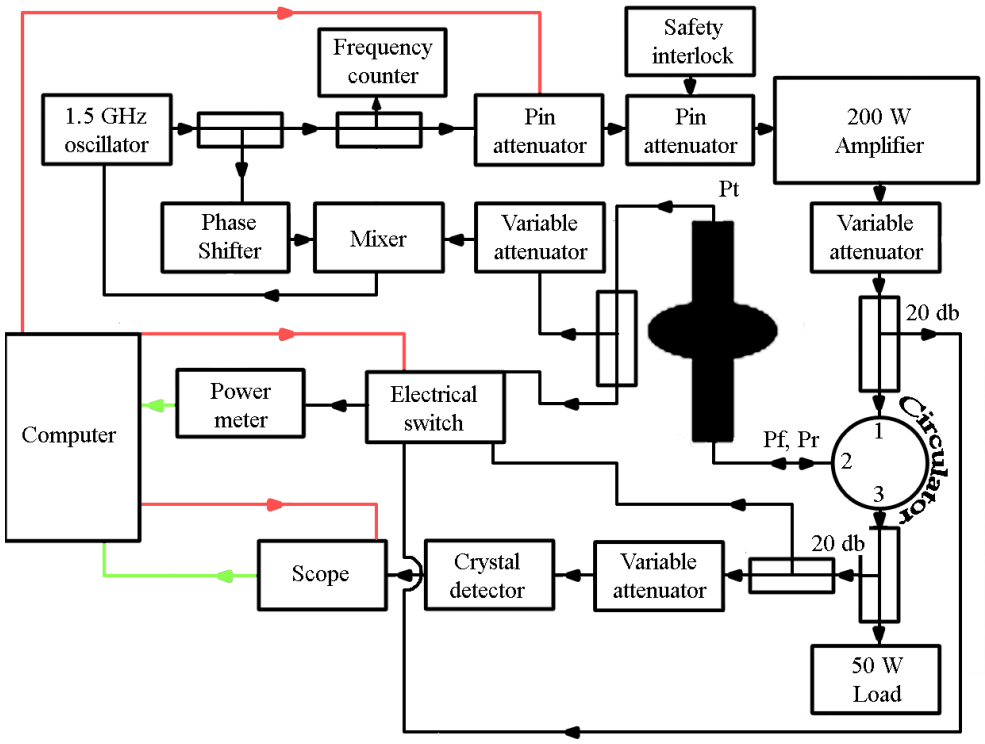

Figure 6.1: Schematic of the RF setup used for cavity testing (from [9]).

A temperature mapping system was attached to outer walls of the cavities during RF tests. The temperature mapping system consists of an array of 756 thermometers, each of the thermometers measuring the temperature difference between the spot on the cavity outer surface and a helium bath. Detailed description of the system can be found in [28, 9]. The best sensitivity of thermometers at the test temperature was about 1 mK, and the efficiency of temperature measurements (ratio of the measured temperature rise to the real temperature rise of the surface) of about 20-30%.

After identifying regions for dissection, the cavity cutting process itself is important, since the sample surface should not be contaminated and the temperature during the cutting process should not rise over the room temperature

in the sample central area, since it will effectively bake the sample and thus any useful information about unique surface structure and its relation to the baking effect might be destroyed. In this thesis work the automated milling machine was used for cutting with the pure water as a lubricant. Using water instead of normally used oil for lubrication is necessary, since it can only expose the sample surface to the water droplets, which do not effect the high field Q-slope properties because the high pressure water rinsing was shown not to alter the HFQS behavior of niobium cavities. Auger electron spectroscopy on the test sample before and after cutting indicated a slight increase of carbon level as expected from handling in air, but no foreign contaminants have been introduced due to cutting. The picture of the cavity with the samples cut out of its walls is shown in Fig. 6.2.

Figure 6.2: The picture of the cavity, which had hot and cold areas cut out for analysis. Arrow indicates one of the samples.

Samples needed to be cut only from the high magnetic field regions where the heating due to HFQS is dominant.

6.2 RF tests

6.2.1 Small grain BCP

The LE1-35 niobium cavity with a grain size of about 1 mm, which underwent a BCP treatment, was high pressure water rinsed and tested with the thermometry system attached. The Q_0 vs. H_{peak} results of the RF test of the cavity are shown in Fig. 6.3.

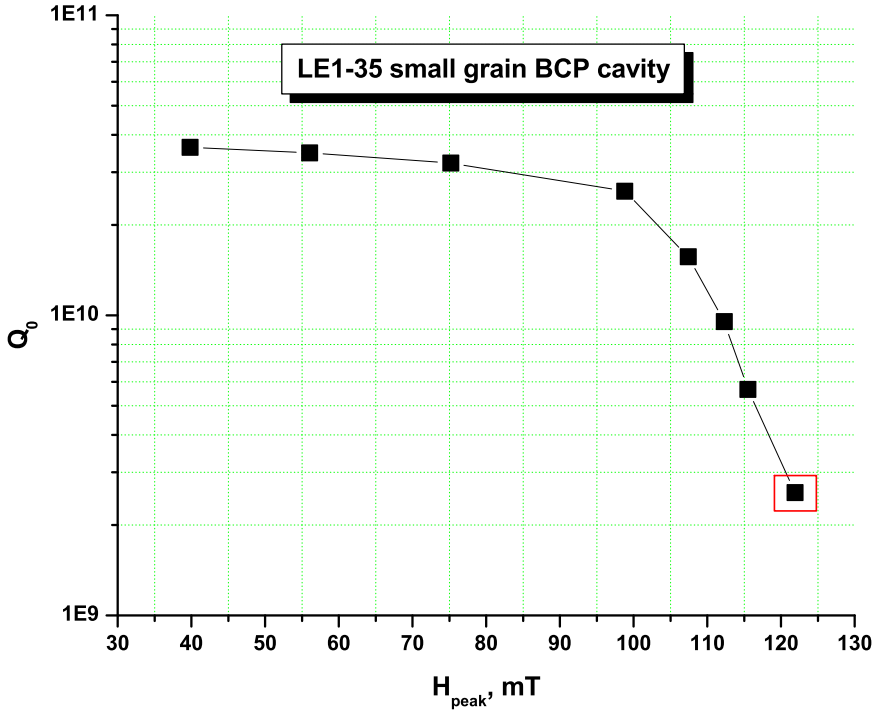

Figure 6.3: LE1-35 cavity quality factor Q_0 versus the peak magnetic field H_{peak}. The red square indicates the point, which corresponds to the temperature map used for dissection.

The highest obtained peak magnetic field of about 120 mT was limited by the available power. No X-rays were registered and thus no field emission loading was present during the test. The Q-drop is entirely due to the HFQS. The temperature map obtained at the field level marked with the red square, which is shown in Fig. 6.4, was used for selecting hot and cold areas.

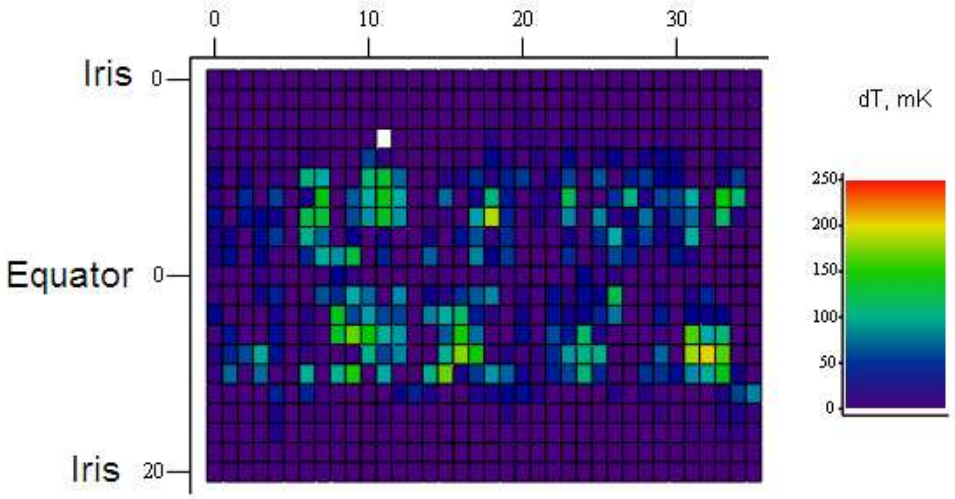

Figure 6.4: The temperature map of the LE1-35 cavity obtained at the peak magnetic field H_{peak} = 120 mT.

The HFQS started at the onset field of about $H_{peak} = 100\ mT$, which is a typical onset field. A non-uniform heating of the cavity walls is clearly observed in Fig. 6.4, which is also a typical feature of the HFQS.

A typical temperature sensor reading ΔT versus peak magnetic field H_{peak} for hot and cold samples is shown in Fig. 6.5.

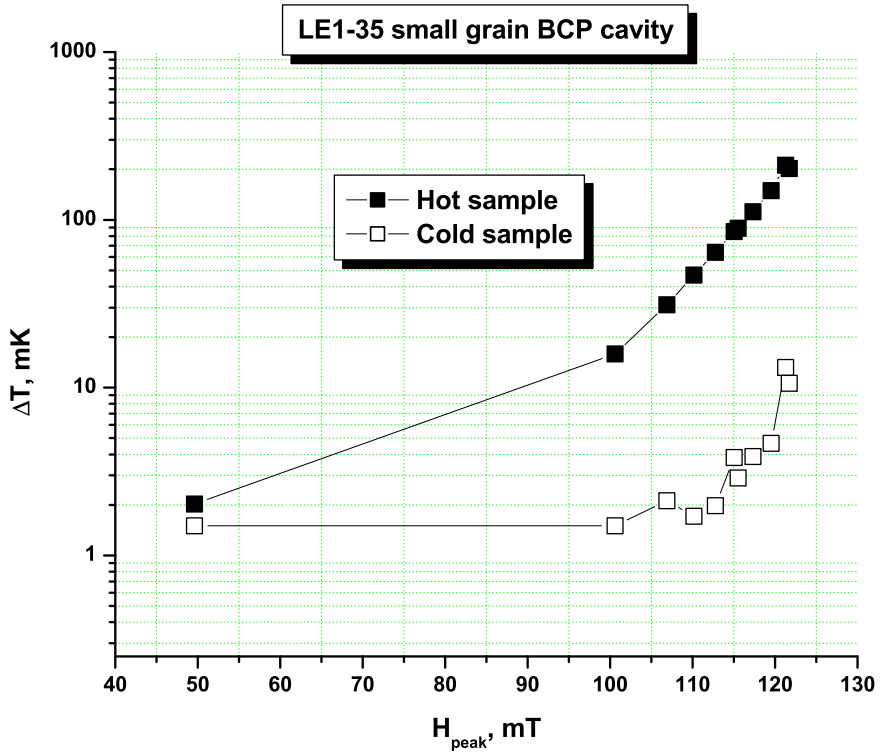

Figure 6.5: Typical ΔT vs. H_{peak} curves for LE1-35 small grain BCP cavity hot and cold samples.

Note that HFQS is present in both hot and cold regions. The ratios of the temperature increase ΔT at the hot areas to the ΔT of the cold areas is about $\Delta T_{hot}/\Delta T_{cold} \approx 2-10$. This ratio will be important later for comparison between small and large grain BCP and EP cavities.

Based on the temperature map (Fig. 6.4)and the interpolated contour plot of the temperature distribution (Fig. 6.6), ten hot and ten cold areas were selected for cutting. Each sample was chosen to span the area covered by two thermometers, so that samples were approximately of a circular shape with the diameter of about 1.5 cm. The contour plot showing the samples selected for

cutting marked by red and white circles for hot and cold areas respectively.

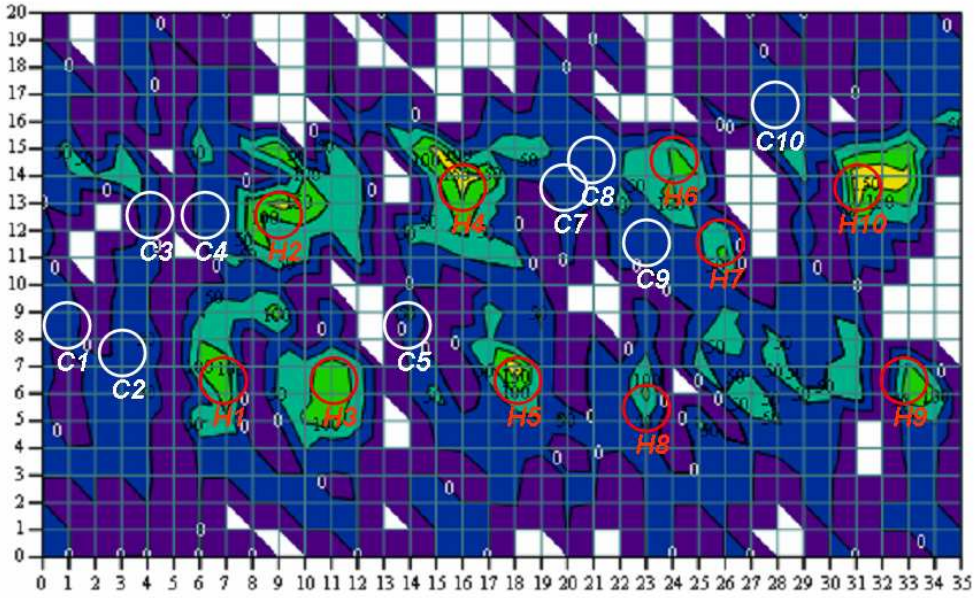

Figure 6.6: The interpolated contour plot of the LE1-35 temperature map at H_{peak}=120 mT. White circles indicate the cold regions, and red circles - hot regions.

6.2.2 Large grain BCP

LE1-37 large grain niobium cavity with the grain size of about 10 cm was BCPed, high pressure rinsed and tested with the thermometry system attached. Results of the RF test are shown in Fig. 6.7. The HFQS started at the peak magnetic field of about $H_{peak} = 100\ mT$. The highest reached field H_{peak} = 130 mT was limited by the available RF power. No X-rays were detected at all field levels.

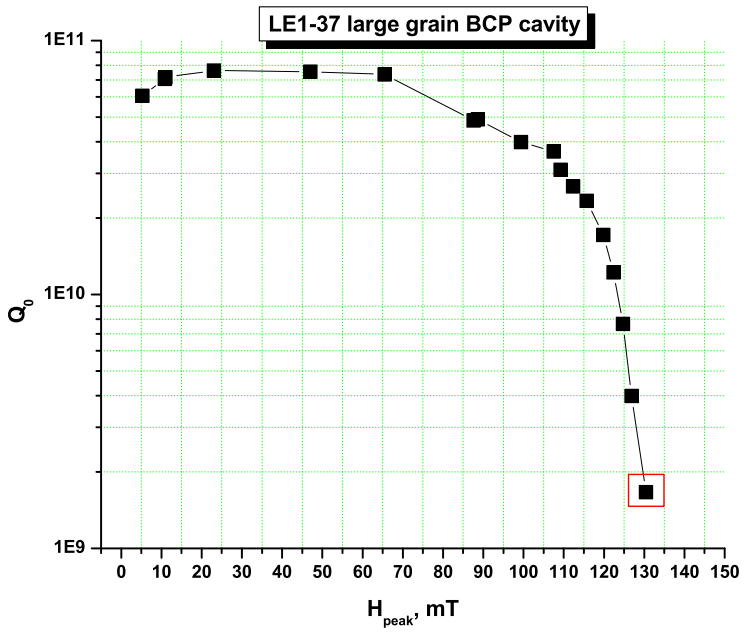

Figure 6.7: LE1-37 cavity quality factor Q_0 versus the peak magnetic field H_{peak}. The red square indicates the point, which corresponds to the temperature map used for dissection.

Temperature maps were obtained at the each field level in the Q vs. H curve and the T-map for the highest field reached (marked by the red square in Fig. 6.7) is presented in Fig. 6.8.

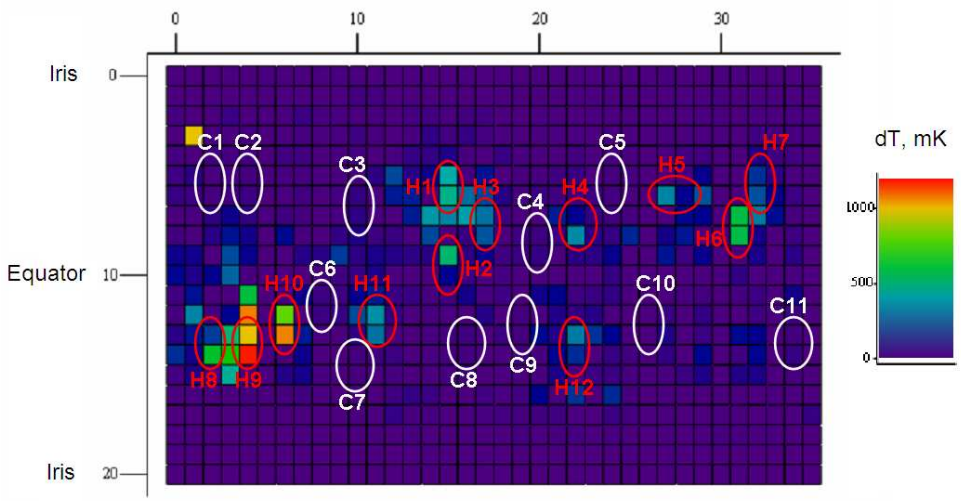

Figure 6.8: The temperature map of the LE1-37 large grain BCP cavity at H_{peak}=130 mT. Areas, which were selected for dissection: white circles - cold regions, red circles - hot regions.

Twelve hot and eleven cold regions were selected for cutting, in Fig. 6.8 hot samples are marked with red circles, and cold samples with white circles. As in the case of the small grain BCP cavity, each sample covered two thermometers. Typical readouts of the temperature sensors in hot and cold regions are shown in Fig. 6.9.

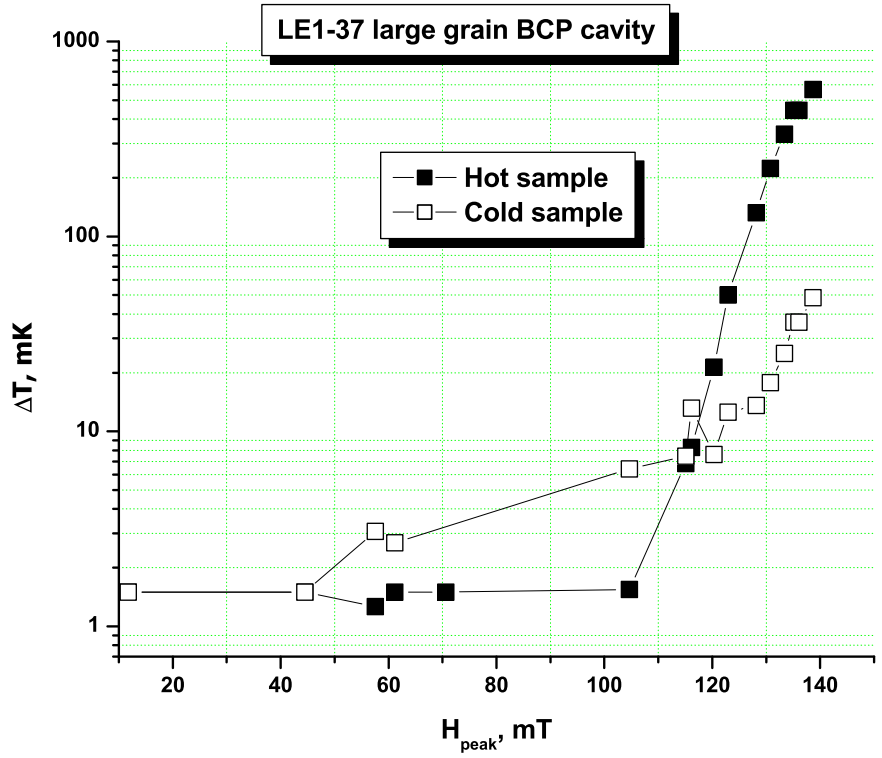

Figure 6.9: Typical ΔT vs. H_{peak} curves for LE1-37 small grain BCP cavity hot and cold samples.

As one can see both from the temperature map (Fig. 6.8)and from the ΔT vs. H_{peak} curves (Fig. 6.9), the hot spots in the large grain BCP case are stronger than in the case of the small grain BCP, whereas cold areas have approximately the same field behavior. The ratio of the maximum temperature increases for the hot and cold samples in the large grain BCP case is $\Delta T_{hot}/\Delta T_{cold} \approx 15 - 25$, which is several times that for the small grain BCP one.

6.2.3 Small grain EP

The small grain LE1-HOR niobium cavity, which had a grain size of about 1 mm, was electropolished, high pressure rinsed and tested with the temperature mapping system attached. The results of the RF test are shown in Fig. 6.10. During the test a field emitter turned on after reaching the peak magnetic field of about H_{peak}=120 mT (E_{peak}=49 MV/m) as was indicated by a significant X-ray radiation level and by the observation of the line heating pattern in the temperature map as is typical of the field emission [9]. But the data obtained by the time of the emitter turn-on was taken in the HFQS regime and was sufficient for selecting hot and cold regions for cutting. Quenching at the field emission site started to happen at the field levels previously reached without it and that was the ultimate limit for the test.

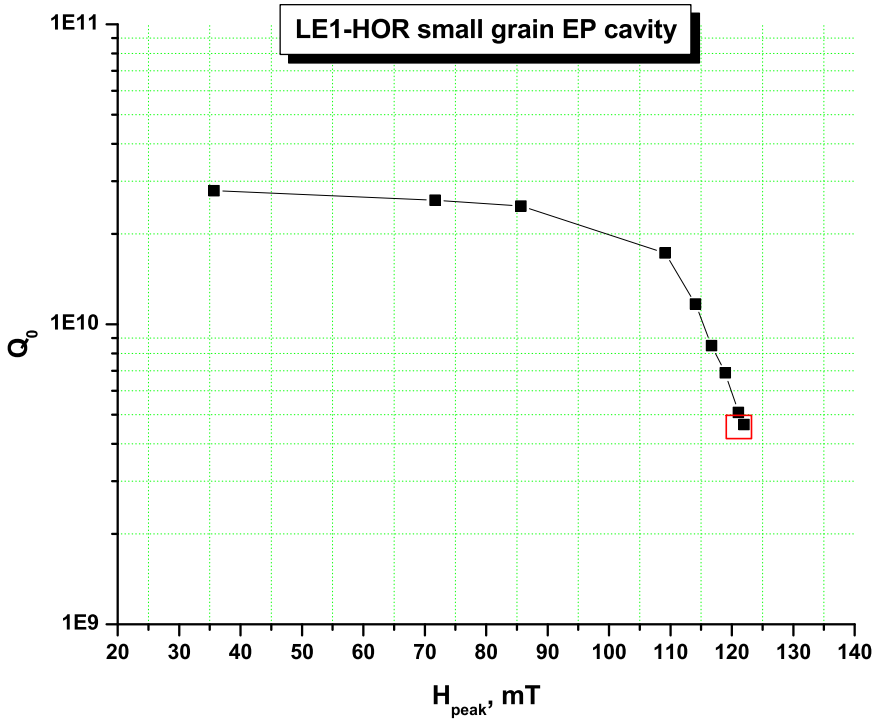

Figure 6.10: LE1-35 cavity quality factor Q_0 versus the peak magnetic field H_{peak}. The red square indicates the point, which corresponds to the temperature map used for dissection.

Four hot and five cold areas were selected for dissection based on the temperature map obtained at the highest field, which is shown in Fig. 6.11. Hot samples are marked with red circles and cold samples with white circles.

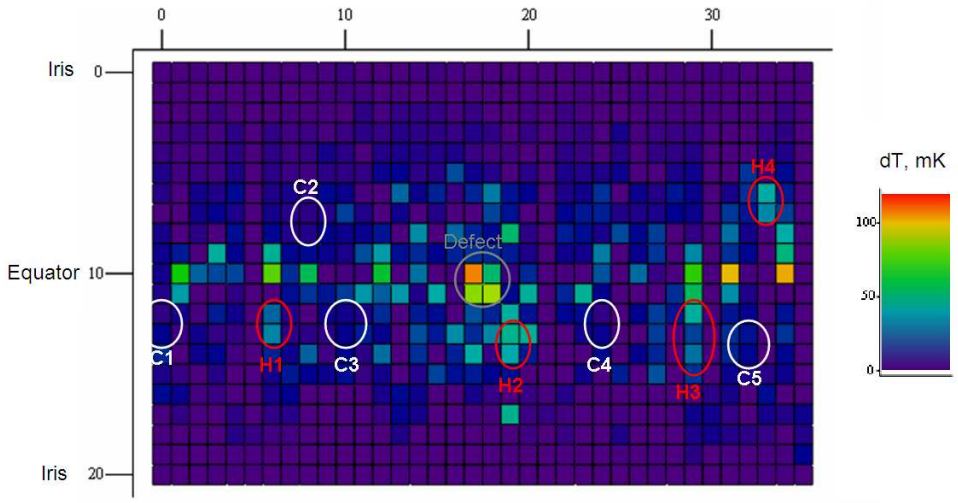

Figure 6.11: The temperature map of the LE1-HOR small grain EP cavity at H_{peak}=120 mT. Areas, which were selected for dissection: white circles - cold regions, red circles - hot regions.

Typical thermometer readings for hot and cold samples are shown in Fig. 6.12.

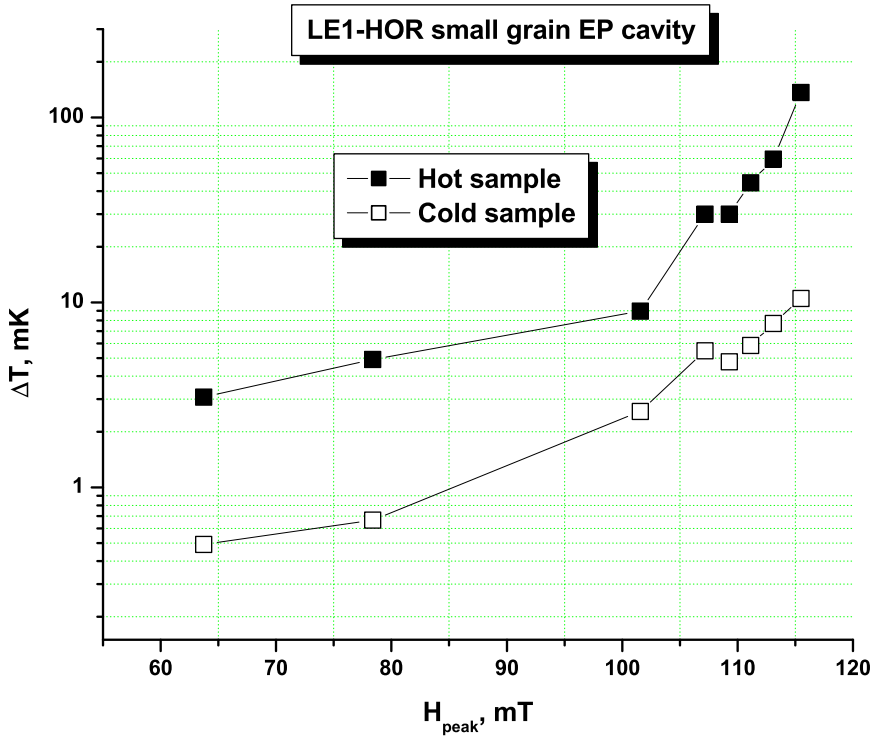

Figure 6.12: Typical ΔT vs. H_{peak} curves for LE1-HOR small grain EP cavity hot and cold samples.

The hot spots in the small grain EP case are comparable to the ones in the small grain BCP case in terms of the maximum temperature increase of about 100 mK. The relative intensities of the hot and cold spots as characterized by the ratios of maximum temperatures are $\Delta T_{hot}/\Delta T_{cold} \approx 4 - 12$, which is similar to the small grain BCP case.

6.2.4 Small grain EP defects

In addition to the high field Q-slope heating, several areas have been identified on the cavity surface by thermometry (Fig. 6.11), which exhibited a pronounced heating starting at lower fields below the high field Q-slope onset. Typical dependencies of ΔT vs. H_{peak} for the defects close to the weld area are shown in Fig. 6.13 in comparison with the same curve for the hot sample (H4).

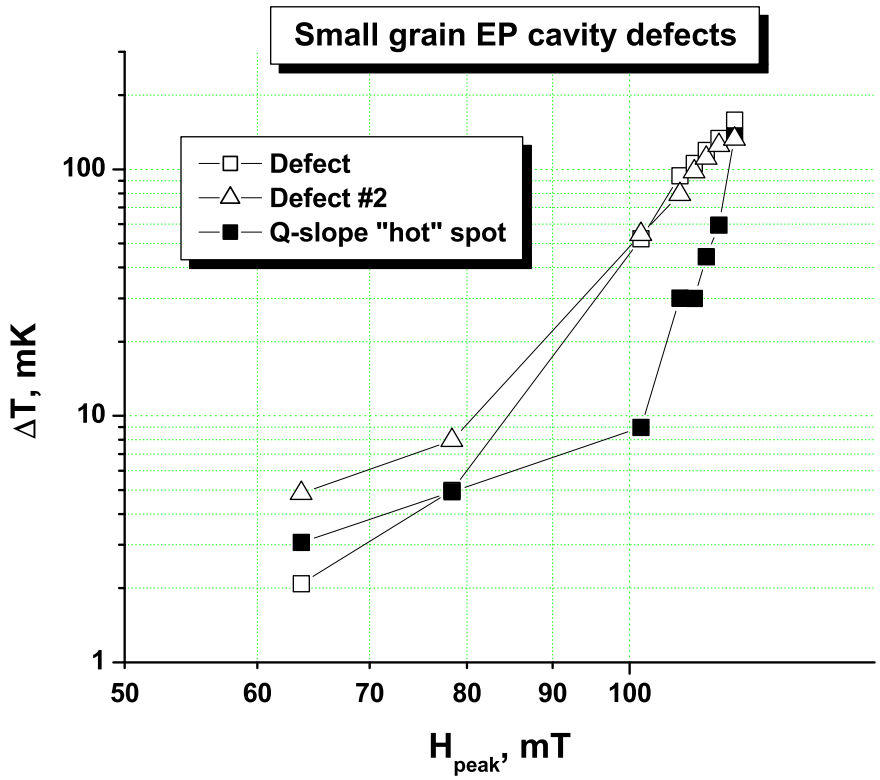

Figure 6.13: Typical ΔT vs. H_{peak} curves for LE1-HOR small grain EP cavity defects near the weld area. Note the difference in the heating between the defects and the HFQS hot spot.

Note the significant difference in the heating of the defect and a hot spot - the former has increased losses already at lower fields, whereas the latter has

almost zero heating up to the HFQS onset field.

Based on the temperature map shown in Fig. 6.11 the defect area marked on the temperature map with the dark gray circle was cut out and analyzed with the SEM. A pit of about 1-1.5 mm in diameter was found on the sample surface, which might have been the cause of the observed heating. Secondary electrons and backscattered electrons images of the pit are shown in Fig. 6.14 and Fig. 6.15 respectively.

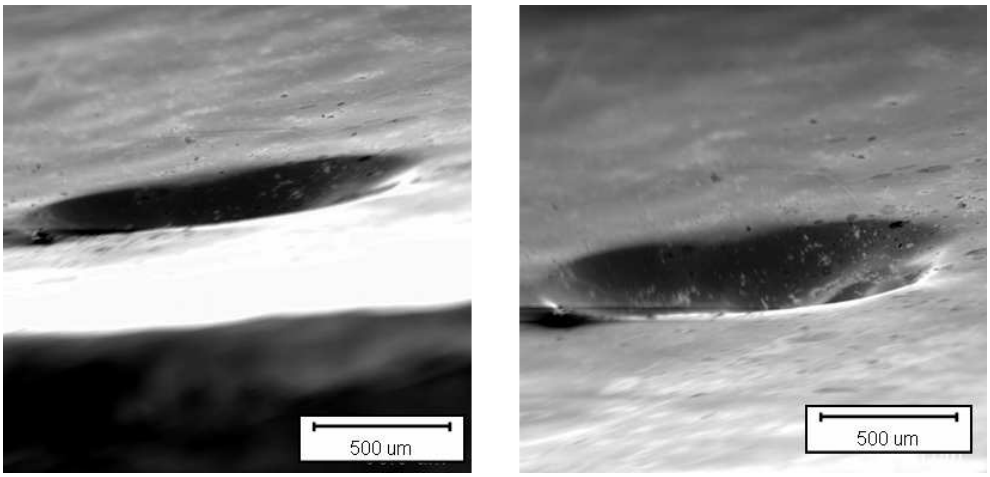

Figure 6.14: Secondary electrons images of the pit identified as a possible cause of heating in the "defect" area of the small grain EP cavity.

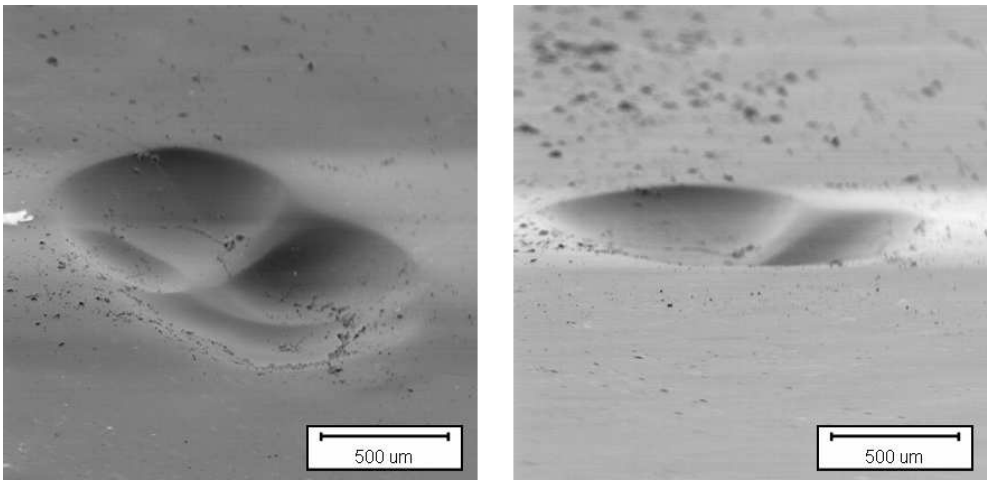

Figure 6.15: Backscattered electrons images of the pit identified as a possible cause of heating in the "defect" area of the small grain EP cavity.

The occurrence of pits near welds has become of high interest in the SRF community. The pre-heating of the pits suggests that part of the pit is normal conducting, or there is other contamination also.

CHAPTER 7

OPTICAL PROFILOMETRY STUDIES

7.1 Introduction

Niobium cavities typically undergo either BCP or EP chemical treatment as one of the steps in the final RF surface preparation. The resulting surface is not perfectly flat but has a finite roughness, with grain boundaries representing the highest steps due to the dependence of the chemical etching rate on the crystalline orientation of the grain. BCP results in the surface, which has larger (5-10 μm) and steeper grain boundary steps, as compared to the EP surface ($<$0.5 μm), as was found by several different studies.

If the step is present on the niobium surface it results in the enhancement of the magnetic field on the step as discussed in the context of the MFE model for the HFQS [14]. Since the enhanced magnetic field could produce a premature local quenching of the grain boundary, a natural explanation for the observed heating non-uniformity of cavity walls in the HFQS regime would be the difference in roughness between hot and cold regions. In order to check this hypothesis the roughness measurements have been performed on the dissected hot and samples to search for any differences. The tool of choice for this purpose was a non-contact optical profilometry.

A white light optical profilometer was used in this thesis work for characterizing the surface roughness of the samples. Its operation is based on the interferometry of light reflected from surface irregularities and the detailed description is beyond this thesis and can be found in [32].

7.2 Experimental data

Several hot and cold samples from the small grain BCP and EP cavities and a small grain EP cavity were analyzed by the optical profilometer. The output data of the optical profilometer is a 3D image of the sample surface, which can be subsequently analyzed by obtaining statistical characteristics such as r.m.s. roughness etc. or extracting additional characteristics such as line profiles.

In comparing roughness of different samples one should distinguish between a microroughness, which is a roughness on the length scale smaller than the grain size, and a macroroughness, which is dominated by the grain boundary steps. Recent studies have shown that the r.m.s. roughness obtained from the data depends on the dimensions of the area analyzed [46].

Typical images of the hot and cold samples obtained by the optical profilometer are shown in Fig. 7.1. The average r.m.s. micro-roughness of the an-

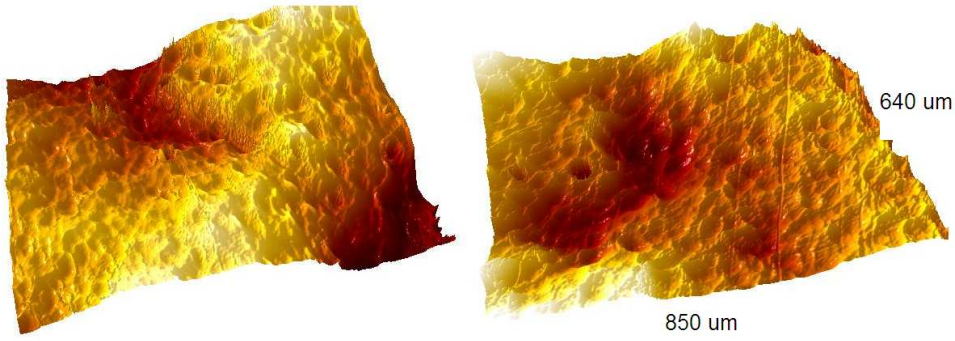

Figure 7.1: Optical profilometer 3-D images (850 μm $\times$ 640 μm) of the hot (left) and cold (right) samples of the LE1-35 small grain BCP cavity.

alyzed samples from both small grain BCP and a small grain EP cavities was about σ=1.5-1.8 μm for both hot and cold samples, thus the micro-roughness

could not be the cause of the different behavior of samples in high RF magnetic fields.

In order to compare the macro-roughness six line profiles were obtained on each sample with each profile spanning about 1 cm in length as compared to the average grain size of 1 mm for the samples. A simple software was developed, which took the line profile as an input, and produced a number of the steps having the step height of 1,2,3,... μm. The resulting data for the small grain BCP cavity samples is summarized in histograms in Fig. 7.2.

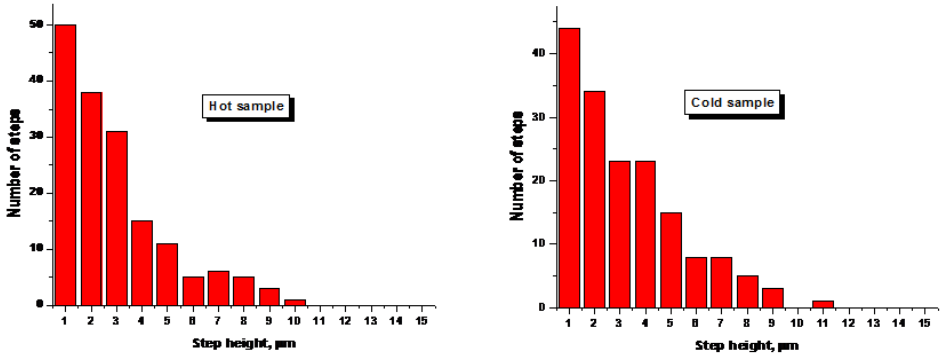

Figure 7.2: Histograms of the step height distributions for the LE1-35 small grain BCP cavity hot and cold samples.

The corresponding data for the small grain EP cavity is shown in Fig. 7.3.

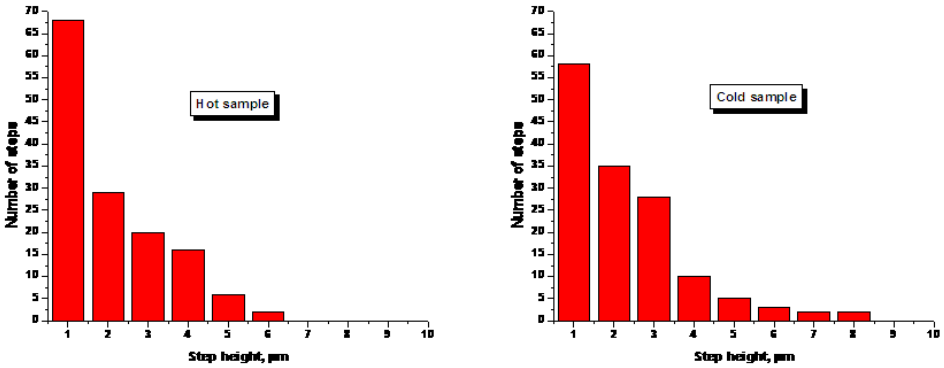

Figure 7.3: Histograms of the step height distributions for the LE1-HOR small grain EP cavity hot and cold samples.

7.3 Conclusion

As the data indicates, in both small grain BCP and small grain EP cases the roughness of hot and cold samples was similar within the grains, and also on the macro-scale of many grains. Therefore the difference between the strong and weak HFQS cannot be attributed to surface roughness, in support of other arguments against roughness as the primary cause of the HFQS. Since temperature mapping data on large grain cavities also indicates that the grain boundaries are not the preferential places for the hot spots [9], we suggest that roughness can be eliminated from the list of possible causes of the HFQS heating distribution. Although roughness might contribute to the overall losses as a secondary mechanism, but is not the primary contributor.

CHAPTER 8

XPS STUDIES

8.1 Introduction

Niobium used for cavity production undergoes several different treatments before it eventually becomes an RF cavity ready for test. After the typical procedures of rolling, mechanical forming, chemical etching and high pressure rinsing of the cavity surface, the structure of the niobium surface can be schematically depicted by the model shown in Fig. 8.1.

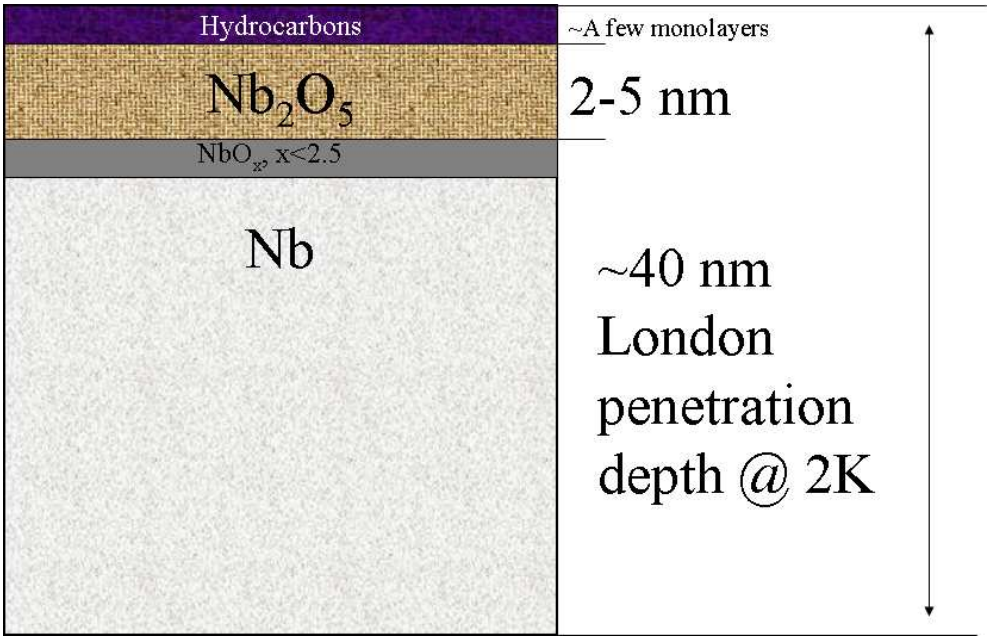

Figure 8.1: Schematic of the niobium surface after typical cavity preparation steps has been performed.

As a relatively reactive metal, niobium after the water rinsing, which follows the chemical etching, is always covered with a 3-5 nm layer of a natural

oxide predominantly in the form of Nb_2O_5. The oxide layer is initially formed during a wet oxidation in water after the chemical treatment such as BCP or EP. The following air exposure of the cavity results in the slow increase of the oxide thickness until the process stops at about 4-5 nm oxide thickness. In the transition region, where the natural oxide meets the bulk niobium, suboxides in the form of NbO and NbO_2 may also be present, although the exact amount is uncertain.

In addition to the oxide, contaminants such as hydrocarbons, water, and chemical residues (F, N, ...) might be present within the first several nanometers of niobium, which can be introduced during chemical etching and other steps of cavity preparation.

Thus, it is important to compare elemental compositions and chemical structures for the hot and cold samples within first several nanometers to check if there are any differences, which might be responsible for their different behavior at high magnetic fields.

A tool, which is suitable to provide this information, is an X-ray Photoelectron Spectroscopy (XPS), also referred to as Electron Spectroscopy for Chemical Analysis (ESCA). In the typical XPS system, such as one shown in Fig. 8.2, a sample is irradiated with the focused X-ray beam of $1 - 2\ keV$ energy, which results in some of the core shell electrons being knocked off as shown in Fig. 8.3.

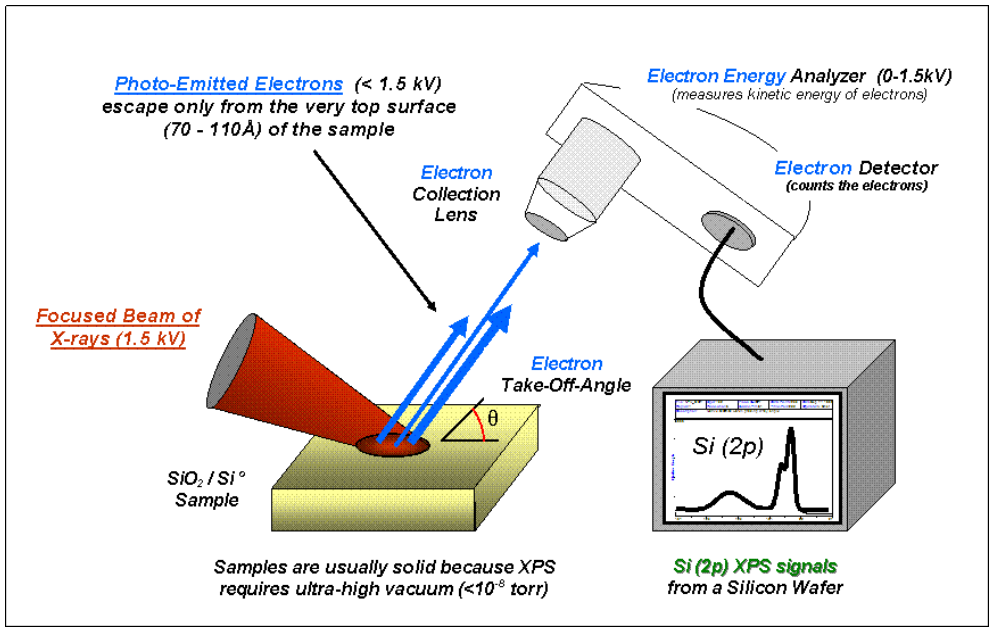

Figure 8.2: Schematic of the typical lab XPS system.

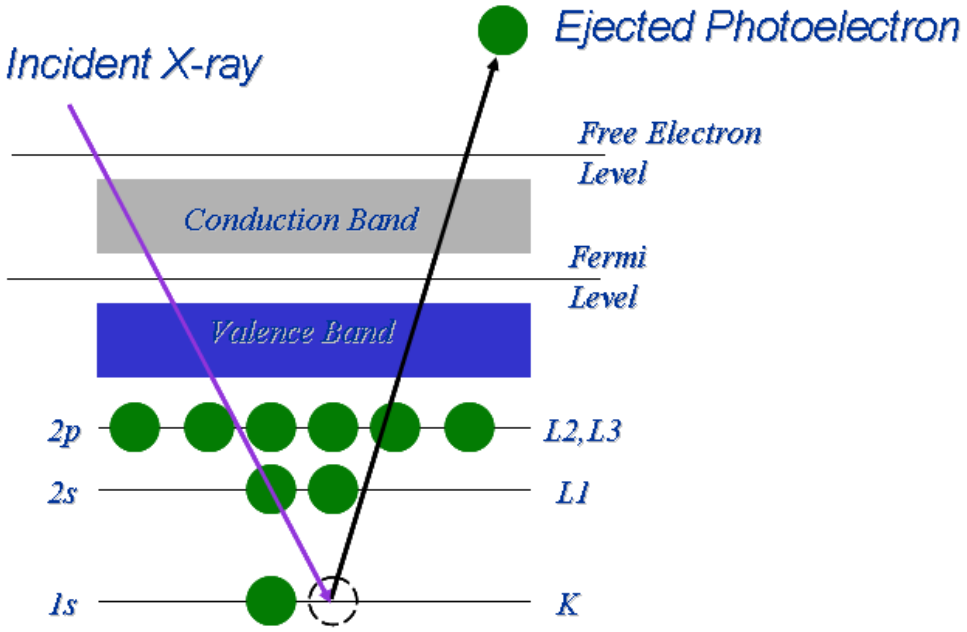

Figure 8.3: Schematic of the photoelectric effect caused by the impinging X-rays in the XPS setup. The resulting photoelectron comes from the 1s shell in this example.

The kinetic energy E_{kin} of the resulting photoelectrons depends on the X-ray beam energy $h\nu$ and the binding energy of the electron E_b within the core shell it was ejected from:

$$E_{kin} = h\nu - E_b \tag{8.1}$$

By collecting the photoelectrons and looking at their kinetic energy distribution it is possible to obtain the distribution of their binding energy if the X-ray beam energy $h\nu$ is known. Binding energies for the elements are known from the literature, which allows a determination of the element each photoelectron originated from. Furthermore, if the originating element of the photoelectron is not free but in a chemically bound state, the binding energy of the electron will be shifted due to the non-zero contribution of the chemical environment to the core shell electron energy. This shift is called a *chemical shift* and is directly measurable by XPS. Chemical shifts for most chemical configurations are available from several databases, i.e. NIST database. XPS can detect all elements except H and He, and the elemental resolution of the typical lab XPS system is about 0.1-1 atomic percent, so that it cannot detect trace impurities with the lower concentration. Previous studies have used XPS data to infer the presence of small quantities of suboxides below the main pentoxide.

Experimentally, photoelectrons are collected by the electron energy analyzer, which separates them based on their kinetic energies. The number of electrons having the kinetic energy within each bin range is counted by the electron detector (Fig. 8.2). Typically, a lower resolution survey over the wide energy window with the bin size of 0.1 eV is used to get information about elements present in the sample. High resolution scans around peaks corresponding to the elements of interest are then performed with the bin size of 0.025 eV to obtain the fine structure of the peaks, which contain the information about the chemical

environment, as described above.

Hot and cold samples from all the cavities, which were dissected, were analyzed using the lab SSX-100 XPS system utilizing the Al Kα X-ray source of 1486.6 eV energy. The angle between the electron energy analyzer and a sample normal was fixed at 55°. The radius of the spot for the X-ray beam was 800 μm.

Photoelectrons have the limited escape depth due to their interaction with the atoms constituting the sample, which is dependent on the inelastic mean free path (IMFP) λ. The information depth d_0, which is the escape depth of photoelectrons, is generally defined to be $d_0 = 3\lambda$. The IMFP is calculated using the simulation software and for photoelectrons resulting from the 1486.6 eV X-rays in niobium the information depth was calculated to be about 7 nm, which covers the oxide and the oxide/metal interface.

8.2 Small grain BCP cavity samples

All samples have been analyzed by the same procedure using the lab XPS system described above. For each sample several measurements have been performed at three different spots at the sample surface:

- A low resolution survey spanning the electron binding energies from 0 to 1000 eV for general analysis of the elements present
- The high resolution spectra acquisition for C 1s, O 1s, N 1s, Nb 3d, and a valence band for the information on chemical bonding

General XPS surveys revealed that three out of ten hot samples had a strong N 1s signal present in the survey at the level of a few atomic percents. An example of the survey from one of the hot samples containing nitrogen is shown in Fig. 8.4. The corresponding typical survey for cold samples is shown in Fig. 8.5. One can notice that in the hot sample survey the N 1s peak is present at about 401 eV binding energy whereas the cold one does not have it.

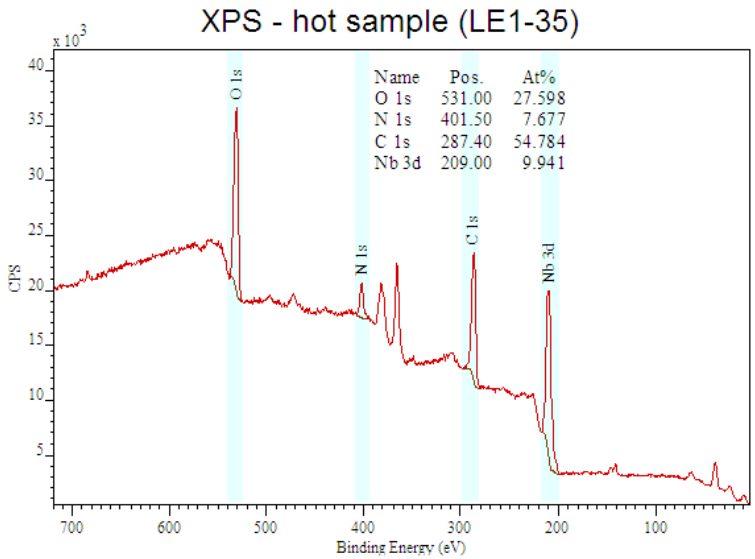

Figure 8.4: XPS survey for the LE1-35 hot sample. Notice a strong N 1s peak indicating the presence of nitrogen in the first 7 nm of the sample.

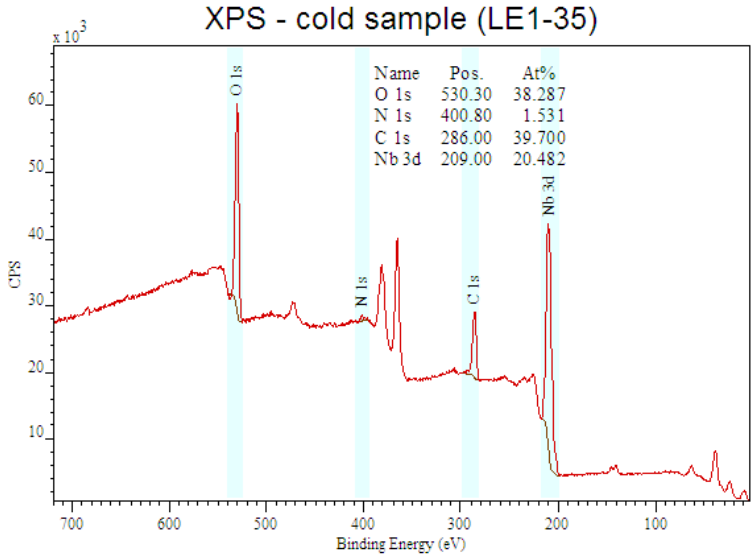

Figure 8.5: XPS survey for the LE1-35 cold sample. Notice the absence of a N 1s peak.

The N 1s peak at 401 eV might correspond to the adsorbed $NO^{\delta-}$ [31], which can be introduced during the BCP treatment where nitric acid HNO_3 is one of the BCP solution constituents.

For the analysis of the niobium oxide structure the high resolution spectrum around Nb 3d peak was obtained for all samples. Typical data for hot and cold samples is shown in Fig. 8.6. No difference within the instrument resolution was observed in the oxide structure of all hot and cold samples.

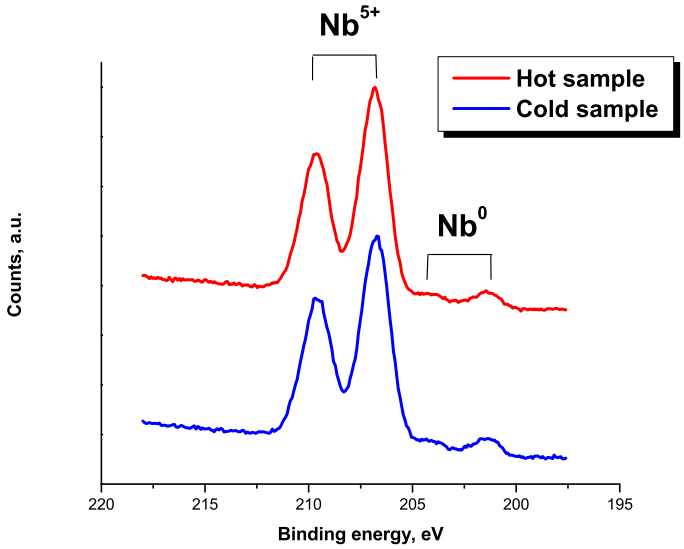

Figure 8.6: XPS Nb 3d peak for the LE1-35 large grain BCP cavity hot and cold samples.

In addition to the lab XPS analysis, a collaboration with Joseph Woicik from BNL National Synchrotron Light Source (NSLS) was established to obtain the XPS spectra using the synchrotron X-ray source, which provides a greater energy resolution and a higher energy of the X-ray beam. The X-ray beam with the higher energy produces photoelectrons with the higher kinetic energy as follows from Eq. (8.1). The higher kinetic energy of the photoelectrons in turn translates into the higher escape depth. XPS spectra acquisition was performed using the X-ray energy of 2139 eV, which provides information about first 10 nm of the niobium surface, as compared to only 7 nm for the lab XPS system. Thus, for the synchrotron energy used, the XPS spectrum is less dominated by the niobium oxide signal, but includes a significant contribution from about 6 nm of bulk niobium underneath the oxide.

The resulting XPS spectra obtained on the hot and cold samples are shown in Fig. 8.7.

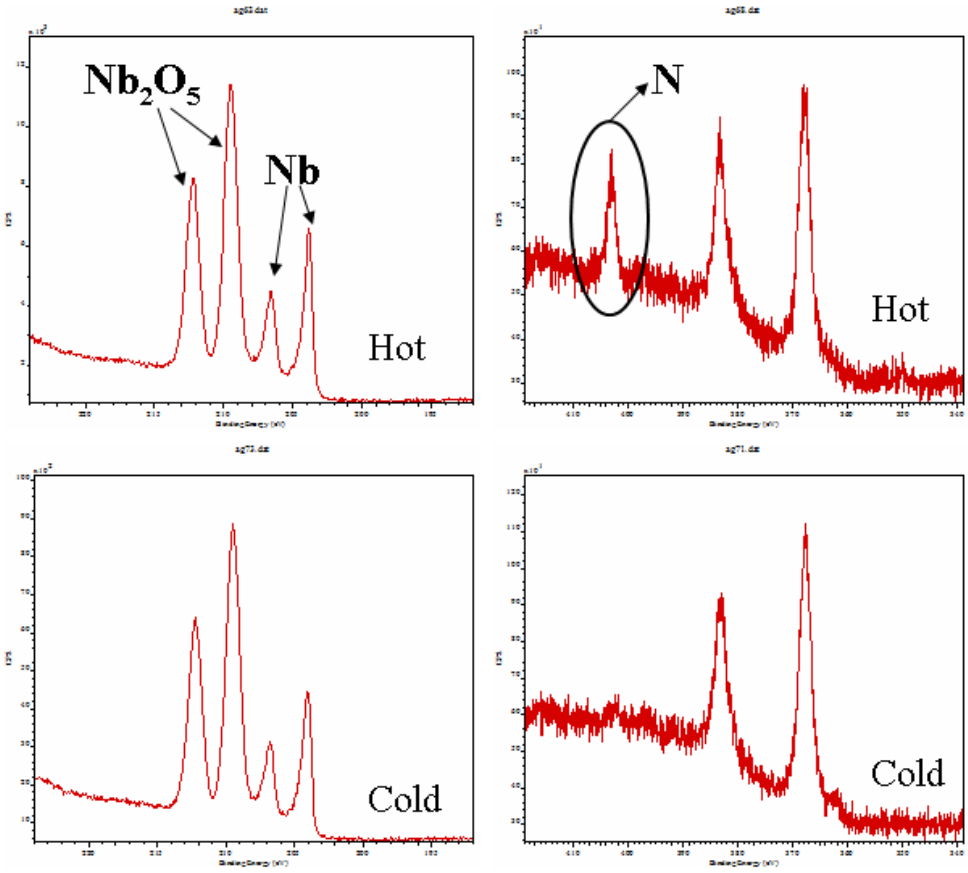

Figure 8.7: XPS spectra for the LE1-35 hot and cold samples obtained using the synchrotron X-rays of 2139 eV. Left panel shows the Nb 3d spectra, and the right panel shows the high resolution surveys around the N 1s peak. Measurements by J. Woicik (NSLS).

The obtained spectra confirmed the conclusion reached after analyzing the lab XPS data that the niobium oxide structure is identical in hot and cold samples, and the only difference inferred from XPS investigations is the presence of nitrogen in the hot sample.

8.2.1 Baking of the nitrogen-containing samples

In order to study the effect of the mild baking on the nitrogen signal, one of the nitrogen-containing hot samples from the small grain BCP cavity was baked in UHV at 110°C for 48 hours and re-examined by the lab XPS. In all three spots of the sample surface, which were analyzed after mild baking, the nitrogen signal was either significantly reduced or disappeared completely as shown in Fig. 8.8-8.9.

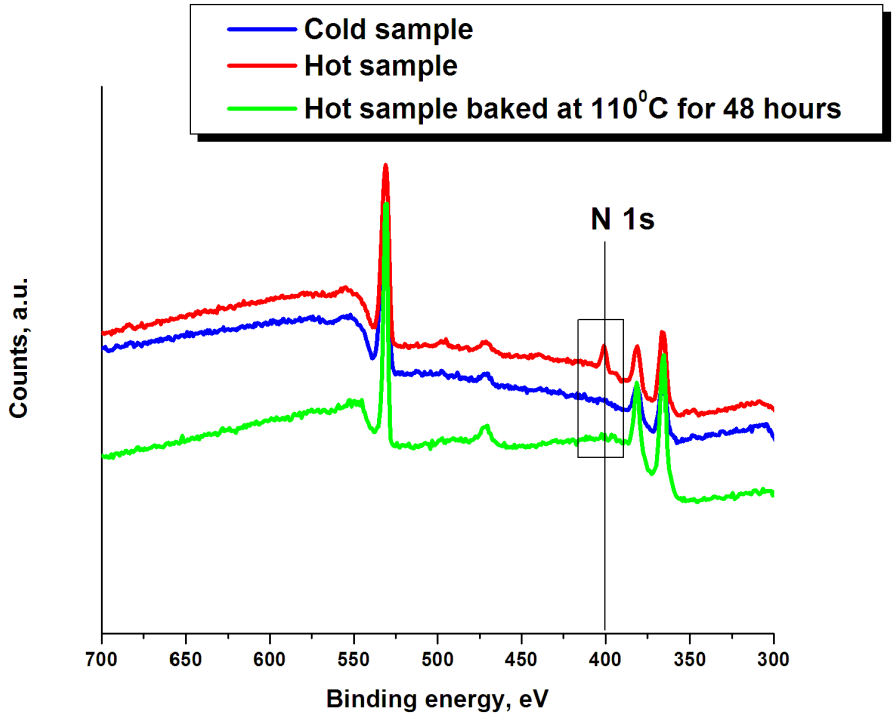

Figure 8.8: XPS surveys for the hot, cold, and baked hot samples of the LE1-35 small grain BCP cavity. Notice the disappearance of the nitrogen signal after 110°C baking.

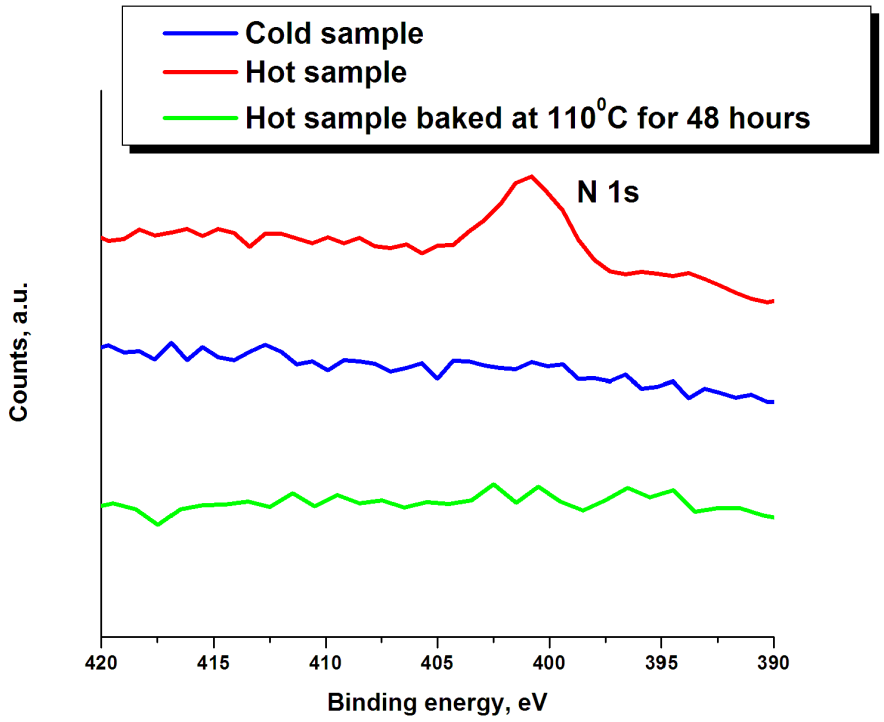

Figure 8.9: N 1s XPS peak for the hot, cold, and baked hot samples of the LE1-35 small grain BCP cavity. Notice the disappearance of the nitrogen signal after 110°C baking.

8.2.2 Angle-resolved XPS studies

In order to study the distribution of nitrogen within the information depth of the XPS signal the angle-resolved technique was implemented in the lab XPS system. The schematic of the typical ARXPS setup is shown in Fig. 8.10.

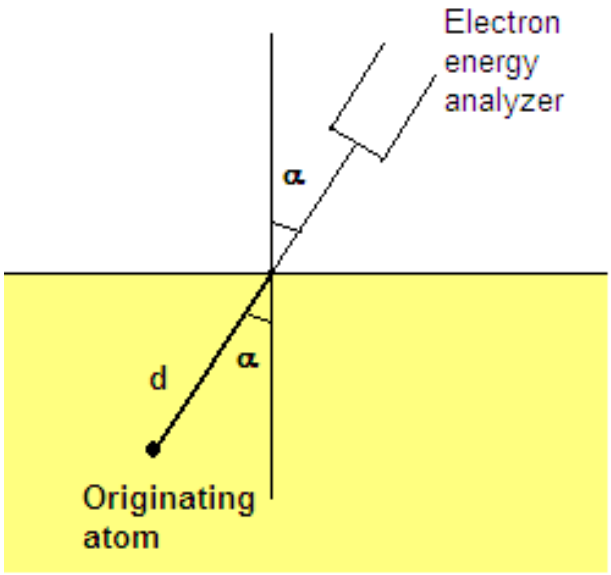

Figure 8.10: Schematic of the typical ARXPS setup.

The angle-resolved XPS (ARXPS) is based on the dependence of the maximum depth, from which the photoelectrons are reaching the analyzer, on the angle between the electron energy analyzer axis and a sample normal:

$$d = d_0 \times cos\alpha \tag{8.2}$$

where d_0 is the maximum escape depth of photoelectrons reaching the analyzer if it is at 0° angle with the sample normal, and α is the angle between the electron analyzer axis and the sample normal. The maximum escape depth d_0 is determined by the photoelectron kinetic energy, which in turn depends on the X-ray beam energy and the binding energy of the electron shell the photoelectron is originated from as follows from Eq. (8.1).

By measuring XPS spectra at different angles between the electron analyzer and the sample normal it is possible to reconstruct the depth profile using the Eq. (8.2).

Both hot and cold samples were investigated using the ARXPS and the nitrogen depth profiles obtained are shown in Fig. 8.11.

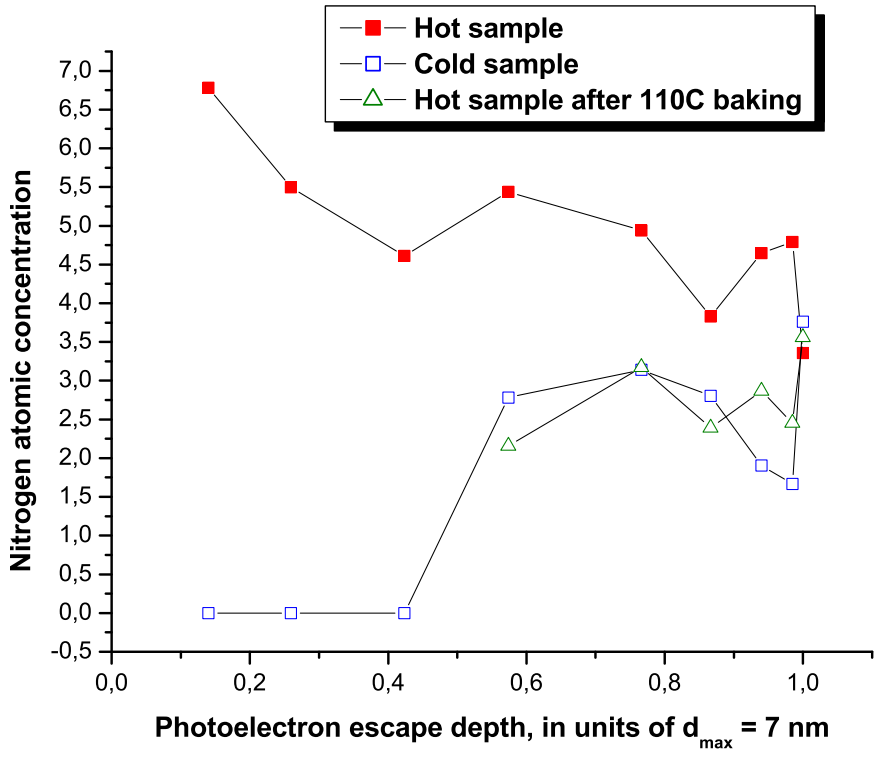

Figure 8.11: ARXPS depth profile of the nitrogen atomic concentration in the LE1-35 small grain BCP cavity samples.

One can notice that in the hot sample nitrogen is almost uniformly distributed throughout the oxide and oxide/metal interface, and after mild baking the nitrogen level is significantly reduced to about the level of it in the cold sample.

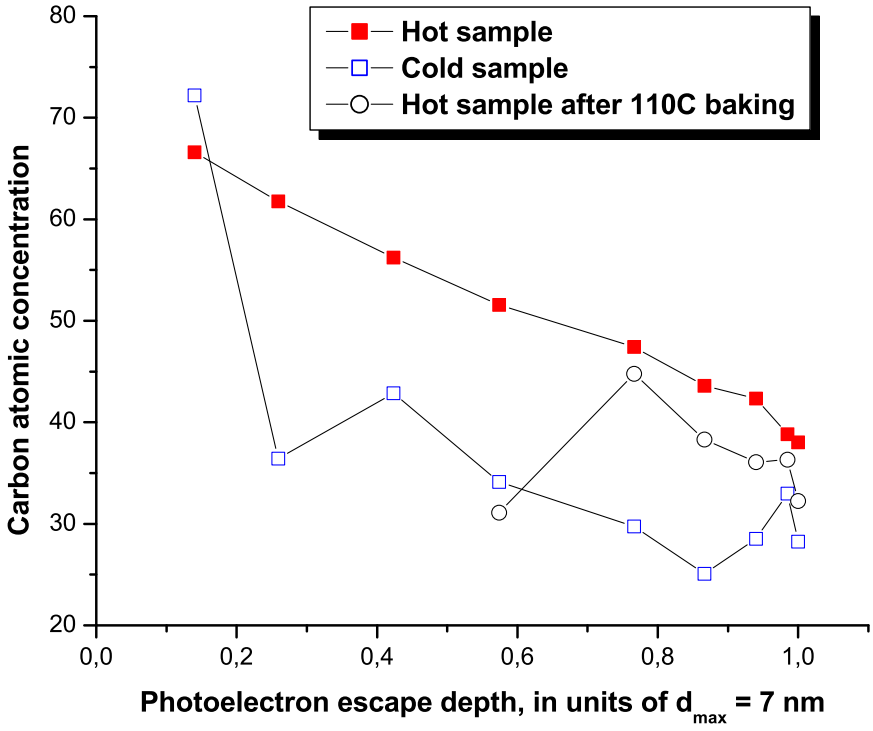

Figure 8.12: ARXPS depth profile of the carbon atomic concentration in the LE1-35 small grain BCP cavity samples.

Carbon profiles before and after mild baking show that the carbon concentration almost did not change. But one should be careful with the carbon concentration interpretation since carbon is a common contaminant, which is inevitably present on the surface of samples in the form of hydrocarbons, and its concentration depends strongly on the handling history of the sample and also varies significantly over the surface of the sample.

8.3 Large grain BCP cavity samples

The analysis of the large grain BCP cavity samples was performed using the lab XPS system described above. Lower resolution wide energy surveys did not reveal any nitrogen or other contaminants presence in both hot and cold samples except for the expected set of peaks for C, O, and Nb. In Fig. 8.13- 8.14 typical XPS surveys for hot and cold samples are shown.

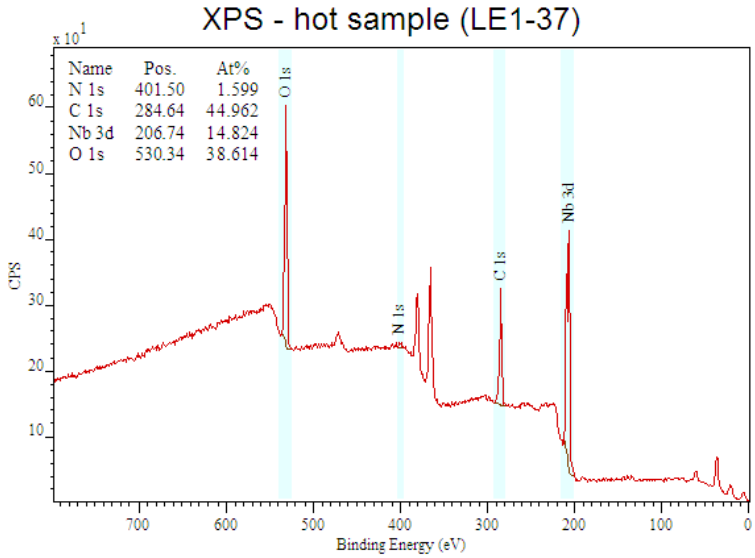

Figure 8.13: XPS survey for the LE1-37 large grain BCP cavity hot sample.

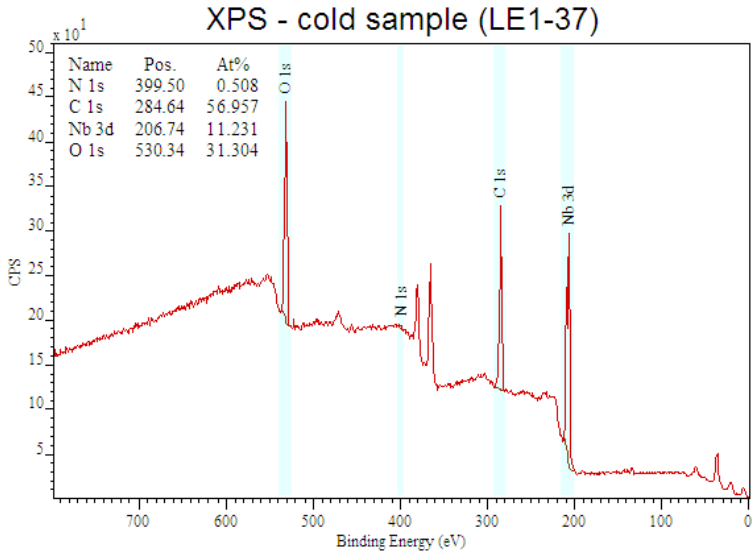

Figure 8.14: XPS survey for the LE1-37 large grain BCP cavity cold sample.

There was no difference observed in the elemental composition of the hot and cold samples within the resolution of XPS, which is about 1 atomic percent as mentioned above.

High resolution scans around the Nb 3d peak at $E_b = 202\ eV$ for all of the hot and cold samples resulted in almost exactly same spectra. Typical results obtained for the hot and cold samples are shown in Fig. 8.15-8.16. One can see that there is no difference in the fine structure of the peaks, and thus the niobium oxide structure is same in both hot and cold samples and it cannot be responsible for the HFQS heating patterns in the large grain niobium cavities.

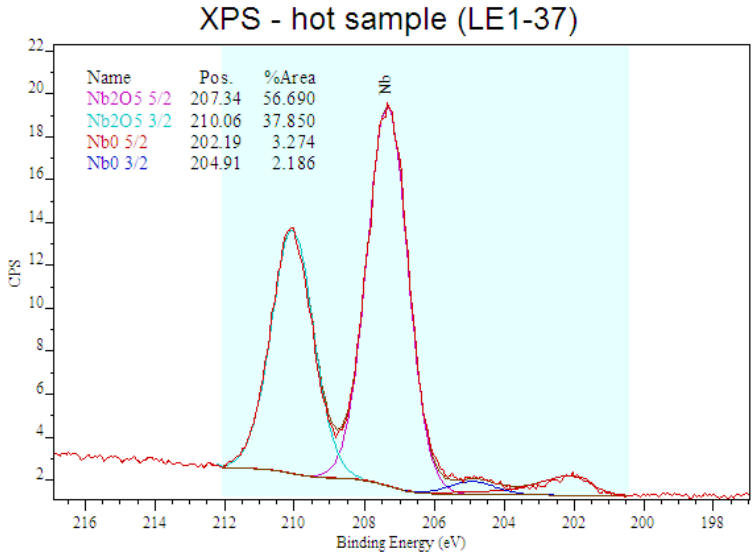

Figure 8.15: XPS Nb 3d peak for the LE1-37 large grain BCP cavity hot sample.

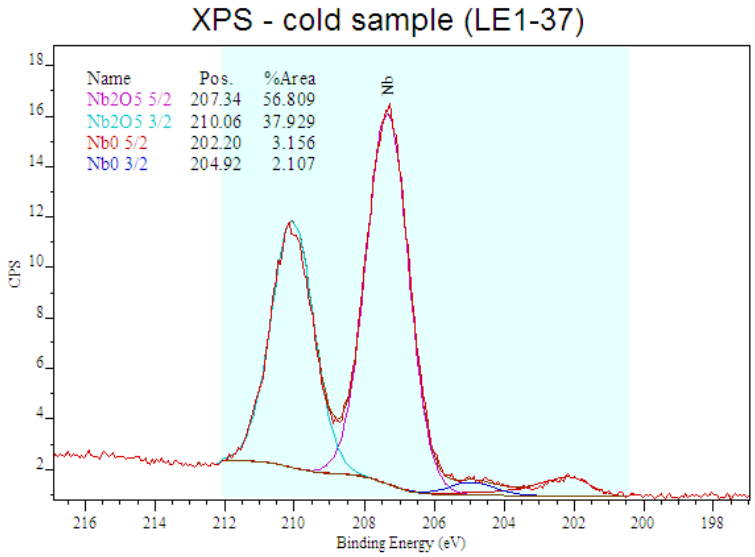

Figure 8.16: XPS Nb 3d peak for the LE1-37 large grain BCP cavity cold sample.

In addition to the high resolution scans around main elemental peaks, very low binding energy electrons coming from the valence band were analyzed to

study the oxidation states. Typical results for the hot and cold samples are shown in Fig. 8.17- 8.18. Since the valence band spectrum is unique for each particular elemental composition and its oxidation state, we can once again see that there is no difference in the chemical structure of the hot and cold samples.

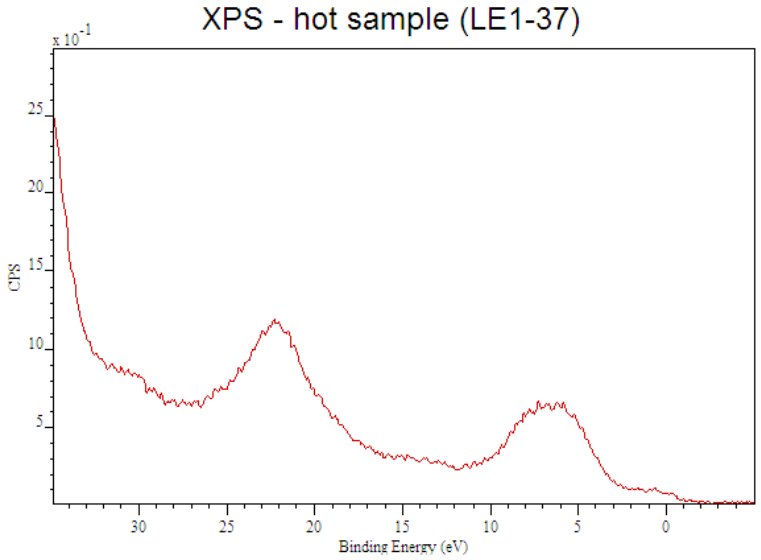

Figure 8.17: XPS valence band spectrum for the LE1-37 large grain BCP cavity hot sample.

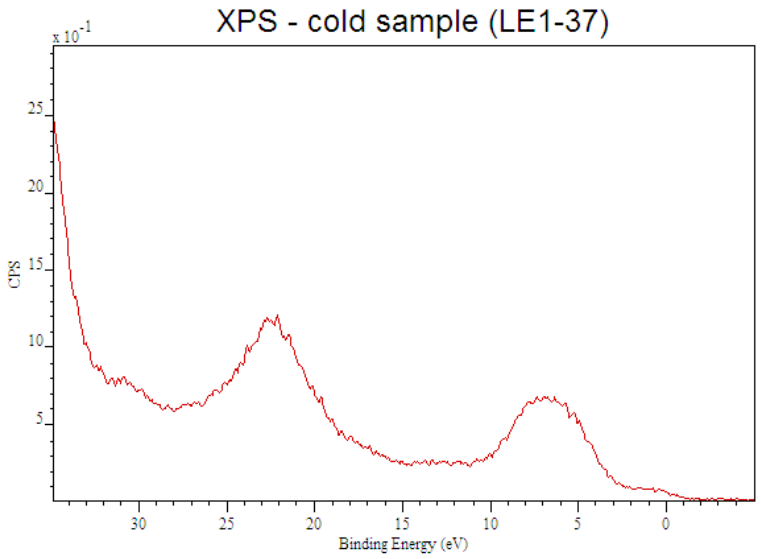

Figure 8.18: XPS valence band spectrum for the LE1-37 large grain BCP cavity cold sample.

8.4 Small grain EP cavity samples

Hot and cold samples from the LE1-HOR small grain EP cavity were analyzed using the lab XPS system using the same procedure as for the two previously discussed cavities.

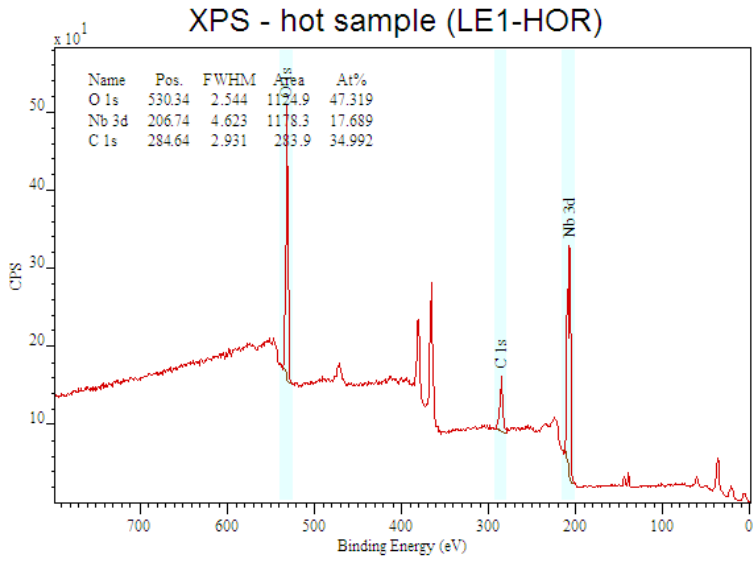

Figure 8.19: XPS survey for the LE1-HOR small grain EP cavity hot sample.

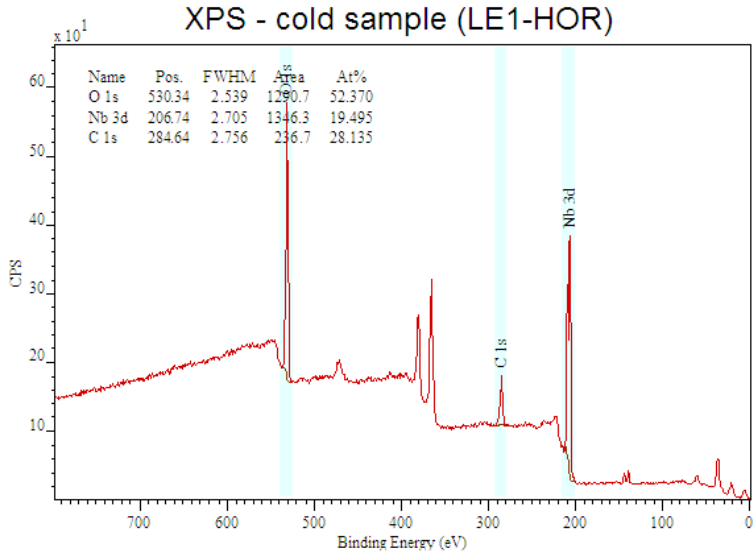

Figure 8.20: XPS survey for the LE1-HOR small grain EP cavity cold sample.

In the low resolution wide energy surveys no excess contaminants were found, with only expected Nb, O, and C signals present in the spectrum. Typical

XPS surveys for the hot and cold samples are shown in Fig. 8.19-8.20.

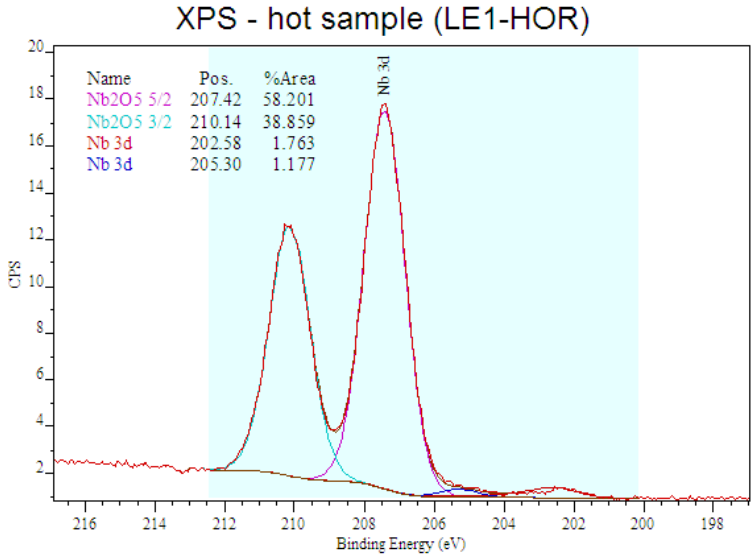

Figure 8.21: XPS Nb 3d peak for the LE1-HOR small grain EP cavity hot sample.

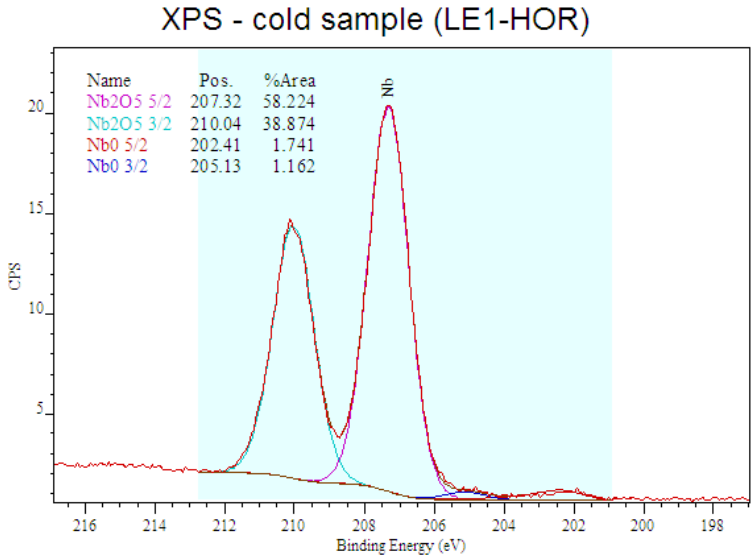

Figure 8.22: XPS Nb 3d peak for the LE1-HOR small grain EP cavity cold sample.

As in the cases of small and large grain BCP samples, the comparison of the

Nb 3d spectra for all hot and cold samples revealed no difference in the oxide structure. Typical Nb 3d spectra for the hot and cold samples are shown in Fig. 8.21-8.22.

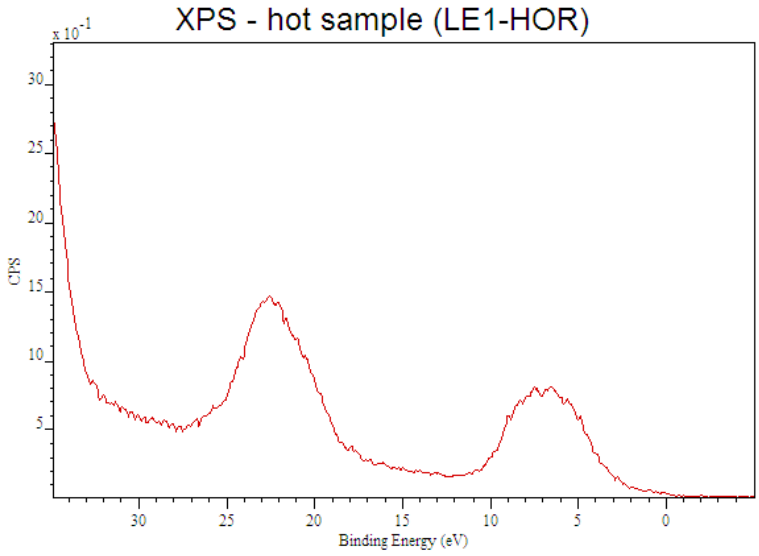

Figure 8.23: XPS valence band spectrum for the LE1-HOR small grain EP cavity hot sample.

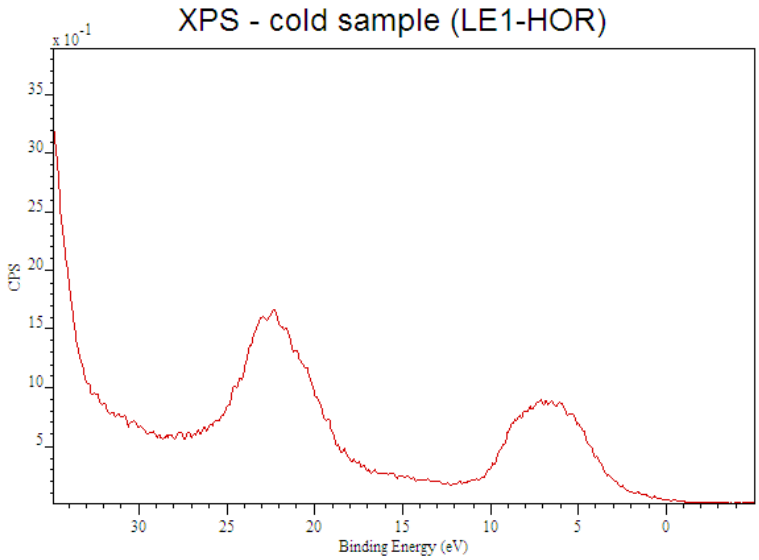

Figure 8.24: XPS valence band spectrum for the LE1-HOR small grain EP cavity cold sample.

The valence band spectrum of the hot and cold samples was very similar as shown in Fig. 8.23-8.24.

8.5 Discussion

The XPS experimental data obtained on the samples from all three dissected cavities allows several conclusions, which address the widely discussed possibility of the niobium oxide role in the HFQS and the heating patterns at the high magnetic fields in the HFQS regime.

Since the $Nb3d$ high resolution spectra obtained on all hot and cold samples appear to be identical, we argue that the difference in the niobium oxide structure is not responsible for the HFQS heating patterns. Furthermore, since baking of the niobium samples did not reveal any change in the oxide structure,

we suggest that the oxide can be ruled out as a possible cause of the HFQS as well. This conclusion was also confirmed by the XPS studies reported in [12], where it was shown that samples after baking and air exposure have exactly same oxide structure as before baking. Valence band spectra obtained on hot and cold samples from large grain BCP and small grain EP cavities confirm that the chemical state of niobium is the same in the samples, at least at the level of XPS sensitivity.

In the case of non-oxygen contaminants, in the small grain BCP cavity it was discovered that hot samples, which exhibited the highest temperature increase during the RF test in the HFQS regime, contained a strong nitrogen signal present within the first 7-10 nm of the surface. Mild baking of the nitrogen-containing sample resulted in the disappearance of the nitrogen signal in the XPS spectrum. If we assume that the mechanism of the nitrogen motion during mild baking is the bulk diffusion, than the observed change is not possible due to a small value of the nitrogen diffusion length as calculated from its bulk diffusion coefficient found in the literature [1]. But it is known that the diffusion of impurities such as nitrogen can go through grain boundaries or dislocations at a much higher rate than through the bulk, which we suggest might be happening in our case for the diffusion of N from the oxide into the bulk.

The "oxide purifier" model proposed recently for the mild baking effect [9] requires the carbon concentration after mild baking to increase in the oxide layer, since carbon is suggested to diffuse from the bulk niobium into the oxide. But ARXPS experiments show that carbon distribution before and after mild baking of the hot sample does not appear to change much at the 4-7 nm depth, which contradicts the model.

CHAPTER 9

EBSD STUDIES ON CAVITY SAMPLES

9.1 Introduction

Niobium is a crystalline material with the body-centered cubic (BCC) lattice structure. In general in any crystalline body different types of crystalline defects are inevitably present, i.e.

- Point defects: vacancies, substitutional impurities, interstitial impurities
- Linear defects: dislocations (edge, screw and mixed types)
- Planar defects: grain boundaries, interfaces
- Bulk defects: precipitates, voids, cracks

Crystalline microstructure of type II superconductors within London field penetration depth λ is known to have an important effect on a multitude of magnetic flux penetration and flux motion phenomena in the superconducting state, such as flux flow, flux pinning, flux creep etc. Thus it is important to analyze hot and cold samples with the tool that provides information about the microstructure in order to elucidate any difference, which might be responsible for the HFQS heating patterns.

Such a tool, which was developed recently, is an Electron Backscatter Diffraction (EBSD).

9.1.1 Dislocations

A dislocation is a linear defect of the crystalline lattice. There are two basic types of dislocations: *edge* and *screw*. In order to visualize ideal dislocations the following procedure is usually suggested: make a cut into an ideal crystal along some plane (Fig. 9.1), then the *dislocation line* is by definition $\vec{t}$, displace atoms by a lattice vector along the direction perpendicular or parallel to the cut plane, "weld" the crystal back together. The resulting distortion is an edge dislocation if $\vec{b} \perp \vec{t}$ and a screw dislocation if $\vec{b} \parallel \vec{t}$.

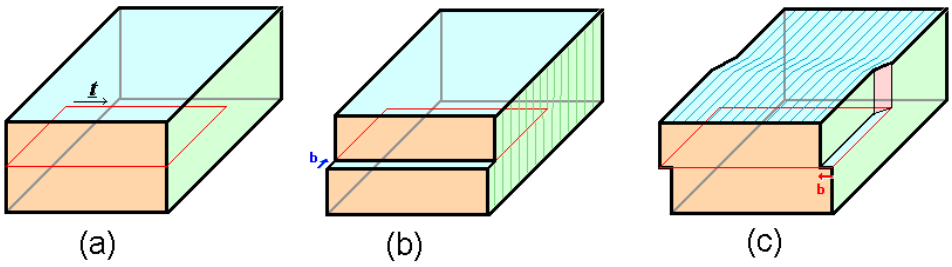

Figure 9.1: (a) Cutting plane determines a dislocation line vector $\vec{t}$; (b) displacement of the lattice for edge dislocations: $\vec{b} \perp \vec{t}$; (c) $\vec{b} \parallel \vec{t}$ for screw dislocations.

In Fig. 9.2 a 3D view of an ideal edge dislocation is shown. One can see that an edge dislocation might be interpreted as a missing atomic half-plane in the crystal.

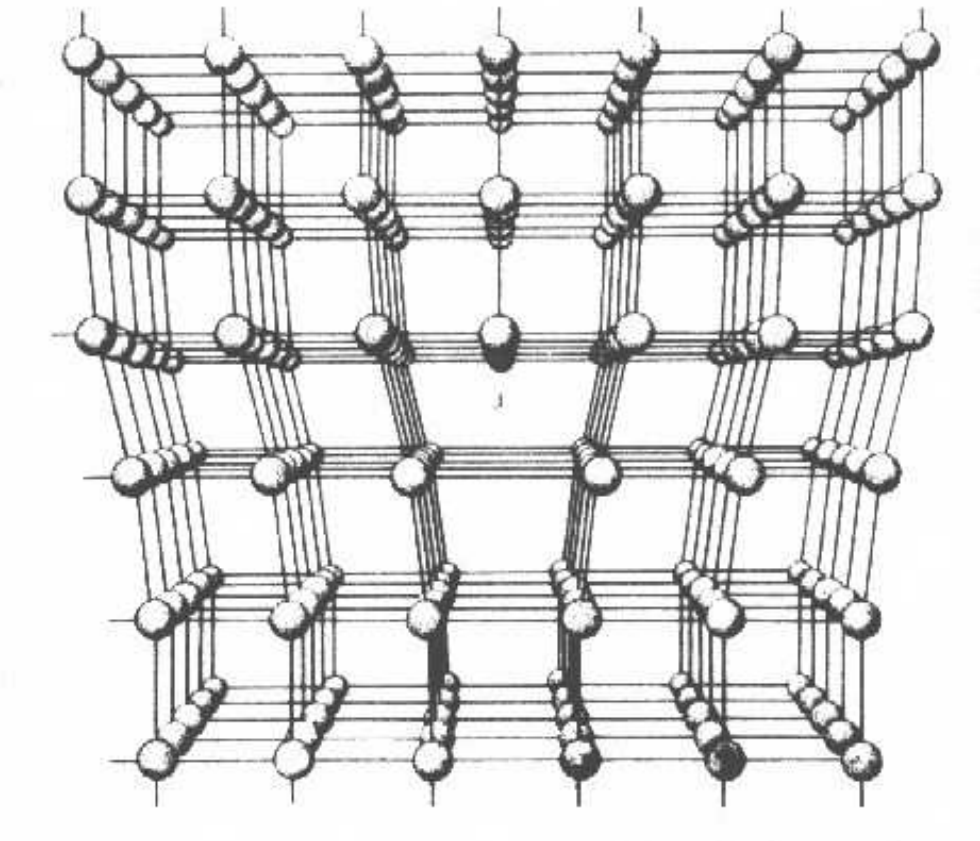

Figure 9.2: 3D-view of an ideal edge dislocation.

Each dislocation can be mathematically characterized by two vectors:

- Burger's vector $\vec{b}$, which describes the difference in atomic positions resulting from crossing the dislocation line.
- Dislocation line vector $\vec{t}$.

Though in real materials dislocations are not only of two extreme cases (edge and screw) but can be of any type determined by the angle between $\vec{b}$ and $\vec{t}$. These dislocations are called to be of a *mixed* type. Edge and screw dislocations are in fact just special cases of a $0°$ and $90°$ angle between Burger's vector $\vec{b}$ and a dislocation line $\vec{t}$.

As was shown at the dawn of dislocation theory [45, 34, 37] by studies of solid materials under applied stress, any plastic deformation of crystalline bodies is accommodated by dislocations, which are created during deformation and their motion allows to preserve the crystal continuity while accommodating the change of geometrical dimensions.

9.2 Electron back-scattered diffraction

Electron back-scattered diffraction (EBSD) is a recently developed technique, which relies on the diffraction of backscattered electrons from the sample surface for identifying the crystalline lattice structure. An EBSD system is usually built upon the existing scanning electron microscope (SEM) system. The sample is typically mounted within the SEM chamber with the angle of about 70° made between the electron beam and a sample surface normal. Backscattered electrons are captured by a phosphorous screen, with the resulting diffraction pattern of Kikuchi bands produced. Detailed description of the physics behind Kikuchi bands formation is beyond the scope of this thesis and can be found in [44]. The image on the screen is captured by a fast camera, and then analyzed by the software that indexes Kikuchi bands assigning a crystalline orientation $\mathbf{g}_{ij}$ to the observed diffraction pattern based on the material parameters such as unit cell length. Each measurement in modern EBSD systems takes about 0.1-0.5 seconds. Moving the beam across the analysis area in a regular pattern (e.g. square or hexagonal) with orientation measurements at each spot produces a 2D-map of crystalline orientations. A schematic of a typical EBSD system setup is shown in Fig. 9.3.

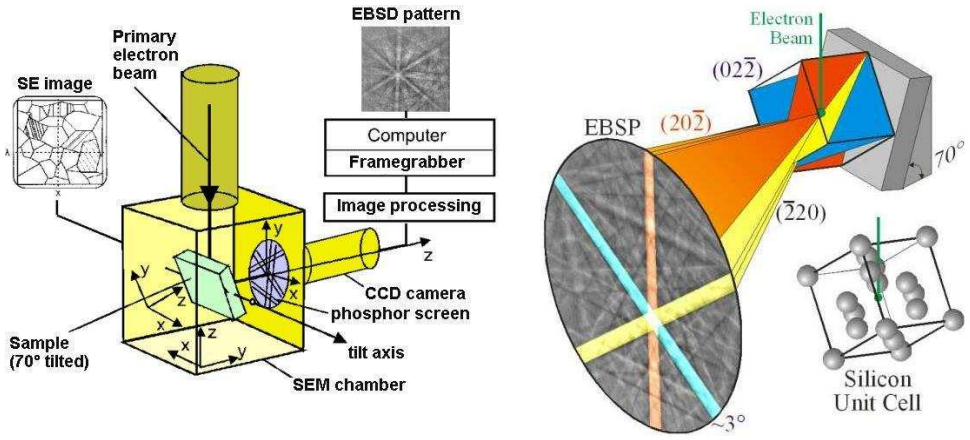

Figure 9.3: Schematic of a typical EBSD system setup (left) and the formation of diffraction pattern on the acquisition screen (Kikuchi bands).

As soon as the crystalline orientation map is obtained there are many additional methods of analysis, which can be applied to it, to extract different information about the microstructure, i.e. Taylor factor, Schmid factor, misorientation profiles, local misorientation etc. Of particular use for this thesis was a local misorientation analysis.

In this thesis work the Jeol 440 SEM was used with the Nordlys II CCD camera attached for EBSD patterns acquisition. Working distance between the sample and the screen was 20 mm, electron beam accelerating voltage of 25 kV, and the angle between the electron beam and sample normal direction was 70°. Square grid was used for EBSD map acquisitions with steps ranging from 0.1 to 20 μm depending on the kind of information needed.

The depth from where the information is obtained with EBSD was estimated to be about 50-100 nm for niobium, thus covering the London penetration depth, which is the depth scale of interest.

9.2.1 Local misorientation

Local misorientation (LM) is defined as an average of misorientation angles between the pixel and its neighbors in a 2D crystalline orientation map:

$$\Delta\alpha = \sum_{i=1}^{N} \Delta\alpha_i$$

where $\Delta\alpha_i$ is the misorientation angle between the pixel and its ith neighbor, N - total number of neighbors counted in the LM determination. In this thesis N=8 was used, so that only adjacent pixels were included in the analysis.

Local misorientation is a measure of a local lattice curvature, which in turn corresponds to a level of plastic deformation, which is accommodated by Geometrically Necessary Dislocations (GNDs) as discussed previously. Thus local misorientation is a measure of a sample dislocation content. This qualitative relation was studied in more detail in [44](pp.247-264).

An example of the crystal orientation map obtained by EBSD on the fine grain BCP niobium sample with the step of 0.5 μm is shown in Fig. 9.4.

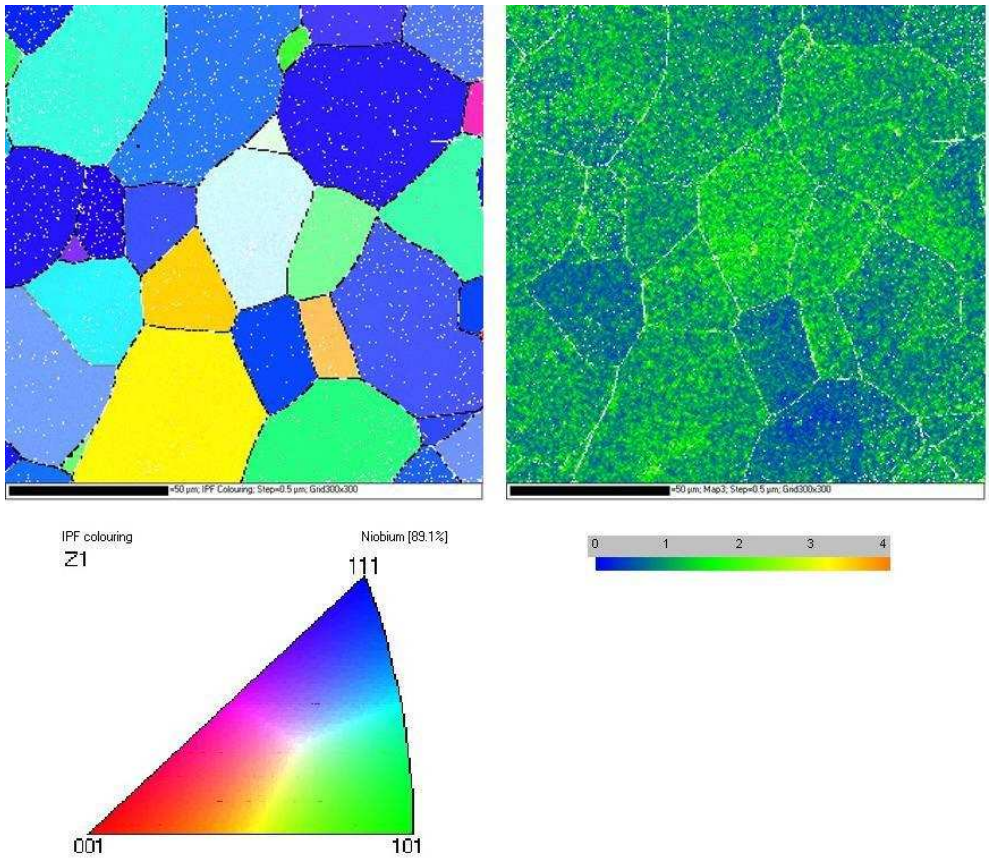

Figure 9.4: Example of an EBSD crystal orientation map (left) and a local misorientation map obtained from it (right) for the fine grain BCP niobium sample. Covered area is 150x150 μm. Color legend for orientations is shown on the left and the misorientation color coding (in degrees) on the right.

The upper left panel shows the crystalline orientation map at each pixel of the map depicted by a particular color. Correspondence between colors and orientations is shown in the lower left inverse pole figure, where color basically codes the angle of misorientation between the spot and three standard orientations: $\langle 001 \rangle$, $\langle 011 \rangle$, and $\langle 111 \rangle$.

The upper right map shows the local misorientation at each pixel calculated as outlined above. Color representation is used, with the legend shown below

the map, so that, for example, zero local misorientations correspond to a dark blue color, and misorientations of about 2° are shown by a green color.

9.2.2 Geometrically necessary dislocation content

Recent development of EBSD data analysis techniques allows obtaining the dislocation tensor from crystalline orientation data.

Local dislocation density tensor, which was introduced by Nye [33], describes the dislocation content concisely:

$$\alpha_{ij} = \sum_{i=1}^{K} \rho^i (b^i \otimes z^i) \tag{9.1}$$

where $\vec{z}^i$ indicates the dislocation direction, $\vec{b}^t$ is a Burgers vector, and ρ^i is a density of dislocations of type i. Assuming zero elastic strain, any crystal containing non-zero dislocation density should have local lattice rotations, which can be measured by EBSD. The relation between the Nye dislocation tensor and lattice disorientations between neighboring points then can be approximated as follows:

$$\alpha_{ij} = e_{ikl} g_{jl,k} \tag{9.2}$$

which is known from EBSD data of orientations g_{ij} at each spot. Eq. (9.1) can be reduced [36] to:

$$\alpha_i = A_{ik} \rho_k$$

where matrix A represents a component of dislocation dyadic $\vec{b} \otimes \vec{z}$. Applying L^2 minimization method the solution can be written explicitly for dislocation density tensor [36]:

$$\rho_{GND} = A^T (A A^T)^{-1} \alpha$$

MatLAB software based on this method developed by R. Fertig [20] was used in order to extract average dislocation density from EBSD orientation maps in this thesis.

9.2.3 Equivalence of LM and GND density characterizations

Local misorientation as measured by the procedure outlined above is a measure of the local lattice curvature, which is directly connected to the dislocation density tensor. So it is important to check this connection explicitly by calculating both local misorientation distributions and GND density distributions for same samples. We chose hot and cold samples from the LE1-37 large grain cavity for this analysis.

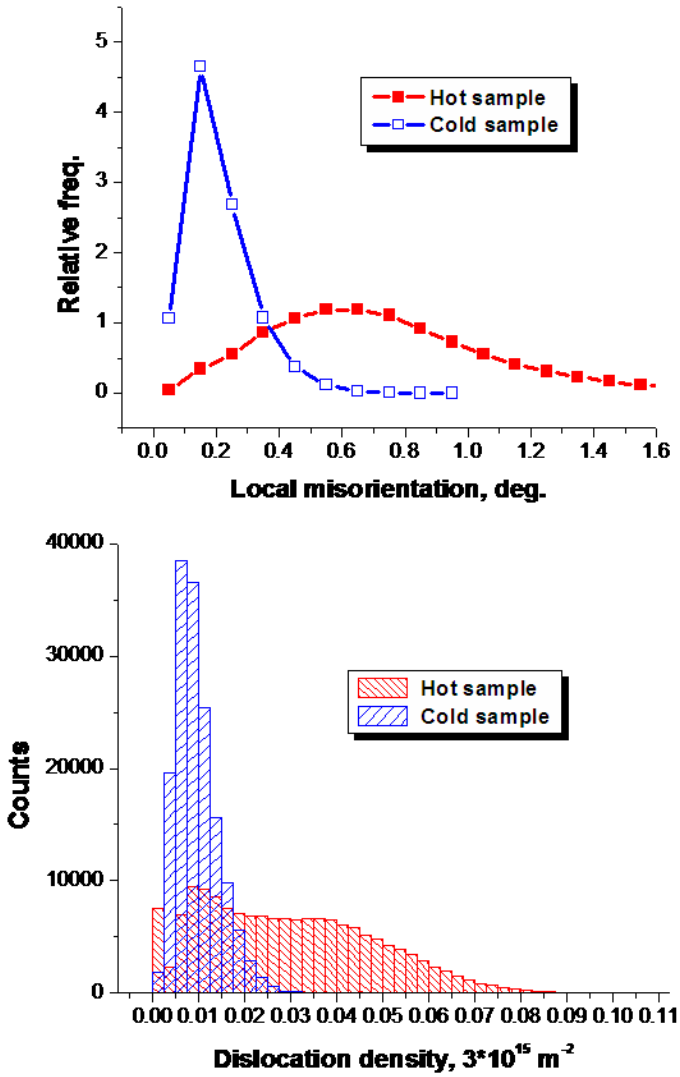

Figure 9.5: Local misorientation distributions for hot and cold samples of LE1-37 large grain BCP cavity (top graph). Compare with the dislocation density distribution (bottom graph) for the same samples.

In Fig. 9.5 local misorientation distributions are shown on the top panel and GND density distributions for the same samples on the bottom panel. One can deduce the strong correlation between the two characterization methods from the data, which is expected from theoretical considerations. Since LM distri-

butions are easier to obtain and contain essentially the same information, they are going to be used for dislocation content comparisons between the samples throughout the thesis.

9.3 Crystalline orientation role in HFQS heating patterns

One of the possible explanations for the heating patterns in the HFQS regime suggested recently was based on the assumption that some grain orientations have lower critical field and/or higher surface resistance than others. Small grain BCP cavity (LE1-35) samples were studied with EBSD in order to check this hypothesis. Texture analysis was performed by getting EBSD maps of samples with a relatively large step of 10-20 μm and then analyzing orientation maps using orientation distribution functions (ODFs) and inverse pole figures (IPFs).

In Fig. 9.6 inverse polar figures obtained by merging all the data obtained for hot (left panel) and cold (right panel) samples are shown. Poles represent three basic crystalline orientations - $\langle 001 \rangle$, $\langle 101 \rangle$ and $\langle 111 \rangle$. Distance from pixel to the pole corresponds to the magnitude of the misorientation angle between the basic orientation of the pole and the pixel.

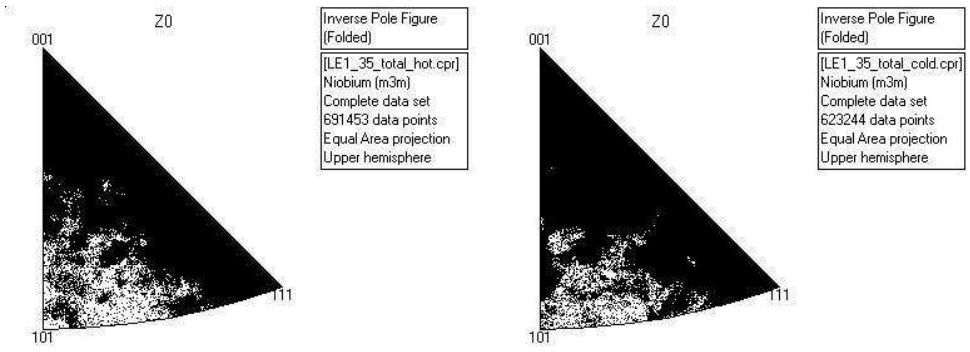

Figure 9.6: Inverse pole figures showing random spread in grain orientations for hot (left panel) and cold (right panel) spots in LE1-35 small grain BCP cavity. Data for all measured samples is included. Notice lack of $\langle 101 \rangle$ orientations in both cases.

It is apparent that there is no preferential orientation in either case. Lack of $\langle 101 \rangle$ orientations can be noticed in both hot and cold samples, which is probably due to sheet rolling and cells forming history. All other orientations are randomly distributed.

Although even single grain cavities show non-uniform losses as determined by thermometry, which already undermines the hypothesis of a crystalline orientation as a main underlying factor for the effect, we provide further direct experimental proof that the hypothesis does not hold and preferential grain orientations are not responsible for the heating non-uniformity in the HFQS.

9.4 Difference between hot and cold samples

As an introductory remark we want to emphasize an important point from the chapters above on the relative intensity of hot and cold regions in cavities of different grain sizes. The largest difference between hot and cold spots was

observed in the large grain BCP case ($\Delta T_{hot}/\Delta T_{cold} \approx 15-25$), followed by a significantly smaller split in small grain EP and BCP ($\Delta T_{hot}/\Delta T_{cold} \approx 2-12$). We would expect EBSD studies to show the similar behavior of the LM distributions, if these bear any relevance to the HFQS.

Large grain BCP cavity samples subjected to EBSD analysis were essentially single grain samples, since the grain size of the LE1-37 cavity was larger than 10 cm, whereas each sample covers only about 3-4 cm^2 area. Analysis was based on the local misorientation distributions obtained with a 1 μm step size.

One of the hot and one of the cold samples, which we analyzed, are of particular interest since they represent an extreme difference between the regions. In Fig. 9.7 local misorientation maps for the **H6** hot sample (left) and **C11** cold sample (right) are shown, which reveal a drastically different microstructure. Sample **H6** appears to have a strong plastic deformation, whereas the cold sample **C11** appears almost free of any stress. Dislocation density is significantly lower in the cold sample as compared to the hot one. And the temperature increase over the bath temperature for the hot sample was about 1K as compared to the 40 mK for the cold one at the highest field.

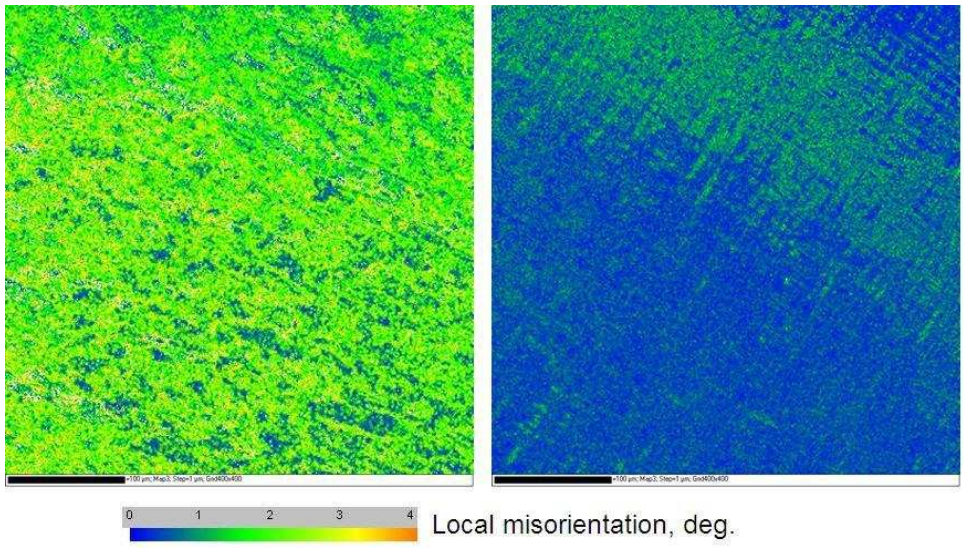

Figure 9.7: Local misorientation maps for **H6** hot spot (left) and **C11** cold spot (right) of a LE1-37 large grain BCP cavity. Map dimensions in both cases are 400x400 μm. Notice a drastically different microstructure.

The corresponding local misorientation and dislocation density distributions were shown previously in Fig. 9.5.

In Fig. 9.8 local misorientation distributions averaged over all hot and all cold spots for the large grain BCP cavity are shown. One can notice that the average distribution is shifted towards lower angles for cold spots as compared to hot spots, which means that on average the GND density is lower in cold spots.

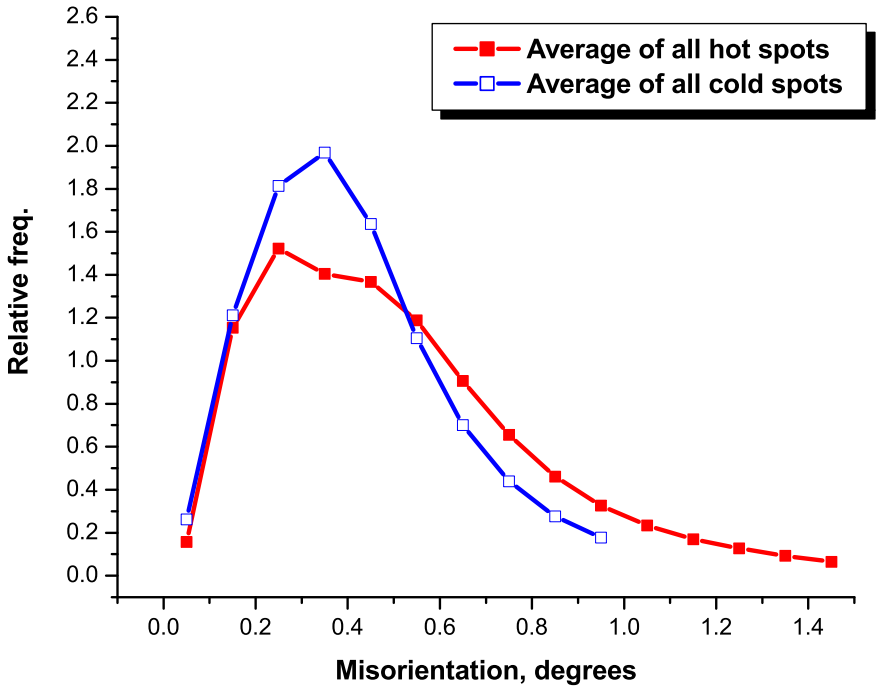

Figure 9.8: Local misorientation distributions averaged over all hot and cold spots for LE1-37 large grain BCP cavity.

Small grain BCP cavity samples, which were analyzed with the EBSD step size of 2 μm, exhibited no observable difference between the hot and cold regions. Resulting LM distributions obtained from crystalline orientation maps are shown in Fig. 9.9. As previously mentioned, the difference in the amount of heating between hot and cold areas in the small grain BCP case is several times smaller than in the large grain BCP cavity as described in Chapter 6, so it may be that it is the reason for the absence of the observable dislocation content difference.

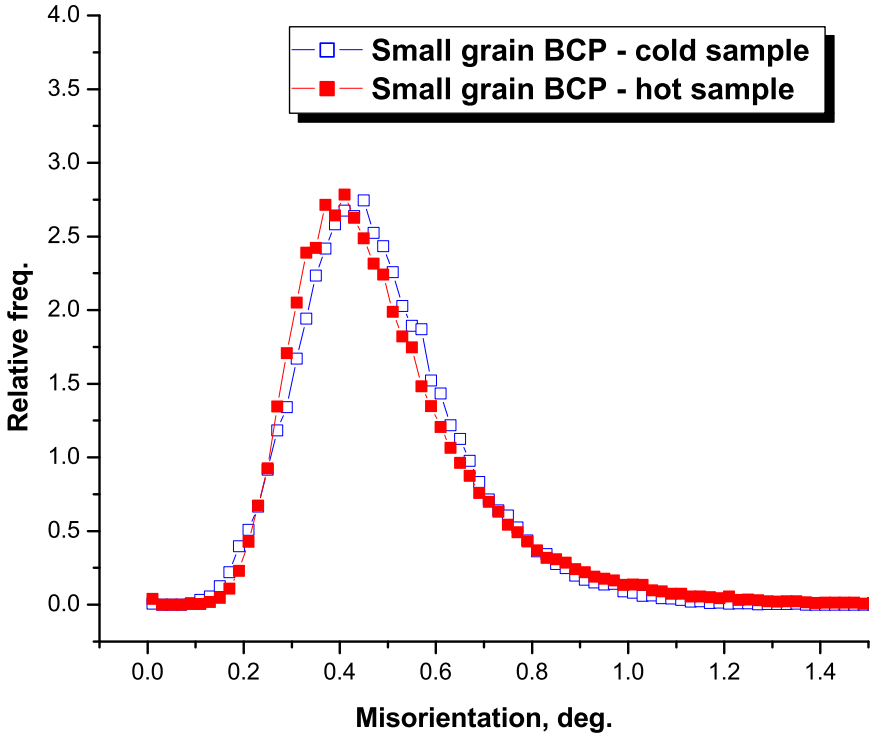

Figure 9.9: Local misorientation distributions for hot and cold spots for LE1-35 small grain BCP cavity.

Small grain EP samples from LE1-HOR hot and cold spots were analyzed with the EBSD step size of 2 μm. LM distributions averaged over the whole set of samples are shown in Fig. 9.10. Again a small shift towards lower misorientation angles is noticeable in cold samples as compared to hot samples.

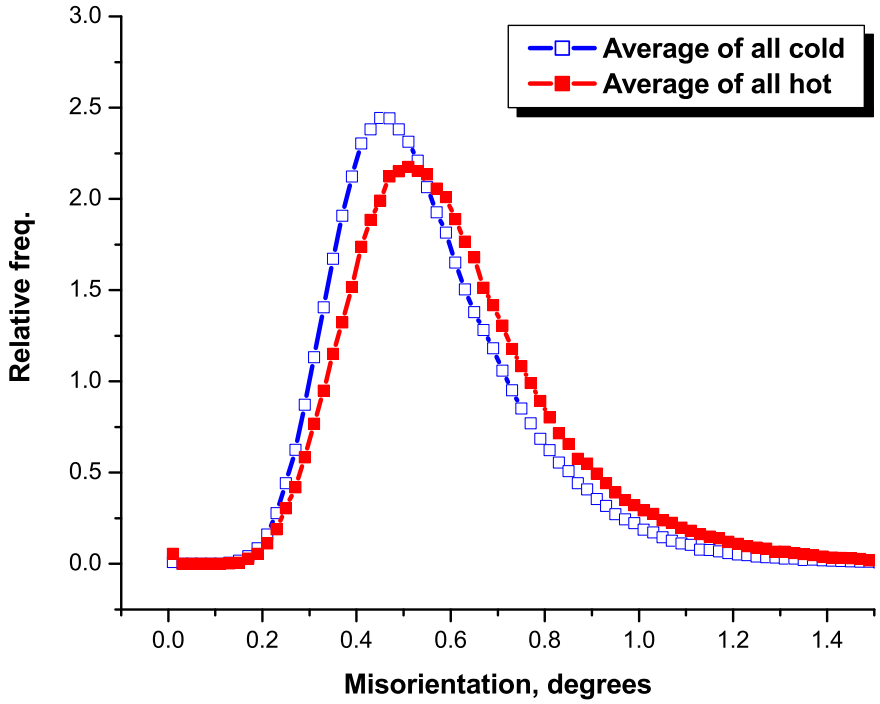

Figure 9.10: Local misorientation distributions averaged over all hot and cold spots for LE1-HOR small grain EP cavity.

A general tendency of cold samples having on average lower GND density than the hot ones can be deduced from the data presented above. Although the shift in the LM towards lower angles in the cold samples as compared to hot is low, it is a real effect since the number of total points measured in each case is of order 10^7, which makes the result statistically significant. Further evidence for the GND density role in the HFQS behavior will be presented in the following section.

9.5 Baking effect on cavity samples

In order to study the effect of baking on dislocation density in hot and cold samples, several samples from all cavities, which had been dissected, were baked at 100-120 °C for at least 48 hours.

In Fig. 9.11 the local misorientation distribution is shown before and after UHV annealing at 110°C for 48 hours for the hot sample from LE1-37 large grain BCP cavity. EBSD orientation maps were obtained with a 2 μm step and LM distributions were calculated from them. Baking resulted in the change of LM distribution manifested in the reduced fraction of higher angle misorientations - effectively the shift of the distribution towards lower angles. From Sec. 9.2.3 we know that it corresponds to the reduced density of GNDs in the baked sample.

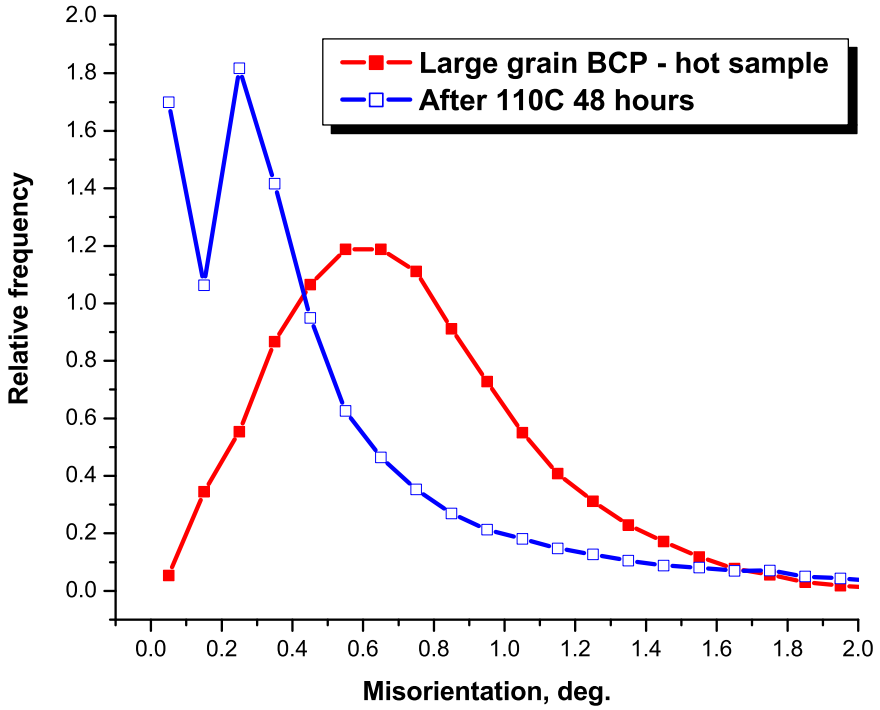

Figure 9.11: Local misorientation distributions for **H6** hot spot of a LE1-37 large grain BCP cavity before and after baking at 110°C for 48 hours.

A similar effect has been observed as a result of baking of the **H1** hot spot and a **C3** cold spot from the LE1-HOR small grain EP cavity. An EBSD step size of 2 μms was used again. LM distribution was obtained from orientation maps as outlined above in Sec. 9.2.1. The strong shifts in the LM distribution towards lower angles for both hot and cold samples is apparent from Fig. 9.12-9.13.

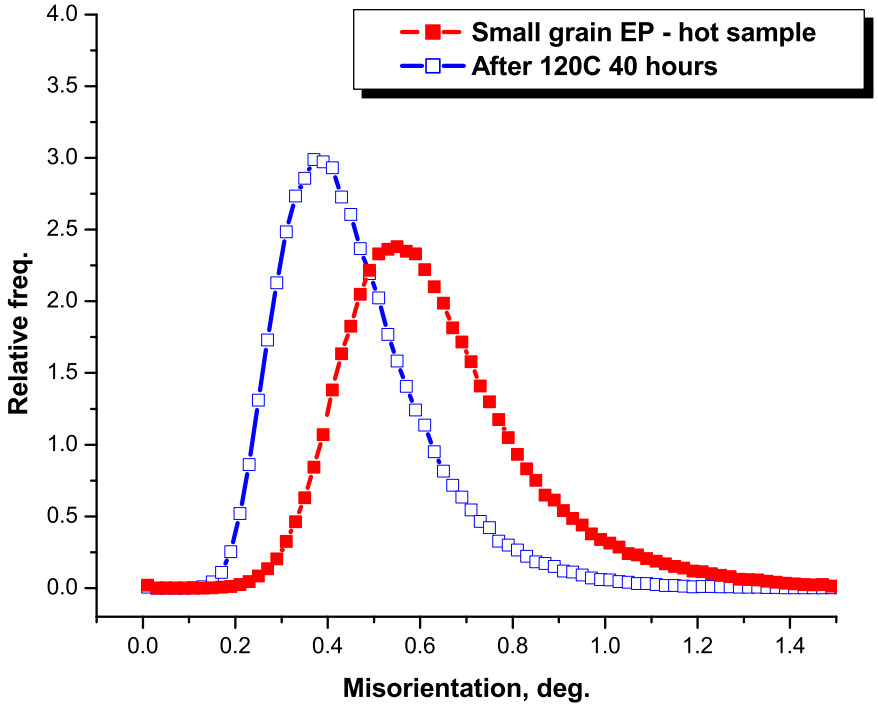

Figure 9.12: Local misorientation distributions for the **H1** hot spot of a LE1-HOR small grain EP cavity before and after baking at 120°C for 40 hours.

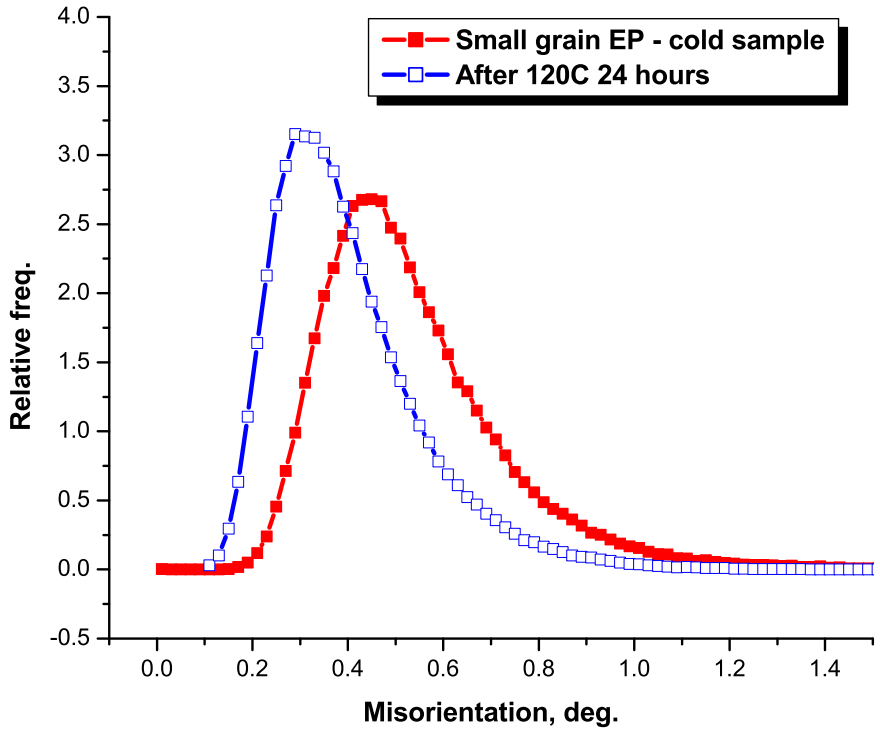

Figure 9.13: Local misorientation distributions for the **C3** cold spot of a LE1-HOR small grain EP cavity before and after baking at 120°C for 24 hours.

EBSD maps with a 2 μm step were obtained on the LE1-35 small grain BCP cavity hot sample (H4) before and after annealing at 120°C for 63 hours. LM distribution was obtained from orientation maps as outlined above in Sec. 9.2.1. As opposed to large grain BCP and small grain EP samples, we observed almost absence of any shift due to baking in the LM as shown in Fig. 9.14.

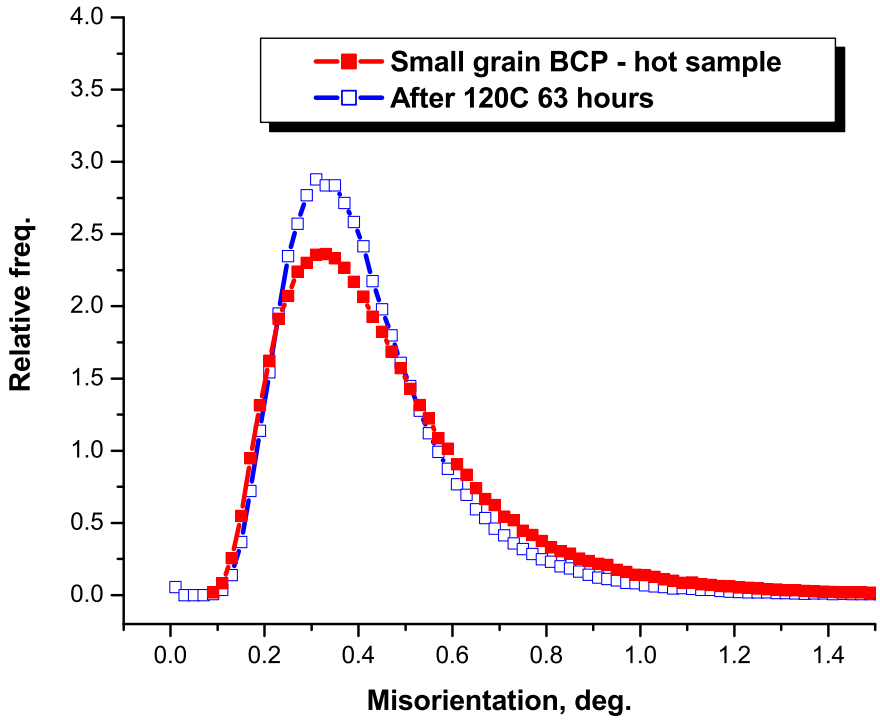

Figure 9.14: Local misorientation distributions for the **H4** hot spot of a LE1-35 small grain BCP cavity before and after baking at 120°C for 63 hours.

As we know from cavity test results, large grain BCP and any grain size EP cavities always respond to a 100-120°C vacuum annealing. The effective result is the elimination of the HFQS in baked cavities. From EBSD data presented above we can conclude that baking on the large grain BCP and a small grain EP material results in the decrease of GND density as revealed by the strong shifts in LM distributions towards lower misorientation angles. This effect allows us to hypothesize the correlation between the GND density and a HFQS presence. The the author's knowledge this correlation is an original discovery.

On the other hand, small grain BCP cavities usually show much less re-

sponse to the mild baking than do large grain and EP-treated cavities. And our EBSD studies on the small grain BCP hot spots showed that in fact the effect of baking is almost not present. This is a compelling correlation, which adds strength to our hypothesis, which is going to be considered in more detail in the following chapter.

CHAPTER 10

POSSIBLE MECHANISMS FOR THE HFQS AND THE MILD BAKING EFFECT

10.1 Introduction

In this chapter we propose a model for the HFQS than also explains the following effects due to baking:

1. Baking has a large effect on EP cavities
2. Baking has a large effect on large grain cavities
3. The depth of baking benefit is 10-20 nm

EBSD studies of the samples from three different cavities considered in Chapter 9 allow us to propose a possible model for the observed HFQS heating patterns and the 100-120°C annealing effect.

We suggest that the underlying cause of the observed heating non-uniformity might be the difference in plastic deformation – hot areas have a larger Geometrically Necessary Dislocation (GND) density than the cold ones. Higher GND density results in a locally suppressed Bean-Livingston barrier due to vortex attraction to dislocations (pinning force) as shown, for example, in [30, 5].

A possible explanation for the baking effect based on the dislocation climb process is proposed.

10.2 Bean-Livingston surface barrier

Bean and Livingston [4] have theoretically deduced that on the surface of type II superconductors there exists a potential barrier for the penetration of fluxoids. They considered the forces acting on a fluxoid close to the surface of the type II superconductor. Since the currents at the surface should have no perpendicular component, this boundary condition results in the existence of an "image" force acting on the fluxoid, which attracts it to the surface in full analogy to the force of an image charge in electrostatics. Another force acting upon the fluxoid is the force exerted by the external magnetic field, which pushes the fluxoid inside the superconductor. The image force and the magnetic force have different dependencies on the distance from the surface and thus the surface barrier in the fluxoid energy emerges. Bean and Livingston were able to calculate the surface barrier for different magnitudes of the applied magnetic field as shown in Fig. 10.1.

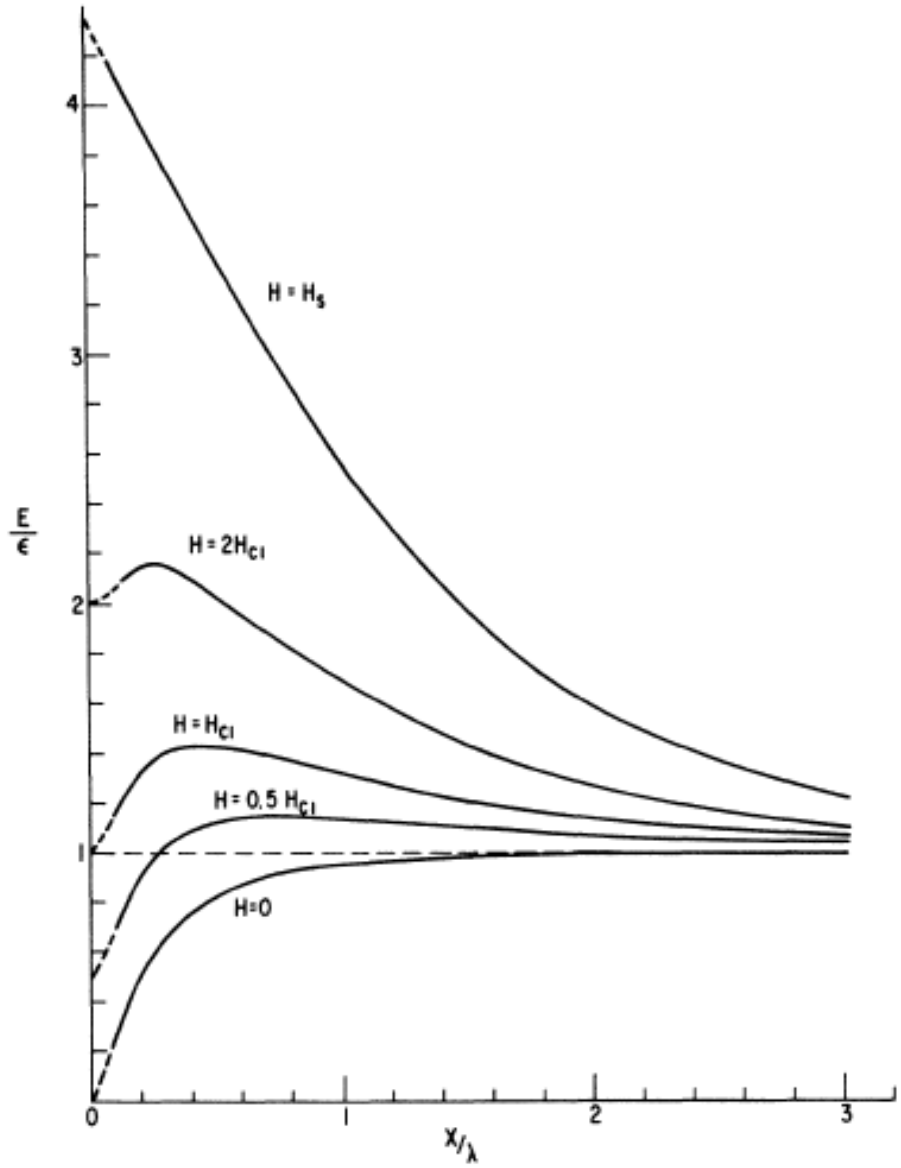

Figure 10.1: Dependence of the fluxoid line energy on distance from the surface for different applied magnetic fields (reproduced from [4]).

An existence of the surface barrier was subsequently experimentally demonstrated. It was also found that the dislocation density has a dramatic effect on the surface barrier. Hysteretic behavior in magnetization is determined by a surface barrier and its change with the dislocation content is shown in Fig. 10.2,

which is reproduced from [29].

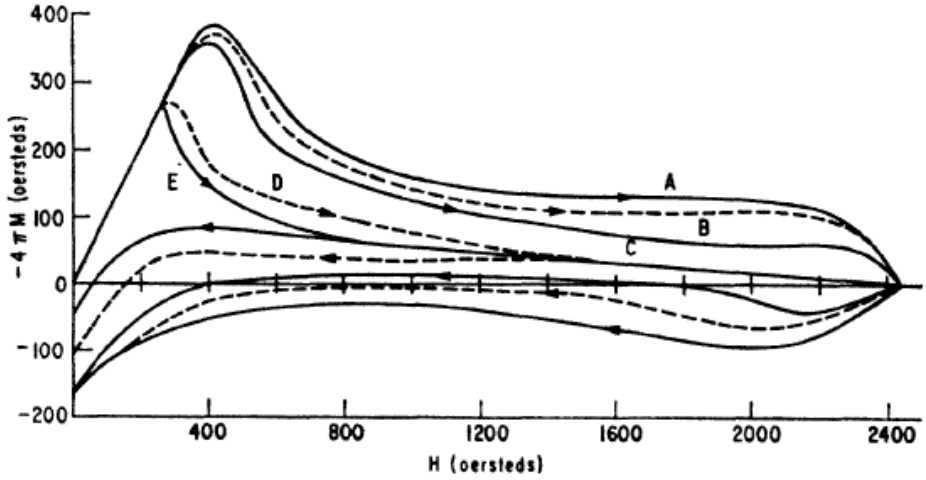

Figure 10.2: Effect of the subsequent room temperature annealing on the lead-8.23 wt.% indium alloy. A–as-cold swaged, B–annealed 30 min, C–1 day, D–18 days, E–46 days (reproduced from [29]).

10.3 Dislocation-based model for the HFQS

There are many sources for producing dislocations in niobium for cavities. The starting sheet material has dislocations due to rolling. Annealing for recrystallization removes most, but possibly not all dislocations. Mechanical deformation performed on niobium in order to form the elliptical cavity shape (i.e. half-cell deep drawing or spinning) results in the high dislocation density introduced inside the material in order to accommodate a plastic deformation. Since applied stress is not uniform a surface deformation is higher than the bulk.

Subsequent chemical etching (i.e. BCP or EP) results in the removal of the surface layer of a very high dislocation content ("damage" layer). On the other

hand, the dislocation structure left by chemical treatments in the surface layer of niobium might be different from that in the bulk.

A high dislocation density lowers the energy of a single vortex inside niobium due to the attractive interaction between a vortex and a dislocation (pinning force), effectively reducing the Bean-Livingston surface barrier height. Thus vortex penetration happens at lower RF fields in areas with the higher dislocation density, manifesting itself in the higher dissipation due to the presence of the vortex core in the RF layer and due to the dissipative oscillatory motion of vortices under the driving Lorentz force.

Variations of the dislocation density over the high-magnetic-field region of cavity walls can produce the observed heating non-uniformity in the HFQS regime as found by temperature mapping - see Fig. 6.4. Dislocation density after baking is reduced in hot areas to the value below the density in the cold spots before baking. Before baking both hot and cold areas have dislocation densities high enough for the HFQS to appear everywhere but with the different strength (hot and cold ares), as found by cavity tests with thermometry. After baking, the dislocation density is reduced, so flux entry and losses become low.

The presence of fluxoids inside niobium within the RF magnetic field penetration depth causes dissipation, which consists of two components:

- Inductive losses due to the stationary fluxoid normal conducting core originating from the superconducting current time variation
- Losses due to the fluxoid motion arising from the viscous drag

The dissipation mechanism due to vortex moving in and out of niobium

driven by a strong RF field have been recently theoretically studied by Gurevich and Ciovati in [26]. The losses due to viscous flux motion accompanied by a flux pinning rise sharply for RF field amplitudes higher than the first flux-entry field B_v, which depends on the particular defect serving as a "gate" for the flux entry. In another theoretical study a dissipation due to a single oscillating vortex, which is already in the surface layer of a superconductor, was considered by Rabinowitz in [39, 38].

The difference between models in [26] and [39, 38] is that the former model does not take into account the effective mass of the fluxoid, whereas the latter one neglects the image force acting on the fluxoid due to the presence of the surface.

The experimental measurements of the velocity of the magnetic field penetration in niobium reported in [21] give at 4.2 K the value of $v_p = 3100 - 4700\, cm/s$. Contrary to the common belief within the SRF community, this speed does *not* translate into the fluxoid nucleation time much larger than the RF period for all fluxoids. The nucleation times for the fluxoids parallel and perpendicular to the cavity surface are significantly different due to the distance the magnetic field should travel in each case. For the case of a $d = 3\ mm$ cavity wall thickness the nucleation time for the fluxoid perpendicular to the surface is $\tau_\perp = d/v_p \approx 10^{-6}\ sec$, but for the fluxoid parallel to the surface the magnetic field only has to travel about the coherence length $\xi = 40\ nm$, and that gives $\tau_\parallel = \xi/v_p \approx 10^{-9}\ sec$, which is of the same order of magnitude as the RF period for 1.5 GHz cavities.

We will follow the simplified model of Rabinowitz to estimate the fluxoid-related losses in the case of niobium cavities, reproduced here for understanding

the losses. The schematic of the problem in hand is shown in Fig. 10.3.

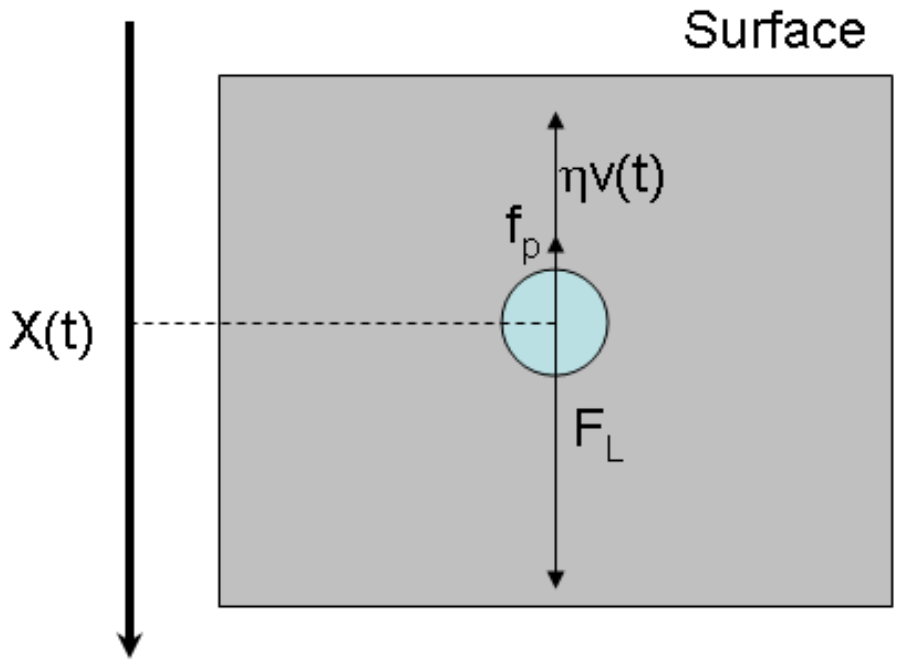

Figure 10.3: Schematic of the single fluxoid within the London penetration depth of the niobium surface with the forces acting on it in the Rabinowitz's model [39, 38].

Following Rabinowitz we first estimate the inductive losses due to the stationary normal conducting core. The electric field induced in a superconductor by the variable current is:

$$E = \frac{m}{e}\left[\frac{1}{ne}\frac{dj}{dt}\right] = \frac{im\omega}{ne^2}j = \rho_s j \tag{10.1}$$

where ρ_s is the superconducting electrical resistivity. Under the assumption that the induced electric field is approximately uniform throughout the fluxoid core, the average dissipated power per unit volume in the normal conducting core is:

$$\frac{dP}{dV} = \frac{1}{2\rho_n'}E^2 \tag{10.2}$$

where ρ_n' is the effective resistivity of the stationary normal region if the actual current flowing through it is used.

$$\rho_n' = G\rho_n, G \geq 1 \tag{10.3}$$

The value of G depends on the relative magnitudes of the electron mean free path and the radius of the fluxoid and for niobium it is close to G=1. Using Eq. (10.1) together with Eq. (10.2) we obtain:

$$\frac{dP}{dV} = \frac{1}{2}\left(\frac{\rho_s^2}{\rho_n'}\right) j_0^2 = \frac{1}{2}\rho_{stat} j_0^2 \tag{10.4}$$

where

$$\rho_{stat} = \frac{\rho_s^2}{\rho_n'} = \frac{m^2\omega^2}{n^2 e^4 G}\frac{1}{\rho_n} \tag{10.5}$$

is the effective resistivity of the normal region if the supercurrent is to flow through it. For niobium cavities at 1.5 GHz we obtain $\rho_{stat} \approx 3.6 \times 10^{-14}\Omega \cdot m$ and the effective surface resistance of $R_{stat} = \frac{\rho_{stat}}{2\pi\lambda} \approx 0.14\mu\Omega$ for a single normal core.

If the fluxoid is not stationary but moving inside the superconductor, an additional dissipation arises. The mechanism of this additional dissipation can be simply explained by the additional electric field induced by the moving magnetic flux. This induced electric field acts on the normal electrons within the fluxoid core causing the dissipation.

Now, let's consider the forces acting on the fluxoid inside a superconductor. As mentioned above, the image force is neglected in this model and there are three forces, which act on the fluxoid - a driving Lorentz force $F_L = Re[\phi_0 j_0 exp(i\omega t)]$, a viscous drag force $\eta v(t)$, and a pinning force $f_p = -pX(t)$. Thus the equation of motion for the fluxoid has the form:

$$MX''(t) + \eta X'(t) + pX(t) = Re[\phi_0 j_0 exp(i\omega t)] \tag{10.6}$$

The solution of Eq. (10.6) is

$$X(t) = Re\{X_0 exp[i(\omega t + \delta)]\} \tag{10.7}$$

For the fluxoid, which is not stationary but oscillating under the influence of the Lorentz force, the power dissipation per unit volume is determined by the work of the Lorentz force averaged over time:

$$\frac{dP}{dV} = \frac{1}{2} Re \left[\mathbf{j} \times \mu \mathbf{H} \cdot \left(\frac{d\mathbf{X}}{dt} \right) \right] = \frac{1}{2} \rho_{eff} j_0^2 \tag{10.8}$$

where j_0 is the superconducting current density at the surface of the superconductor and ρ_{eff} is the effective resistivity of the oscillating fluxoid. Using Eq. (10.7) we obtain the effective resistivity for the case of the fluxoid parallel to the surface to be:

$$\rho_{eff} = \frac{\omega^2 \phi^2 H H_0 \mu^2}{\rho_n^2 (\omega^2 M - p) + \omega^2 \phi^2 H_0^2 \mu^2} \rho_n \tag{10.9}$$

where ϕ is a total magnetic flux in the fluxoid, M is the effective mass of the fluxoid per unit length, p is the pinning force per unit length of the fluxoid, ρ_n is a normal state resistivity, H is the magnetic field in the fluxoid, and $H_0 = H_{c2}$ - upper critical field.

The effective mass of the fluxoid M is given by the Bardeen-Stephen formula [3]:

$$M = 2\pi n m a^2 \left(\frac{H_0}{H} \right)^2 sin^2 \alpha \tag{10.10}$$

where n is the electron density, m is the electron mass, a is the radius of the fluxoid, and α is a Hall angle.

Substituting Eq. (10.10) into Eq. (10.9) we obtain for the general case:

$$\rho_{eff} = \frac{\omega^2 \phi^2 H H_0 \mu^2}{\rho_n^2 \left(2\pi \omega^2 n m a^2 \left(\frac{H_0}{H} \right)^2 sin^2 \alpha - p \right)^2 + \omega^2 \phi^2 H_0^2 \mu^2} \rho_n \tag{10.11}$$

To estimate the mass per unit length of a single quantum of magnetic flux ϕ_0 we assume that $sin^2\alpha = 1$, $a \approx \xi \approx 40\ nm$, $n = 5.55 \times 10^{28}\ m^{-3}$, $H = H_0 = 400\ mT \approx 3.2 \times 10^5\ \frac{A}{m}$ to obtain:

$$M \approx 5.1 \times 10^{-16}\ kg \tag{10.12}$$

Since the pinning force p per unit length of the fluxoid is not known, we will use the approximation of $p \ll \omega^2 M$ first and will discuss the effect of a non-negligible p later. Using the value of $\rho_n \approx 10^{-9}\ \Omega \cdot m$ for Nb at low temperatures we obtain:

$$\rho_{eff} \approx 2.9 \times 10^{-11} \Omega \cdot m \tag{10.13}$$

and the effective surface resistance is

$$R_{osc} = \frac{\rho_{eff}}{2\pi\lambda} \approx 120\mu\Omega \tag{10.14}$$

The surface resistance due to the stationary normal conducting core is therefore much less than the surface resistance due to the oscillatory motion of the fluxoid. The total surface resistance of the single oscillating fluxoid is thus:

$$R_s^{flux} = R_{stat} + R_{osc} \approx 120\mu\Omega \tag{10.15}$$

First we estimate the needed number of fluxoids N_{flux} to produce losses, which are comparable to the power dissipation due to regular BCS losses for the ideal cavity. We assume that the effective area of each oscillating fluxoid is $\pi\xi^2$ and then we obtain for the power of the fluxoid-related losses:

$$P_{flux} = \frac{1}{2} R_s^{flux} A_{flux} H^2 \tag{10.16}$$

where $A_{flux} = N_{flux}\pi\xi^2$ - total effective area of the oscillating fluxoids. For the regular BCS losses we have:

$$P_{diss} = \frac{1}{2} R_s^{BCS} A_{cav} H^2 \tag{10.17}$$

where A_{cav} is the effective area of the cavity, $A_{cav} \approx 0.156\ m^2$, and $R_s^{BCS} \approx 13.8\ n\Omega$ at $Q_0 = 2 \times 10^{10}$.

If P_{flux} is equal to P_{diss} than the Q_0 of the cavity will decrease by a factor of 2. From Eq. (10.16) and 10.17 we obtain:

$$\frac{1}{2} R_s^{flux} A_{flux} = \frac{1}{2} R_s^{BCS} A_{cav} \Rightarrow \sigma_{flux} = \frac{N_{flux}}{A_{cav}} = \frac{1}{A_{flux}} \frac{R_s^{BCS}}{R_s^{flux}} \approx 1.7 \times 10^{10}\ m^{-2}$$

where σ_{flux} is the area density of fluxoids required to decrease the Q_0 by a factor of 2. This density of fluxoids corresponds to the average spacing between the fluxoids to be:

$$l \approx \frac{1}{\sqrt{\sigma_{flux}}} = 8\ \mu m$$

If we compare the fluxoid density with the value obtained from the dislocation density tensor calculations based on EBSD data for the **H6** sample from a large grain LE1-37 cavity (Fig. 9.5), the estimate for σ_{flux} is about three orders of magnitude lower than the estimated dislocation density. There are two possible explanations for the difference.

First one is that if we assume that there is only some fraction of dislocations, which have types and/or orientations with respect to the applied magnetic field, favorable for the earlier flux entry in the form of single oscillating fluxoids at each dislocation center, then the difference might come from the fact that not all dislocations will serve as flux entry sites initially, but as the applied magnetic field increases, more and more fluxoids penetrate, increasing the losses until the quench is reached at some location.

Another explanation comes from the finding that dislocations in a cavity-grade niobium are distributed non-uniformly and form a dislocation cell structure. In this structure the dislocation density is much higher in the dislocation

cell walls, and is decreased inside the dislocation cell. In the experimental study on niobium wires [43] it was experimentally shown that dislocation cell walls strongly interact with fluxoids. TEM micrographs of the dislocation cell structure observed on the filaments is shown in Fig. 10.4.

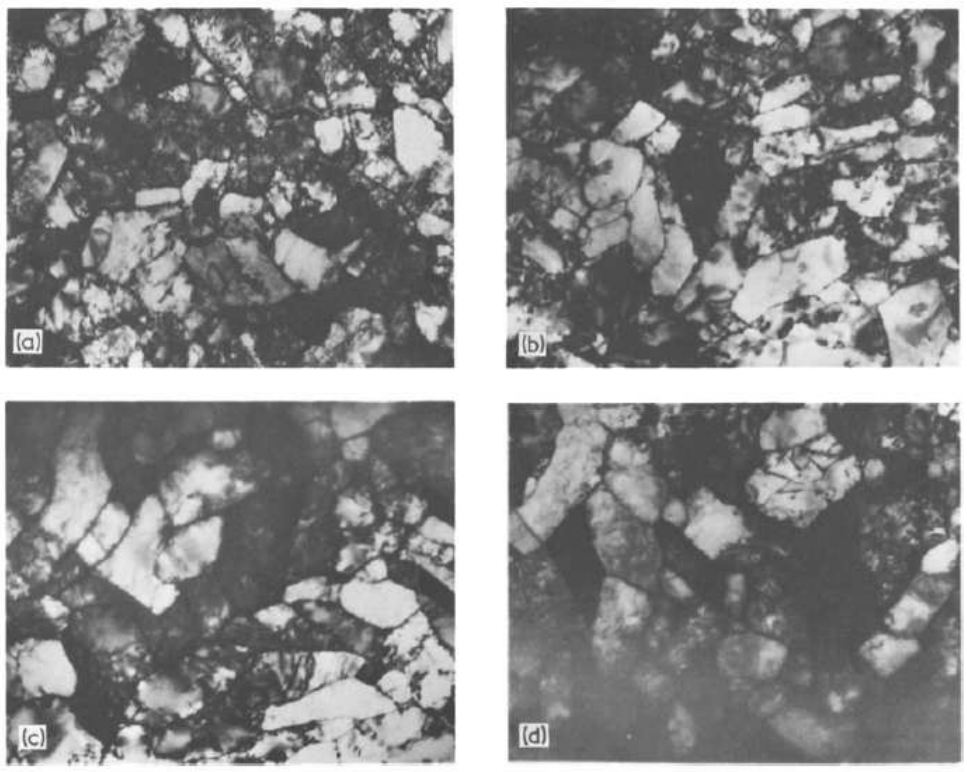

Figure 10.4: TEM micrographs of the dislocation cell structure in niobium wires (reproduced from [43]).

In application to the RF case, dislocation cell walls might also serve as the flux penetration sites, and not individual dislocations. Then we have a good order of magnitude agreement between the density of fluxoids and the dislocation cell walls density, since the dislocation cell size is expected to be of order a few microns.

Returning to the effect of the non-zero pinning constant p on the resistivity

of the fluxoid, we can consider it based on the Eq. (10.11). The pinning constant is in the denominator of the Eq. (10.11), and if it is not negligible, but less than $\omega^2 M$ term, it will decrease the denominator, increasing the effective resistivity of the fluxoid. A physical picture that might make it more clear is that the non-zero pinning force allows the fluxoid to spend more time in the higher current density region closer to the surface of a superconductor thus increasing the effective resistivity.

10.4 Baking effect due to dislocation climb

In order to explain the low-temperature baking effect on the HFQS we suggest a dislocation climb mechanism enabled by vacancy motion at elevated temperatures.

Dislocation climb is the motion of a dislocation in the direction perpendicular to its glide plane. Both edge and screw dislocations can climb, although details of the process are different. The dislocation climb can only occur if accompanied by a movement of vacancies. A typical example is when the monoatomic vacancy comes next to an edge dislocation. An atom from the dislocation extra half-plane can jump in the place of the vacancy and as a result the dislocation will move by a one lattice vector.

A rough schematic of the process is shown in Fig. 10.5. When the vacancy diffuses to the position of the atom, the dislocation effectively moves by a one lattice vector.

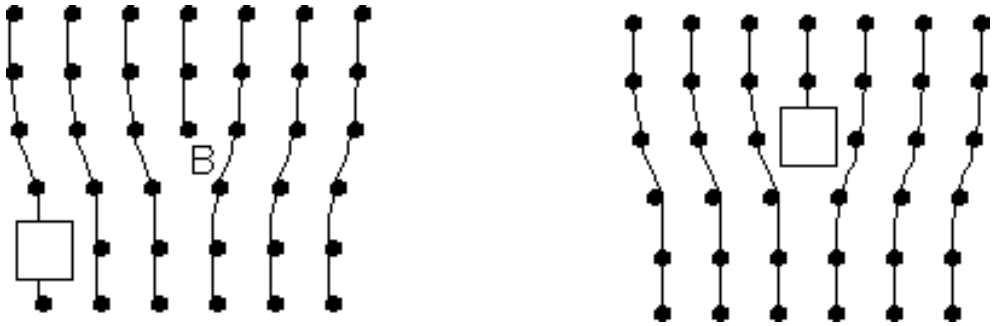

Figure 10.5: Schematic of the edge dislocation climb through vacancy diffusion.

The dislocation climb process has a strong temperature dependence as opposed to another form of dislocation movement – slip. Since cavity experiments suggest that the HFQS has a strong response to the temperature of baking, it points toward dislocation climb as a possible mechanism for the baking effect. The temperature dependence of the dislocation climb comes from the strong link between the climb and vacancies, which have a strongly temperature dependent diffusion coefficient:

$$D = D_0 e^{-\frac{E_a}{k_b T}} \tag{10.18}$$

where E_a is the activation energy. The value of E_a for niobium is not found in the literature, but positron annihilation studies show [13] that at about 100°C vacancies become mobile due to the dissociation of vacancy-hydrogen complexes, which bind vacancies and prevent them from moving. So baking turns on the dislocation climb mechanism by freeing the vacancies. It should be noted that the concentration of vacancies should not necessarily change as a result of baking, since the role of vacancies is to just provide a mechanism for the dislocation motion. Some preliminary positron annihilation studies were performed in order to study the effect of mild baking on the vacancy concentration, these are reported in Appendix A.

The net result of the 100-120°C baking is a decreased number of dislocations in the London penetration depth, which translates into a smaller number of sites for a premature flux entry. Baking may particularly reduce the number of dislocations, which are oriented favorably for the magnetic flux to enter at low field levels.

The fact that small grain cavities require longer baking times as compared to large grain and single grain cavities can also be explained by the effect of grain boundaries on the annealing, grain boundaries being the obstacles in the way of dislocation and vacancy motion during the baking.

Small grain BCP cavities often do not respond to the baking as found by cavity tests, so that the HFQS is not removed. Since surface irregularities (i.e. GBs) have sharper and deeper steps, the total roughness is much higher for the BCP surface. This prevents the motion of dislocations required for the total "healing" effect of baking.

The destructive effect of more than about 20 nm material removal by anodizing [10] or BCP or EP on the baking benefit might come from the fact that only material within the dislocation climb range is modified by baking, since dislocations can climb out of niobium only at the surface and the bulk dislocation density is not affected. Chemical treatment thus just removes the layer, which was modified and restores the bulk dislocation concentration.

To summarize, we suggest that vacancies in niobium, which become mobile starting at about 100°C, enable dislocations to climb out of niobium, which results in the reduced dislocation density in the surface layer. As a result there are fewer flux quanta present in the penetration depth and smaller losses.

CHAPTER 11

SUMMARY

Surface characterization of the hot and cold areas dissected from niobium cavities of different grain size, which had BCP and EP treatment prior to test, allowed to make several conclusions about the role of different surface properties in the HFQS.

A roughness of hot and cold samples was analyzed by optical profilometry and was found to be the same on all relevant scales. Therefore it cannot be responsible for the heating patterns in the HFQS regime, and, perhaps, can be eliminated from the list of primary causes of the HFQS as well.

A niobium oxide structure of hot and cold samples was analyzed using XPS. Results show that the oxide structure is very similar for all samples analyzed, at least at the level of XPS sensitivity (0.1-1 at.%). Hence, differences in the oxide cannot be the underlying cause of the HFQS heating non-uniformity.

Nitrogen was identified as a possible contributor to the heating patchiness in the small grain BCP case, as three hottest samples exhibited a significant nitrogen signal. Still, small grain EP and large grain BCP cavities did not have any excess nitrogen in the hot areas. Thus, a full role of common contaminants (C, N) is not completely clear, but most likely they play a minor role in the HFQS if any.

Grain orientations have been analyzed on the small grain BCP hot and cold samples and it was shown that the texture is random and there is no preferential orientation present.

A difference in the dislocation structure of hot and cold samples found by EBSD was identified as a possible source of the HFQS heating non-uniformity.

A change in the dislocation structure due to mild baking of cavity samples was observed by EBSD.

An alternative explanation for the HFQS was proposed based on the premature flux penetration at dislocations or dislocation cell walls.

A possible mechanism for the mild baking effect based on the dislocation climb enabled by vacancies was proposed.

APPENDIX A

POSITRON ANNIHILATION STUDIES

Vacancy concentration and mobility in niobium might play a role in the low temperature baking effect, since vacancies can provide a mechanism for the dislocation motion through a dislocation climb. In order to study the near-surface concentration of vacancies and its change upon low temperature baking, *Positron Annihilation Spectroscopy* (PAS) was used. PAS is based on the trapping of positrons by the open volumes within the sample material followed by the annihilation with electrons. The energy of the resulting γ-quanta depends on the momentum of the electrons. The momentum of the electron in the annihilation process is dependent upon whether the electron is in the regular lattice or in the vacancy-like defect. As a result, a Doppler-broadening of the spectrum of the produced radiation can be used as a measure of the distribution of electron momenta and thus the vacancy concentration. A detailed description of the technique is beyond this thesis and can be found elsewhere.

Output data from PAS is the dependence of the so-called *S-parameter* on the positron energy. S-parameter characterizes a sharpness of the X-ray spectrum, and qualitatively the higher the S-parameter, the higher the vacancy concentration.

The energy of positrons E_p determines the depth d inside the material they penetrate, and the approximate relation exists:

$$d[nm] = \frac{40}{\rho} E_p^{1.6} \tag{A.1}$$

where ρ is the density in g/cm^3 of the analyzed material.

A collaboration was established with Prof. P. Simpson from University of Western Ontario in order to perform PAS measurements on several niobium samples. Several single grain niobium samples treated with BCP for about 100μm material removal were analyzed with PAS before, during, and after low temperature baking at 30-200 °C. Results of the S-parameter measurements for one of the single grain BCP samples are shown in Fig. A.1.

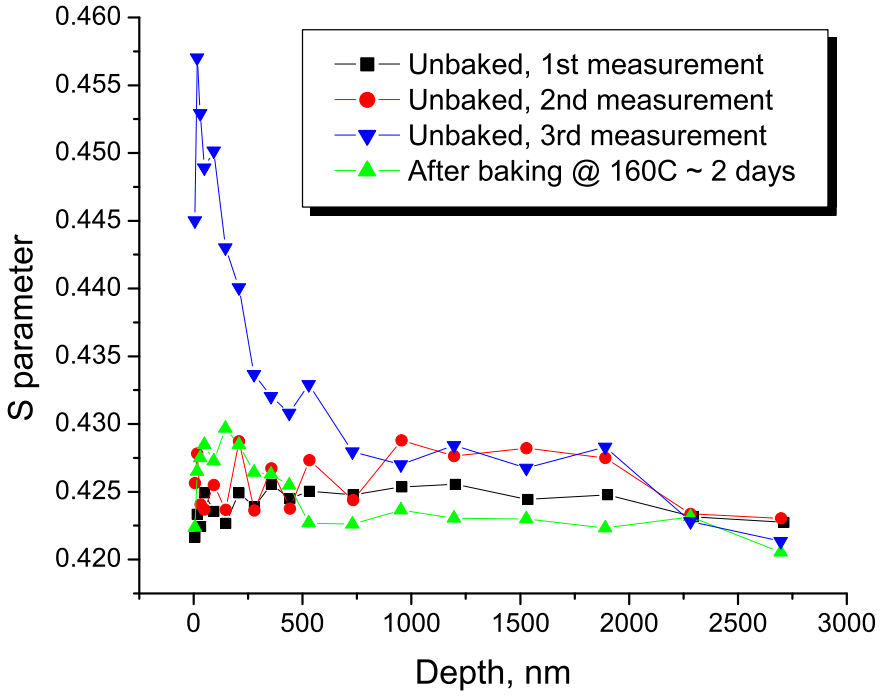

Figure A.1: S-parameter vs. depth for a single grain BCP sample. The peak in S-parameter close to the surface appeared after vacuum failure and was removed by a 160°C in situ baking for 2 days.

After two initial measurements the sample was left in the PAS vacuum chamber for a few days. After that the S-parameter was remeasured and surprisingly a peak in the S-parameter close to the surface appeared. It was found out later that there were intermittent problems with vacuum while the sample

was sitting in the chamber, so that a vacuum failure caused the peak. It is unclear at this point if the peak corresponds to the increased vacancy density in the surface layer or is a consequence of the adsorbed layer of residual gases released during the pump failure (H, CO). Subsequent baking of the sample at 160°C for 2 days and remeasuring the S-parameter showed that the peak was removed.

It was decided to ramp-anneal another sample (with the peak in S-parameter) in vacuum by gradually increasing the temperature from room temperature up to about 200°C keeping the sample at each temperature in the process for about 30 minutes, while investigating the S-parameter at $E_p = 6\ keV$, which corresponds to the depth of about 20 nm in niobium. The results are shown in Fig. A.2.

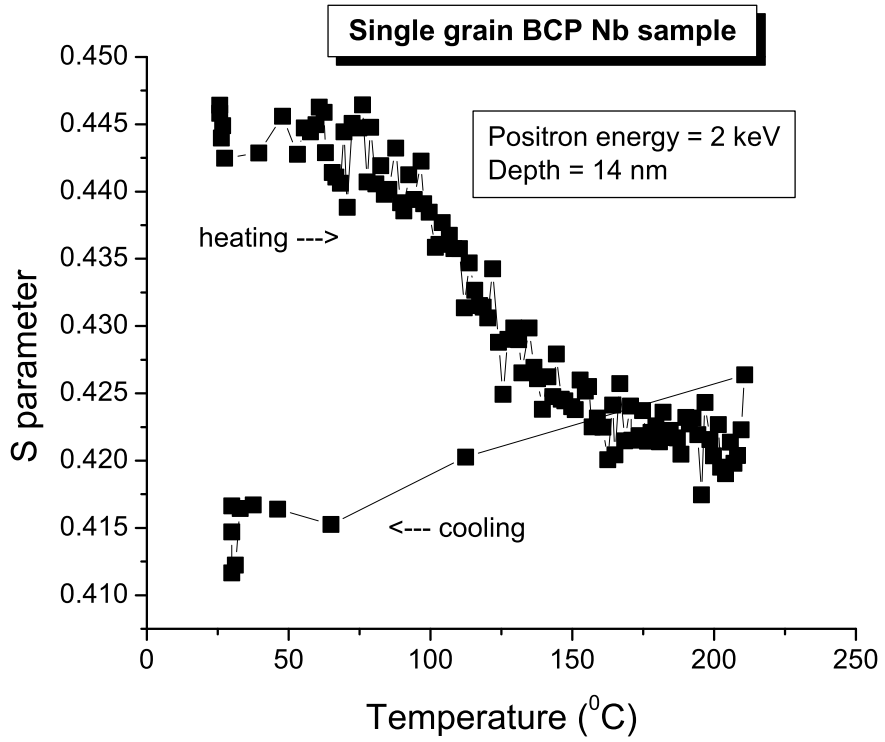

Figure A.2: S-parameter at a fixed positron energy E = 2 keV vs. baking temperature for a single grain BCP sample. Note the onset of the S-parameter decrease at T = 80°C.

After ramp annealing the S-parameter depth profile was remeasured and showed no peak near the surface, indicating a slightly decreased S-parameter than in the bulk. After the air exposure of the sample and remeasuring the S-parameter it was found that the peak did not reappear thus confirming that the annealing change was irreversible (Fig. A.3).

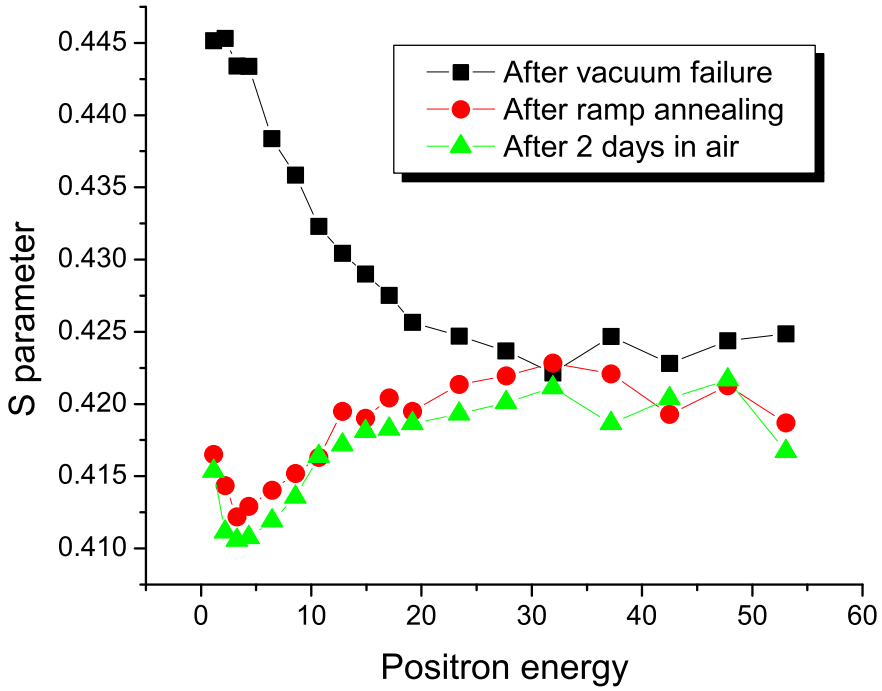

Figure A.3: S-parameter vs. positron energy for a single grain BCP sample. The peak in S-parameter appeared after vacuum failure and was removed by a ramp annealing. Air exposure did not bring the peak back.

In these preliminary studies there were some changes in the sample observed with PAS due to vacuum failure and a subsequent baking at low temperatures used for the cavity mild baking. It is unclear at this point though, what the physical interpretation of the results is.

BIBLIOGRAPHY

[1] C. Y. Ang. *Acta Metall.*, 1:123, 1958.

[2] J. Bardeen, L. N. Cooper, and J. R. Schrieffer. *Phys. Rev.*, 108:1175, 1957.

[3] J. Bardeen and M. J. Stephen. *Phys. Rev.*, 140(A1197), 1965.

[4] C. Bean and J. D. Livingston. *Phys. Rev. Lett.*, 12:86–87, 1964.

[5] A. M. Campbell and J. E. Evetts. Flux vortices and transport currents in type ii superconductors. *Advances in Physics*, 50(8):1249–1449, 2001.

[6] G. Ciovati. In *Proceedings of the 11th Workshop on RF Superconductivity*, 2005.

[7] G. Ciovati. PhD thesis, Old Dominion University, 2005.

[8] G. Ciovati. Improved oxygen diffusion model to explain the effect of low-temperature baking on high field losses in niobium superconducting cavities. *Appl. Phys. Lett.*, 89:022507, 2006.

[9] G. Eremeev. PhD thesis, Cornell University, 2008.

[10] G. Eremeev and H. Padamsee. Change in high field q-slope by anodizing of the baked cavity. *Physica C*, 441:134–136, 2006.

[11] G. Eremeev and H. Padamsee. Temperature map studies on nearly oxide-free, thin-oxide and standard-oxide cavities. In *Proceedings of the 12th Workshop on RF Superconductivity*, 2007.

[12] H. Tian et al. Recent xps studies of the effect of processing on nb srf surfaces. In *Proceedings of the 13th Workshop on RF Superconductivity*, 2007.

[13] J. Cizek et al. *Phys. Rev. B*, 32(7):4326–4331, 1985.

[14] J. Knobloch et al. High field q-slope in superconducting cavities due to magnetic field enhancement at grain boundaries. In *Proceedings of the 9th Workshop on RF Superconductivity*, 1999.

[15] J. Vines et al. Systematic trends for the medium field q-slope. In *Proceedings of the 13th Workshop on RF Superconductivity*, 2007.

[16] R. L. Geng et al. Microstructures of rf surfaces in the electron-beam-weld regions of niobium. In *Proceedings of the 9th Workshop on RF Superconductivity*, 1999.

[17] R. L. Geng et al. In *Proceedings of PAC2007*, 2007.

[18] T. Hays et al. In *Proceedings of the 7th Workshop on RF Superconductivity*, page 437, 1995.

[19] T. Proslier et al. Tunneling study of cavity grade nb: possible magnetic scattering at the surface. *Appl. Phys. Lett.*, 92:212505, 2008.

[20] R. Fertig. PhD thesis, Cornell University, 2008.

[21] R. B. Flippen. The radial velocity of magnetic field penetration in type ii superconductors. *Phys. Lett.*, 17(3), 1965.

[22] R. H. Fowler and L. Nordheim. *Proc. R. Soc. Lond. A, Math. Phys. Sci.*, 119:173, 1928.

[23] R. A. French. *Cryogenics*, 8:301, 1968.

[24] V. L. Ginzburg and L. D. Landau. *Zh. Eksp. Teor. Fiz. [Sov. Phys. - JETP]*, 20:1064, 1950.

[25] A. Gurevich. Thermal rf breakdown of superconducting cavities. In *Proceedings of the Workshop on Pushing the Limits of RF Superconductivity.*, 2005.

[26] A. Gurevich and G. Ciovati. Dynamics of vortex penetration, jumpwise instabilities, and nonlinear surface resistance of type-ii superconductors in strong rf fields. *Physical Review B*, 77:104501, 2008.

[27] J. Halbritter. Degradation of superconducting rf cavity performances by extrinsic properties. In *Proceedings of the 10th Workshop on RF Superconductivity*, 2003.

[28] J. Knobloch. PhD thesis, Cornell University, 1997.

[29] J. D. Livingston. *Phys. Rev.*, 129:1943, 1963.

[30] J. D. Livingston. Defects and magnetic hysteresis in type ii superconductors. *Rev. Mod. Phys.*, 36(1):54–58, Jan 1964.

[31] M. H. Matloob and M. W. Roberts. *J. Chem. Soc., Faraday Trans. 1*, 73:1393–1405, 1977.

[32] P. E. Mix. *Introduction to Nondestructive Testing: A Training Guide*. Wiley-IEEE, 2005.

[33] J. F. Nye. Some geometrical relations in dislocated crystals. *Acta Metall.*, 1:153–162, 1953.

[34] E. Orowan. *Z. Phys.*, 89, 1934.

[35] H. Padamsee, J. Knobloch, and T. Hays. *RF Superconductivity for Accelerators*. John Wiley and Sons, 1998.

[36] W. Pantleon. Resolving the geometrically necessary dislocation content by conventional electron backscattering diffraction. *Scripta Materialia*, 58:994–997, 2008.

[37] M. Polanyi. *Z. Phys.*, 89, 1934.

[38] M. Rabinowitz. *Appl. Phys. Lett.*, 19(73), 1971.

[39] M. Rabinowitz. Analysis of a critical loss in a superconductor. *J. Appl. Phys.*, 88(42), 1971.

[40] A. Romanenko. Review of high field q-slope, surface measurements. In *Proceedings of the 12th Workshop on RF Superconductivity.*, 2007.

[41] H. Safa. In *Proceedings or the 9th Workshop on RF Superconductivity*, 1999.

[42] D. Saint-James and P. G. De Gennes. *Phys. Lett.*, 7:306–308, 1963.

[43] A. T. Santhanam. *Journal of Materials Science*, 11:1099–1102, 1976.

[44] A. J. Schwartz, M. Kumar, and B. L. Adams, editors. *Electron Backscatter Diffraction in Materials Science*. Kluwer Academic/Plenum Publishers, 2000.

[45] G. I. Taylor. *Proc. R. Soc. London*, 145A, 1934.

[46] H. Tian. Scale-specific nb surface topographic characterizations for superconducting rf accelerators cavities. In *Proceedings of the 3rd International*

Workshop on Thin films and New Ideas for pushing the limits of RF Superconductivity, 2008.

[47] B. Visentin. In *Proceedings of the Workshop on Pushing the Limits of RF Superconductivity*, 2006.